uOttawa

L'Université canadienne
Canada's university

FACULTÉ DES ÉTUDES SUPÉRIEURES
ET POSTOCTORALES

uOttawa

L'Université canadienne
Canada's university

FACULTY OF GRADUATE AND
POSDOCTORAL STUDIES

Younes Nouri
AUTEUR DE LA THÈSE / AUTHOR OF THESIS

M.A.Sc. (Civil Engineering)
GRADE / DEGREE

Department of Civil Engineering
FACULTÉ, ÉCOLE, DÉPARTEMENT / FACULTY, SCHOOL, DEPARTMENT

The Impact of Hydraulic Bores and Debris on Free Standing Structures

TITRE DE LA THÈSE / TITLE OF THESIS

Dr. Ioan Nistor & Dr. Dan Palermo
DIRECTEUR (DIRECTRICE) DE LA THÈSE / THESIS SUPERVISOR

Dr. Andrew Cornett
CO-DIRECTEUR (CO-DIRECTRICE) DE LA THÈSE / THESIS CO-SUPERVISOR

EXAMINATEURS (EXAMINATRICES) DE LA THÈSE / THESIS EXAMINERS

Dr. E. Sherwood

Dr. C. Rennie

Dr. T. S. Murty

Gary W. Slater
Le Doyen de la Faculté des études supérieures et postdoctorales / Dean of the Faculty of Graduate and Postdoctoral Studies

The Impact of Hydraulic Bores and Debris on Free Standing Structures

Younes Nouri

Thesis submitted to the
Faculty of Graduate and Postdoctoral Studies
in partial fulfillment of the requirements for the degree of

Master of Applied Science in Civil Engineering

Under the auspices of the Ottawa-Carleton Institute for Civil Engineering

University of Ottawa
Ottawa, Ontario, Canada
May 2008

Your file Votre référence
ISBN: 978-0-494-50910-4
Our file Notre référence
ISBN: 978-0-494-50910-4

Abstract

As tsunami waves travel towards the shoreline, they may break offshore and runup the shore as a hydraulic bore. Recorded videos from the December 26, 2004 Indian Ocean Tsunami show that tsunami waves transformed into a hydraulic bore that propagated onshore with considerably high velocity. Large pieces of debris such as boats were carried up to four kilometers inland. The 2004 December Indian Ocean Tsunami severely affected communities bordering the Indian Ocean, including the coasts of Indonesia, India, Sri Lanka, Thailand, the Maldives Islands, as well as the littoral zones of several West African countries. The performance of structures built in the vicinity of shorelines in these countries highlights the fact that current structural design codes do not give proper attention to tsunami-induced forces and the impact of floating debris.

Currently, there are no clearly established procedures to address tsunami-induced forces. In this study, the deficiencies and discrepancies within tsunami-resistant design of typical buildings among the existing structural codes are identified. Currently, analogies between a tsunami-induced bore and a dam-break wave exist in literature. Therefore, in order to advance the existing understanding of bore-structure interactions, an experimental approach was taken where a dam-break flow, generated by the fast opening of a gate, impacts various free standing structures of different shapes located downstream of the gate. The pressures and forces exerted on all sides of the structure, together with the bore height and the flow velocities in the flume were measured. The effect of upstream obstacles and flow constrictions was also investigated. In addition, to further understanding of debris impact during a tsunami, wooden logs were added to the bore in order to act as water borne missiles while the structure reactions were measured.

The present study aims to provide a better qualitative and quantitative understanding of tsunami-induced forces and debris impact in an effort to improve existing structural codes for the design of buildings that are located in the vicinity of the shoreline in tsunami prone areas.

Acknowledgments

I would like to thank my supervisors Dr. Ioan Nistor, Dr. Dan Palermo and Dr. Andrew Cornett for their guidance, helpful critique and endless support during my studies. The past two years have been a great learning experience from various scientific and personal aspects for me, for which I am really grateful.

I would like to sincerely thank everyone working in the Coastal, Ports and Offshore Group at the Canadian Hydraulics Centre, National Research Council of Canada, Ottawa for providing the facilities for performing the experiments, their significant help in the preparation of the flume and in facilitating the experimental set-up. I have been able to learn a great deal about laboratory research work through out this study. I am very grateful for all I have learned, especially from Dr. Andrew Cornett, the Coastal, Ports and Offshore Group Leader.

I would like to acknowledge the help of John Perrins, the senior technical officer of the machine shop at the University of Ottawa for building the acrylic structure used in the research. Also, Bertrand Boisseuil, Antoine Cousin, and Nima Aghnyaei helped me significantly with preparing and performing the experiments, for which I am grateful. I received valuable advice during this study from Dr. Colin Rennie and I would like to thank him. I was fortunate to receive never ending help and invaluable advice from Elizabeth Jamieson, my friend and colleague, throughout this study, for which I am thankful.

Finally, I would like to thank family for all the endless support they have provided me, and to whom I owe everything.

Table of Contents

List of Figures

List of Tables

List of Symbols

Roman letters

A	Projected area of the body normal to the direction of flow (m^2)
C	Dimensionless coefficient
C_D	Drag coefficient (non-dimensional)
d_0	Initial reservoir height (m)
d_S	Inundation depth (m)
f	Darcy-Weisbach friction factor (non-dimensional)
F_B	Buoyancy force (N)
F_{brkp}	Breaking force on columns (N)
F_{brkw}	Breaking force on walls (N)
F_D	Total drag force acting in the direction of flow (N)
F_{HS}	Hydrostatic force per unit width (N/m)
F_i	Impact force (N)
F_s	Total surge force per unit width of wall (N/m)
g	Gravitational acceleration (m/s^2)
h	Surge height (m)
h_0	Impoundment depth (the initial still water level upstream of the gate when the gate is closed) (m)
m	Mass of the body impacting the structure (kg)
t	Time (s)
u	Flow velocity (m/s)
u_b	Velocity of impacting body (assumed equal to the flow velocity) (m/s)
u_I	Approach velocity of impacting body (assumed equal to the flow velocity) (m/s)
u_P	Normal component of velocity (m/s)
U	Bore front velocity (m/s)
V	Submerged volume of the structure (m^3)

V_0	Initial flow velocity behind the dam (m/s)
x	Horizontal location, measured from the gate (m)
x_1	Location of the transition point from ideal dam-break wave profile and wave tip region (m)
x_2	Location of the negative wave front (m)
x_s	Location of the wave front tip (m)

Greek letter symbols

θ	Bed slope (non-dimensional)
ρ	Seawater density (kg/m^3)
Δt	Impact duration (equals to the time between initial contact of the body with the building and the maximum impact force) (s)
γ	Specific weight of sea water (N/m^3)

Subscripts

x	Horizontal coordinate (m)

Chapter 1. Introduction

1.1. Objective

The 26 December 2004 Indian Ocean Tsunami severely affected communities bordering the Indian Ocean, including the coasts of Indonesia, India, Sri Lanka, Thailand, the Maldive Islands, as well as the littoral zones of several West African countries. Triggered by the fourth strongest earthquake recorded since 1900, with a magnitude of 9.1 on the Richter scale according to the US Geological Survey (USGS), the devastating tsunami was generated off the west coast of northern Sumatra, Indonesia. According to USGS (2007) and Munich Re Group (2005), the tsunami waves propagated over the entire area of the Indian Ocean, causing a huge number of casualties: more than 283,100 people were killed; 14,100 were listed as missing; and 1,126,900 were displaced. Further, the tsunami impacts resulted in significant economic losses, estimated to exceed US $10 billion. The USGS reported that the 2004 Indian Ocean Tsunami was one of the most destructive natural hazards causing more casualties than any other in recorded history. The 2004 Indian Ocean Tsunami was recorded nearly world wide on tide gauges in the Indian, Pacific and Atlantic Oceans. It led to generation of seiches in India and the United States, and subsidence and landslides in Sumatra. Also, as a result of this disaster, a mud volcano near Baratang, Andaman Islands became active on December 28, 2004.

The infrastructure of hundreds of cities and villages in the above mentioned countries (especially Thailand, Indonesia and Sri Lanka) was severely affected by the impact of tsunami waves. The devastating effects raised public concern and revealed deficiencies that exist with the current warning and defence systems against tsunamis and also highlighted the need for constructing tsunami shelters. One important element that needs significant improvement is the estimation of the lateral resistance of onshore structures against tsunami-induced forces and also the quantification of impact forces generated by water borne debris. Proper attention must be paid to the detailed design of structural members exposed to the above mentioned forces. Reconnaissance missions of the December 2004 Indian Ocean Tsunami disaster revealed that tsunami-induced forces can lead to severe damage or collapse of structures as shown in Fig. 1.1 (Ghobarah *et al.* 2006; Maheshwari *et al.* 2006; Murty *et al.* 2006; Nistor *et al.* 2006; Ruangrassamee *et al.* 2006; Saatcioglu *et al.* 2005, 2006a,b; Tomita *et al.* 2006; and Yamamoto *et al.* 2006). Therefore, these forces should be properly accounted for in the design of infrastructure built within a certain distance from the shoreline in tsunami prone areas.

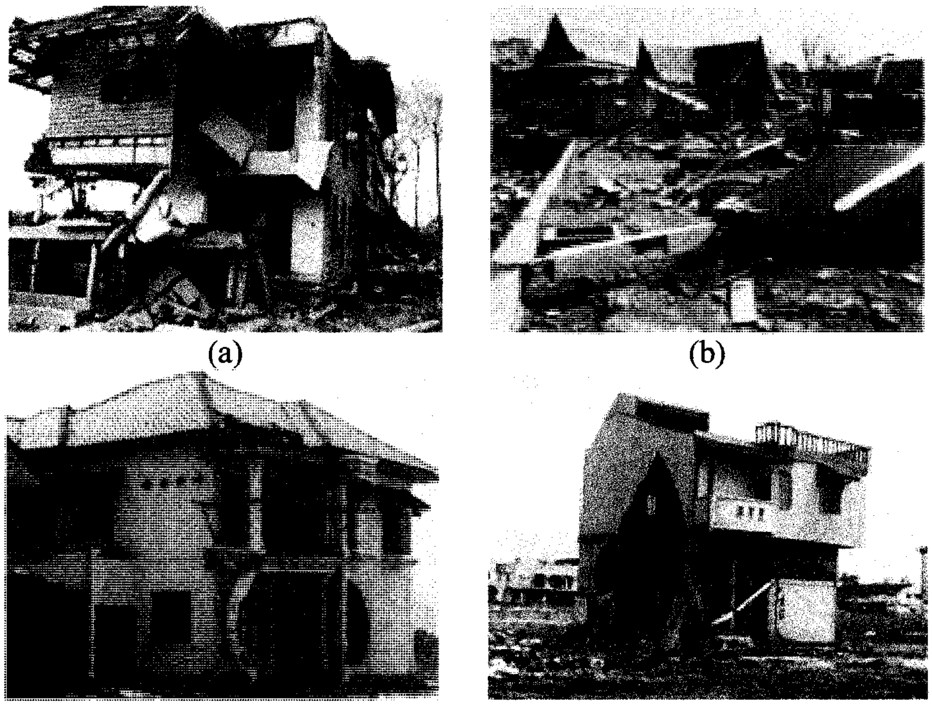

(a) (b) (c) (d)

Fig. 1.1. Tsunami damage in Thailand and Indonesia (December 2004 Indian Ocean Tsunami): (a) severe structural damage, Khao Lak, Thailand; (b) column failure of a reinforced concrete frame, Phuket, Thailand; (c) column failure due to debris impact, Banda Aceh, Indonesia; (d) punching failure of infill walls, Banda Aceh, Indonesia (Nistor *et al.* 2006).

A tsunami is a series of successive ocean waves caused by a large vertical displacement of sea water. They are usually triggered by an earthquake, but they can also be generated by volcanic eruptions, landslides, undersea slumps or meteor impacts. As a result of such events, large volumes of water may be displaced and further travel towards the shoreline in the form of a long wave. While approaching shallow coastal waters, the tsunami wave gets "squeezed" by the sloping bottom and its amplitude increases. The tsunami wave can then transform near the shore into an advancing hydraulic bore, similar to a dam-break wave (flood wave generated by sudden failure of a dam). Finally, while travelling overland, this bore impacts any infrastructure lying in its path. The bore can transport significant amounts and varying sizes of debris, such as drift wood, components of buildings, vehicles and even large boats.

The design of coastal structures such as breakwaters, jetties, groins, and quay walls, against waves, is typically governed by the effect of breaking waves and their associated forces, and is well established in the literature. However, unlike coastal structures, the evaluation and impact of tsunami-induced hydrodynamic forces on structural elements, (which are an integral part of buildings used for habitation and/or economic activity), has received little attention by researchers and designers. The poor performance of structures during the 2004 Indian Ocean Tsunami and the shortcomings of structural design codes may indicate that designers had assumed that there was no need to design structures against tsunami-induced forces. This assumption could be based on the fact that even moderately destructive tsunamis are rare events, with significantly large return periods. However, lessons learned from the Indian Ocean disaster revealed that tsunami-induced forces should be accounted for in the design of structures built within a certain distance from the shoreline in tsunami prone areas.

Reinforced concrete structures were observed to withstand tsunamis with acceptable low levels of damage (Shuto 1994); the level of damage was defined by Shuto (1994) as follows:

- **Destroyed:** walls and most pillars are damaged; restoration is not possible.
- **Partially Damaged:** most pillars withstand the tsunami, but parts of the walls are damaged; restoration is possible.
- **Withstood:** windows are broken, but pillars and walls withstand; it is possible to re-use the structure after slight repairs.

However, the results of field surveys performed in the aftermath of the 2004 Indian Ocean Tsunami in Indonesia and Thailand showed that poorly detailed concrete structures were 'destroyed' or experienced 'partial damage' (Matsutomi *et al.* 2006). In general, results from a number of other field surveys in the affected countries confirmed these observations (Saatcioglu *et al.* 2006a,b). As shown in Fig. 1.2, inundation depths of more than five meters can induce 'Partial Damage' on concrete structures. A review of existing design codes and technical literature in Chapter 3 highlights the fact that current structural design codes do not give proper attention to tsunami-induced forces and the impact of floating debris.

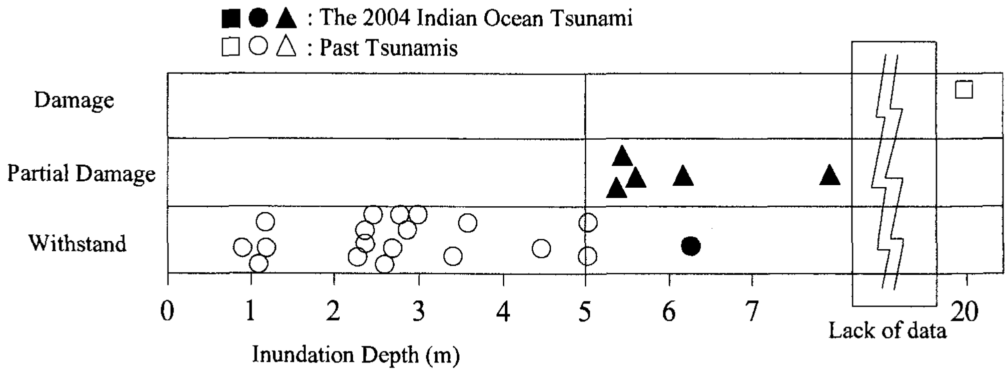

Fig. 1.2. Relation between the inundation depth and degree of damage to reinforced concrete buildings (Matsutomi *et al.* 2006).

Currently, there are no clearly established procedures that address tsunami-induced forces for the design of buildings located in the vicinity of the shoreline in tsunami prone areas. Moreover, significant disagreement on the existing empirical formulae for the calculation of tsunami-induced force components has fostered new research interests in an effort to properly address both tsunami-induced forces and the impact of floating debris within design codes. Some of the shortcomings and inconsistencies of the existing codes with regard to tsunami-induced forces are also highlighted in this thesis.

1.2. Scope

While tsunamis travel toward the shoreline, they may break offshore and runup the shore as a hydraulic bore. Recorded videos from the December 2004 Indian Ocean Tsunami showed that, in most areas, the tsunami transformed into a hydraulic bore which propagated onshore with considerably high velocity. Evidence of the enormous forces generated by the tsunami are documented by structural failures along with the displacement of large pieces of debris, such as large boats, that were carried up to four kilometers inland from the shoreline.

The present study was performed in order to investigate the mechanisms and physics of the bore-structure interaction. An experimental approach was taken, where a dam-break flow, generated by the fast opening of a gate, impacted various free standing structures of different shapes located downstream of the gate. The pressures and forces exerted on all sides of the structure, together with the bore height and flow velocities along the flume were measured and recorded. The effect of upstream obstacles and flow constrictions was also investigated. In addition, wooden logs were added to the bore to act as water borne missiles and the structure reactions were measured in order to further the understanding of debris impact during a tsunami.

The laboratory-scale dam-break flows studied in this thesis provide a reasonable approximation of the overland flow caused by tsunamis that break offshore. However, it is important to bear in mind that tsunamis are often a series of successive ways where the first wave may not be the largest.

1.3. Contributions

The novelty of the present study resides in the investigation of the interaction of a hydraulic bore with free-standing structures, with respect to quantifying exerted pressures and forces. Moreover, the effect of upstream obstacles and flow constrictions on the above forces had not been previously investigated. This thesis aims to enhance the understanding of the bore-structure interaction. The results obtained can be further used to provide guidelines for the design of structures located in the vicinity of shorelines in tsunami-prone areas.

In addition to the application of this study to improving design guidelines, the research results are valuable for the validation of numerical models. The most recently developed numerical methods, dealing with the interaction of fluid-structure at the cutting edge of multi-phase numerical modeling, must be validated with experimental data. However, reliable sets of data investigating fluid-structure interactions are very limited.

1.4. Outline

Chapter 1 provides an introduction to the present study. Main elements of the thesis, including objective, research scope, thesis contributions, and thesis outline are briefly explained.

A detailed literature review is presented in Chapter 2, which includes a description of the characteristics of a tsunami-induced hydraulic bore, as well as existing results of current research on the impact of hydraulic bores and debris on walls and free-standing structures. The main objective of the literature review is to identify gaps in existing knowledge of tsunami-induced forces and debris impact.

In Chapter 3, most of the existing formulations for estimating tsunami-induced force components are gathered and compared; the deficiencies and the discrepancies in tsunami resistant design of typical buildings among the existing structural codes are also illustrated. The main objective of this chapter is to identify gaps in the current structural codes for the design of onshore structures against tsunami-induced forces.

The experimental set-up is described in detail in Chapter 4. The characteristics of the facility, preparation of the flume, and construction of the gate, together with the method of carrying out the experiments, are briefly described in this chapter. The calibration procedure, specifications of the measurement devices, sampling rate of measuring data and the position of instruments used in the experiments are also explained.

In Chapter 5, data obtained for different tests with varying configurations for the measurement devices and structure shape and position are presented and discussed. Data analysis is performed and discussions are presented.

Chapter 6 presents a comparison of existing structural codes that address tsunami-induced forces through a design example. Furthermore, dynamic analysis is used to demonstrate the effects of tsunami-induced impulsive forces exerted on structures.

Conclusions based on obtained data and results of the data analysis are presented in Chapter 7. The contributions of the present research are outlined in this chapter, along with recommendations for future work.

Chapter 2. Literature Review

In this chapter, results of a literature review are presented in order to identify gaps and shortcomings within existing research. This chapter opens with a survey of the research performed on dam-break flows. Further on, the analogy between a tsunami-induced bore and a dam-break flow is explained. Then, published research results on the pressures and forces exerted on structures by hydraulic bores are reviewed.

2.1. Dam-Break Wave

A dam-break wave is one of the most studied examples of unsteady flow in open channels. Catastrophes caused by the sudden failure of dams and the resulting wave have attracted physicists and scientists since the 19th century (Chanson 2004). Major dam breaks in the past century, including failures of the St Francis Dam, Malpasset Dam and the overtopping of the Vajont Dam in 1928, 1959 and 1963, respectively, attracted recent attention to the subject (Chanson 2004).

Shallow water equations (also called *Saint-Venant equations*), providing a simplified representation of unsteady open channel flows, were derived by Saint-Venant in 1871, from depth integrated equations of momentum and mass conservation, based on the following assumptions:

1. one-dimensional flow,
2. hydrostatic pressure,
3. flow resistance being the same as a steady uniform flow for the same depth and velocity,
4. negligible bed slope (θ), i.e. $sin\theta \approx tan\theta \approx \theta$,
5. constant water density, and
6. boundaries of the channel are fixed.

It should also be noted that the sudden failure of a dam, corresponds to a discontinuity in boundary conditions of the equations. However, despite all simplifying assumptions, taking discontinuous solutions into account is still a challenging feature of the equations. Moreover, analytical solutions exist for a very limited number of cases, due to the nonlinear character of these equations. As a result, and with the advent of modern computers, numerical methods are widely utilized to solve the equations and capture the discontinuities of the solution. The method of characteristics is one of the earliest methods used to solve the Saint-Venant equations numerically, and is based on a graphic interpretation of the problem. This method is efficient in giving a good understanding of the physical concept behind the problem. The method of characteristics is still studied because it is essential for defining boundary conditions for a few explicit schemes.

2.1.1 Analytical Solutions

Solving an actual dam-break problem, while taking into account all the influencing parameters (spatial and temporal variation of cross-sectional area, bottom slope, friction characteristics, and speed of failure) is still impossible. Therefore, an idealized dam-break problem can be assumed, where a sudden removal of a gate releases a mass of water, as shown in Fig. 2.1 (Chanson 2005b). After the gate opens, a dam-break wave propagates downstream while a negative wave moves upstream.

First attempts on solving the dam-break problem date back to 1892, when Ritter (1892) made important contributions and presented an analytical solution for the case of a dam-break wave problem for an inviscid fluid in a dry, horizontal rectangular channel with a semi-infinite reservoir extension. He assumed a hydrostatic pressure field and ignored the effect of friction. A parabolic free surface profile for the flow that is concave upward was derived, and the velocity was found to vary linearly from the negative front to the positive front. Despite all the assumptions, detailed experiments have shown that Ritter's solution can predict the general characteristics of the flow quite well, except for the wave front and during wave initiation (Lauber and Hager 1998).

Major existing contributions to the analytical solution have been represented in the literature as follows:

- Ritter (1892) derived an analytical solution for dry horizontal frictionless channels; the main feature of Ritter's solution is being self-similar (i.e., the solution only depends on the ratio x/t, see Leal *et al.* (2006));

- Dressler (1952) took into account the influence of friction, based on a perturbation solution; his solution is non-self similar due to the effect of friction;
- Whitham (1955) utilized a friction model, quadratic in the flow velocity, and derived a parabolic water surface profile for the bore front that is concave downward and asymptotically approaches a vertical face in the bore front;
- Stoker (1957) generalized Ritter's approach for wet initial downstream and like Ritter, reached a self-similar solution;
- Lauber and Hager (1998) could reach a solution based on shallow water equations with friction slope in the source term; and
- Fracarollo and Capart (2002) worked on mobile bed and derived a semi-analytical solution but were incapable of providing an explicit equation for wave celerity.

Chanson (2005b and 2006) solved the Saint-Venant equations using the method of characteristics for a wide rectangular channel with a semi-infinite reservoir. He divided the flow into two separate parts: the wave tip region and a following ideal-fluid region (Fig. 2.1). In the wave tip region ($x_1 < x < x_s$), friction is the dominant term and the flow velocity does not vary rapidly, whereas in the next region ($x_2 < x < x_1$), the acceleration and inertial terms are dominant. A simple, explicit analytical solution for dam-break flow on a dry horizontal bed, in terms of bore front velocity, location and characteristics was derived. Consequently, an explicit expression is provided for free surface profiles of the flow. Comparison with various sets of experimental data showed that the Chanson's derived solution is in agreement with experimental studies and provides a good estimation of more accurate models (Chanson 2005b). The advantage of this solution is that it can be easily implemented to calibrate the instantaneous free-surface profiles for real fluids, selecting appropriate values of flow resistance friction. It should be noted that this solution is derived based on a number of assumptions, such as applicability of Saint-Venant equations and a constant Darcy-Weisbach friction factor in the wave-tip region. Consequently, application of the solution should be limited.

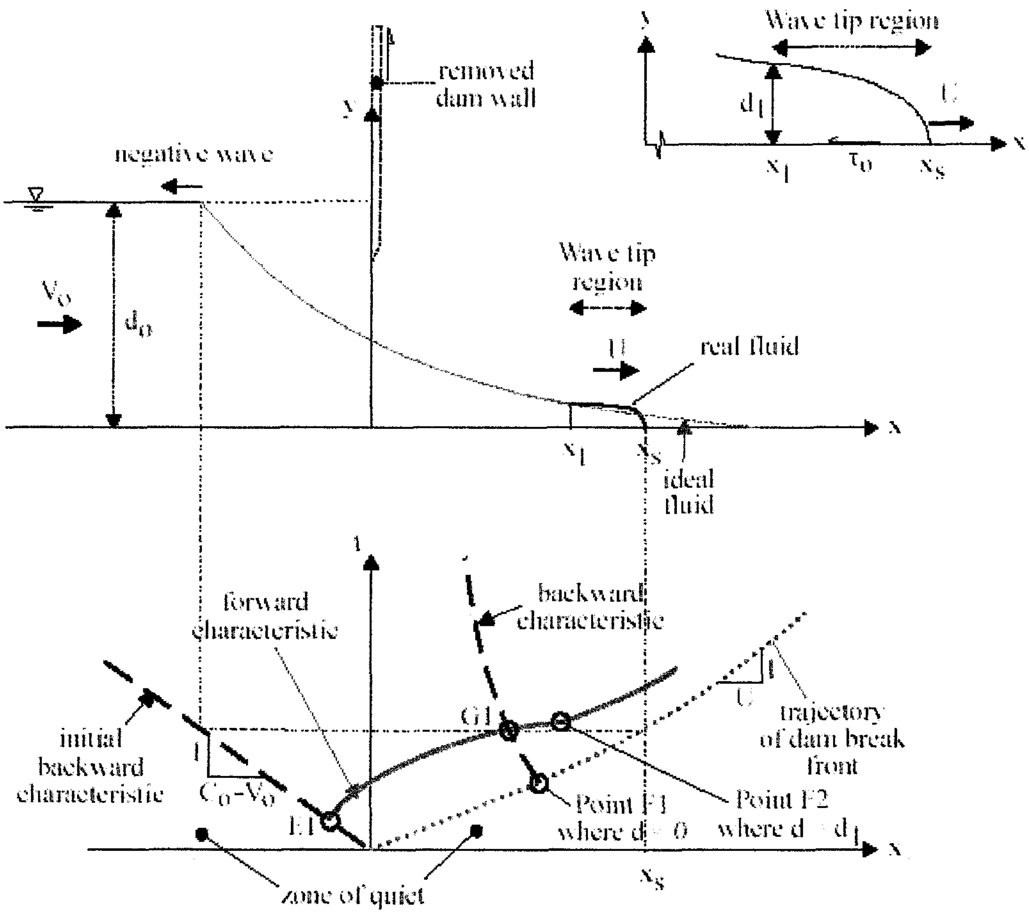

Fig. 2.1. Sketch of an idealized dam-break in a dry horizontal channel, Chanson (2005b).

The wave front velocity (U) can be calculated from the following equation (Eq. 2.1), whereas the location of wave front (x_s) can be obtained from Eq. 2.2.

$$\frac{8}{3}\times\frac{1}{f}\times\frac{\left(1-\dfrac{U}{2\sqrt{gd_0}}\right)^3}{\dfrac{U^2}{gd_0}}=\sqrt{\frac{g}{d_0}}\times t \tag{2.1}$$

$$\frac{x_s}{d_0}=\left(\frac{3U}{2\sqrt{gd_0}}-1\right)\times\sqrt{\frac{g}{d_0}}\times t+\frac{4}{f\times\left(\dfrac{U}{\sqrt{gd_0}}\right)^2}\times\left(1-\frac{U}{2\sqrt{g\times d_0}}\right)^4 \tag{2.2}$$

where f is the Darcy-Weisbach friction factor, g is the gravitational acceleration, t is the time and d_0 is the initial reservoir height.

The instantaneous free-surface profile for the ideal-fluid region and wave tip region is then obtained from the following equations (Eqs. 2.3 and 2.4) respectively:

$$\frac{d}{d_0} = \frac{1}{9} \times \left(2 - \frac{x}{t \times \sqrt{g \times d_0}} \right)^2 \text{ where } -\sqrt{\frac{g}{d_0}} \times t \le \frac{x}{d_0} \le \left(\frac{3}{2} \times \frac{U}{\sqrt{g \times d_0}} - 1 \right) \times \sqrt{\frac{g}{d_0}} \times t \quad (2.3)$$

$$\frac{d}{d_0} = \sqrt{\frac{f}{4} \times \frac{U^2}{g \times d_0} \times \frac{x_s - x}{d_0}} \text{ where } \left(\frac{3}{2} \times \frac{U}{\sqrt{g \times d_0}} - 1 \right) \times \sqrt{\frac{g}{d_0}} \times t \le \frac{x}{d_0} \le \frac{x_s}{d_0} \quad (2.4)$$

Chanson (2005b) further developed his work to address the case of a dam-break problem where the initial flow velocity behind the dam (V_0) is non-zero (i.e. both the dam and the reservoir translate at a constant speed V_0 prior to dam removal). Similarly, instantaneous free-surface profiles for the wave tip region and the ideal-fluid region were provided. Applications of these simple analytical solutions were demonstrated through comparison of dam-break wave with tsunami surges, which is mentioned in Sec. 2.2.1. Further details can be found in Chanson (2005a, b and 2006).

2.1.2 Experimental Work

Lauber and Hager (1998) performed a comprehensive literature review of existing experimental studies on dam-break waves in horizontal and sloped channels. They summarized the existing understanding of the phenomena in horizontal channels as follows:

- "the basic flow configurations of dam-break waves are currently known;
- sudden dam-breaks occur, provided the non-dimensional removal period is smaller than $(g/h_0)^{1/2}t=2^{1/2}$, with g = gravitational acceleration, h_0 = reservoir depth and t = time;
- the effect of tailwater on the propagation characteristics is significant;
- the effects of scale in a smooth prismatic and rectangular channel are insignificant provided $h_0 \ge 300$ mm, except for the wave front, the flow is then governed by the Froude similarity law; and
- the effect of boundary roughness is small during the initial wave propagation. It has a significant effect close to the wave front for larger times, however;

- Ritter's classic dam-break solution gives a reasonable picture of dam-break flow, except close to both the positive and negative wave fronts; and
- hydraulic jumps complicate dam-break flows, and such phenomena cannot be described easily with either experimental or numerical approaches."

Consequently, most studies have been geared towards investigating the initiation process of a dam-break flow and the flow features at the positive bore front. Most of the tests are performed in horizontal flumes or flumes with small angle. Also, the test flumes are supposed to be as long as possible to approach the assumption of an infinitely long channel in analytical solutions. Moreover, tests with dry or wet downstream and mobile or immobile beds have been performed to investigate the effect of various parameters on flow variables. A number of studies exist on dam-break experiments with fixed bed, such as those of Levin (1952), Dressler (1954), U.S. Army Corps of Engineers (1960, 1961), Estrade (1967), Chervet *et al.* (1970), Drobir (1971), Barr and Das (1980), Martin (1981), Miller and Chaudhry (1989), Bell *et al.* (1992), Franco (1996), Lauber and Hager (1998), Stansby *et al.* (1998), Leal (1999), Briechle and Kötenger (2002), and Leal *et al.* (2002).

Leal *et al.* (2006) conducted a comprehensive literature review of dam-break wave experiments in order to investigate the existing formulae and data sets on dam-break wave-front velocity. Fig. 2.2 shows a dimensionless representation of the data from several data sets: Bell *et al.* 1992 (Be1); Briechle and Kotenger 2002 (Br1,Br2); Franco, 1996 (Fr); Lauber and Hager 1998 (La); Leal 1999 (Le1), Leal *et al.* 2002 (Lefb1); and Stansby *et al.* 1998 (St1,St2). The results are presented in terms of location ($X = x/h_0$) and time ($T = t\sqrt{g/h_0}$) where x = downstream distance to the dam section, t = time after the gate opening, and h_0 = impoundment depth (the initial still water level upstream of the gate when the gate is closed). Furthermore, Leal *et al.* (2006) developed a numerical model based on shallow-water approach, assuming that sediment transport was occurring dominantly in the form of contact-load and using recent developments in sheet flow studies (see Leal *et al.*, 2006 for further details). It was observed that the result from the numerical model provided the best description of the experimental data (Fig. 2.2).

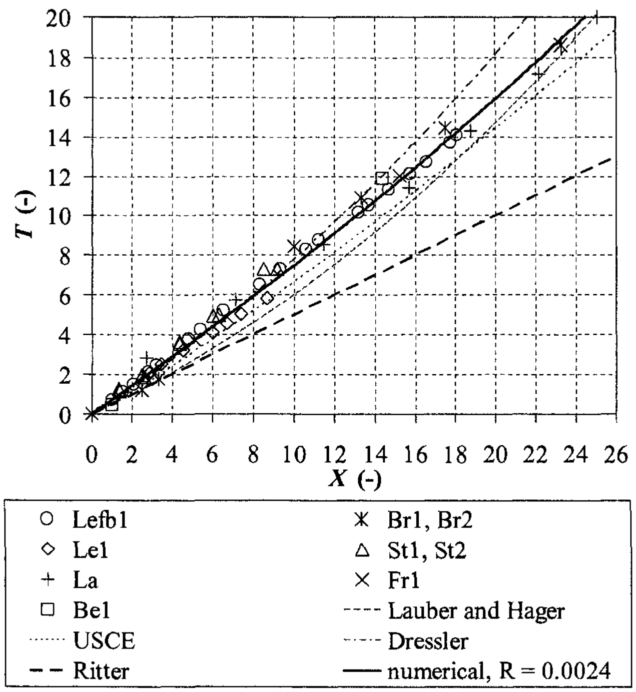

Fig. 2.2. Wave-front locations in (X,T) space over dry fixed bed; comparison of experimental data sets (symbols) with proposed formulae (lines) (Leal *et al.*, 2006).

2.2. Tsunami-Induced Hydraulic Bores

As tsunami waves advance towards the shoreline and water depth decreases, their wave height increases while celerity decreases. Tsunami waves may break offshore or at the shoreline, inundating low-lying coastal areas in the form of a hydraulic bore. On the other hand, tsunami inundation can also occur as a gradual rise and recession of the sea level for the case of non-breaking tsunami waves. The width of the continental shelf, the initial tsunami wave shape, the beach slope and the tsunami wave length are all parameters which govern the breaking pattern of tsunami waves (Yeh 2006). A collapsing breaker, occurring on a sloping beach, is shown in Fig. 2.3.

Tsunami waves have a larger horizontal length scale compared to the vertical. Consequently, implementing shallow water wave theory (i.e., depth-integrated equations of momentum and mass conservation with the assumption of a hydrostatic pressure field) seems to be a reasonable method for representing tsunami wave propagation. Using these equations, it has been shown that the behaviour and runup of non-breaking tsunami waves can be predicted with acceptable accuracy. However, disagreement has been observed between experiment and prediction, in terms of behaviour and runup of breaking waves and the resulting bore (Hibberd and Perregrine 1979, Packwood and Peregrine 1981).

Significant efforts were directed towards the experimental investigation of the mechanisms of tsunami bore runup (Yeh *et al.* 1989, Yeh 1991). Although a two-dimensional dam-break flow was used in the experiments, the bore motion was observed to be fully three-dimensional and highly turbulent. This is in agreement with other observations regarding the irregularity of the bore front in transverse direction and the noticeable fluctuation of the front propagation (Yeh and Mok 1990).

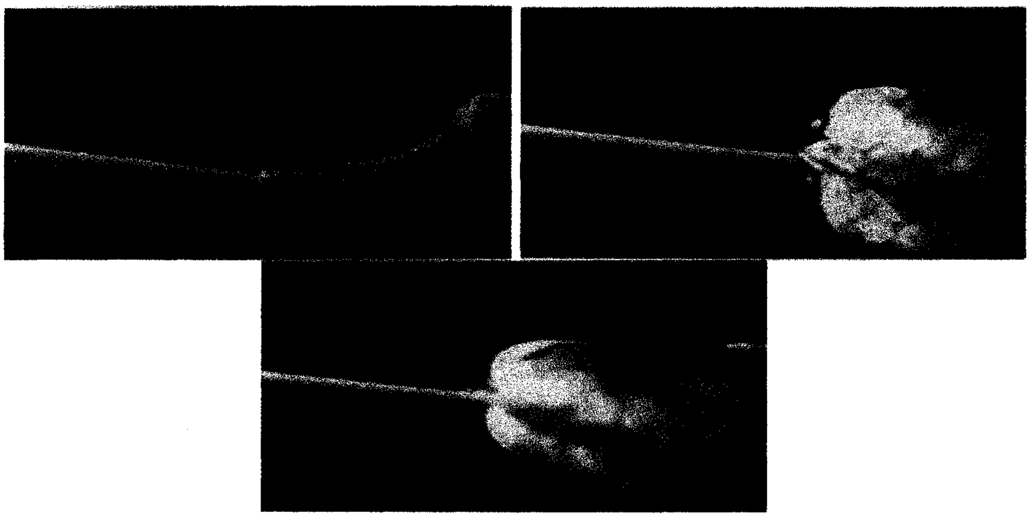

Fig. 2.3. A collapsing breaker resulted from an undular bore (Yeh and Mok 1991).

Pictures and video recordings taken during the 2004 Indian Ocean Tsunami showed tsunami waves breaking offshore, followed by a highly turbulent tsunami-induced bore propagating onshore with considerably high velocity. Fig. 2.4 shows four photos that were taken during the devastating tsunami. These photos were taken by a Canadian couple at a tourist resort in Khao Lak, Thailand on December 26, 2004. Unfortunately, the couple lost their lives after the bore inundated the resort, but the photos were recovered afterwards from the memory card of their digital camera. The first two photos capture the recession of the sea water before the arrival of tsunami waves, revealing the tidal flats (Fig. 2.4 (a) and (b)). The next photo, Fig. 2.4(c), shows the waves traveling towards the shoreline and breaking before the shoreline. Finally, the highly turbulent tsunami-induced bore can be seen propagating onshore in Fig. 2.4 (d).

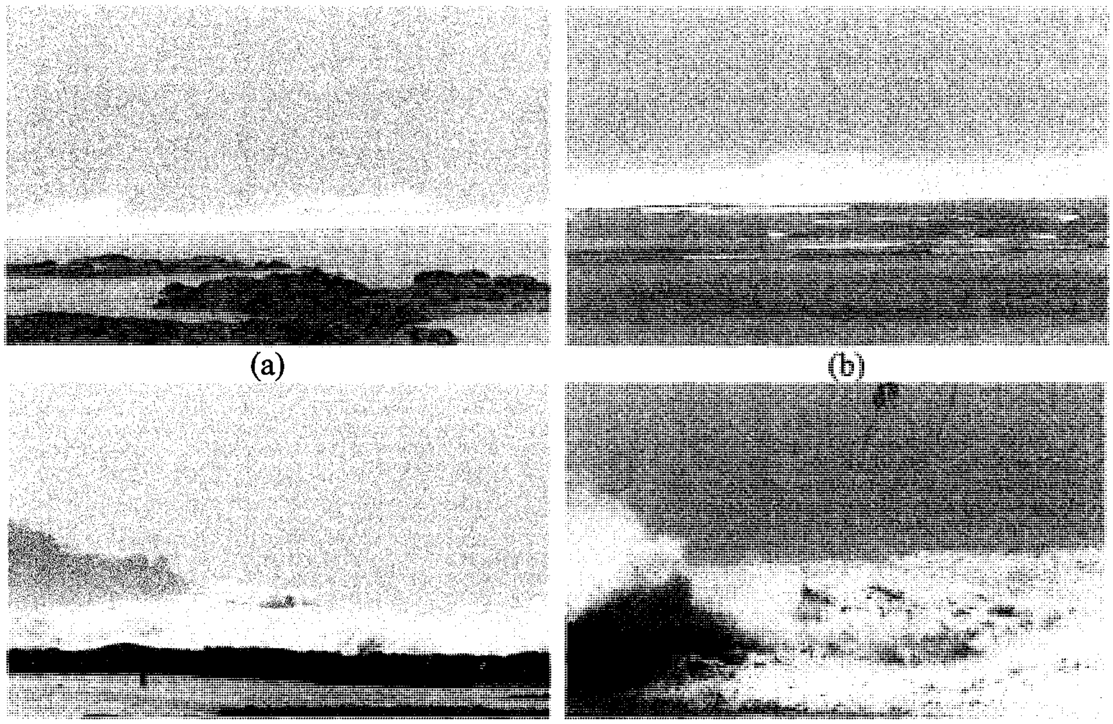

Fig. 2.4. A tsunami wave in Khao Lak, Thailand (26 December 2004 Tsunami): (a) water recedes, (b) waves approaching the shoreline, (c) tsunami waves breaking close to the shoreline (d) tsunami waves inundating the shoreline, CNN (2007).

The runup of broken tsunami waves in the form of a hydraulic bore has been witnessed and reported during previous tsunamis: Hilo, Hawaii, in the 1960 Chilian Tsunami (Cox *et al.* 1963) and along the western coast of Akita Prefecture in the 1983 Nihonkai-Chubu earthquake tsunami (Yeh 1991). Several more examples were gathered during the 2004 Indian Ocean Tsunami. For example, a tsunami-induced hydraulic bore propagating onshore is clearly captured in Fig. 2.5. It should be noted that the time lag between the pictures is 6 s. Hence, with a rough estimation of the distance traveled by the bore (12 m), the bore front velocity can be crudely calculated: $U = \frac{12}{6} = 2$ m/s. The tsunami-induced bore shown in Fig. 2.5 is a highly irregular and turbulent flow, similar in many respects to the flow generated by a dam-break on a dry horizontal bed.

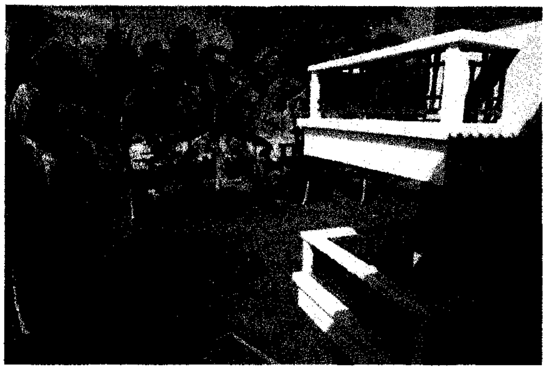
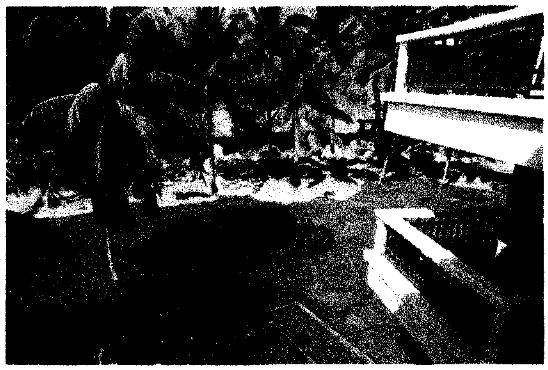

(a) t = 11:22:42 s (b) t = 12:22:48 s


(c) t = 12:22:53 s (d) t = 12:23:02 s

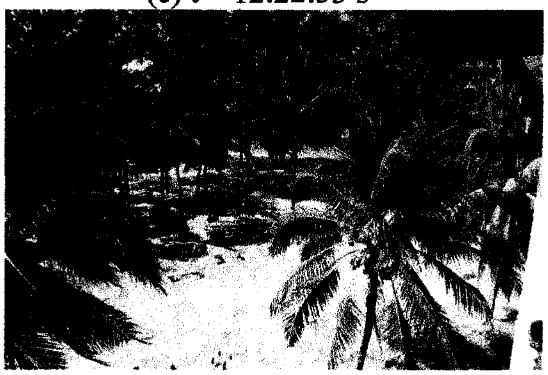


(e) t = 12:23:13 s (f) t = 12:24:41 s


(g) t = 12:24:46 s (h) t = 12:24:53 s

Fig. 2.5. Advancing tsunami-induced bore at Phuket Island, Thailand (December 2004 Tsunami), Pbase (2007).

It may be assumed that, compared to non-breaking tsunami waves, tsunami-induced bores will have less destructive force. This assumption could be based upon the fact that the wave energy will be considerably reduced due to dissipation at breaking. However, existing evidence from past tsunamis has proven otherwise: the 1960 Chilean Tsunami caused severe destruction and killed 61 people, according to Cox *et al.* (1963). One hundred fatalities were reported after the 1983 Nihonkai-Chubu Tsunami, where waves carried 4-ton armour units up to 135 m onshore, Yeh (1991). The most devastating effects were caused by the tsunami-induced bores occurring during the Indian Ocean Tsunami 2004, as mentioned before. Tsunami-induced bores in Northern Sumatra and parts of Thailand, such as Khao Lak caused tremendous damage. Fig. 2.6 illustrates an example of the extensive damage caused by tsunami-induced flows inundating low-lying coastal plains during the Indian Ocean Tsunami.

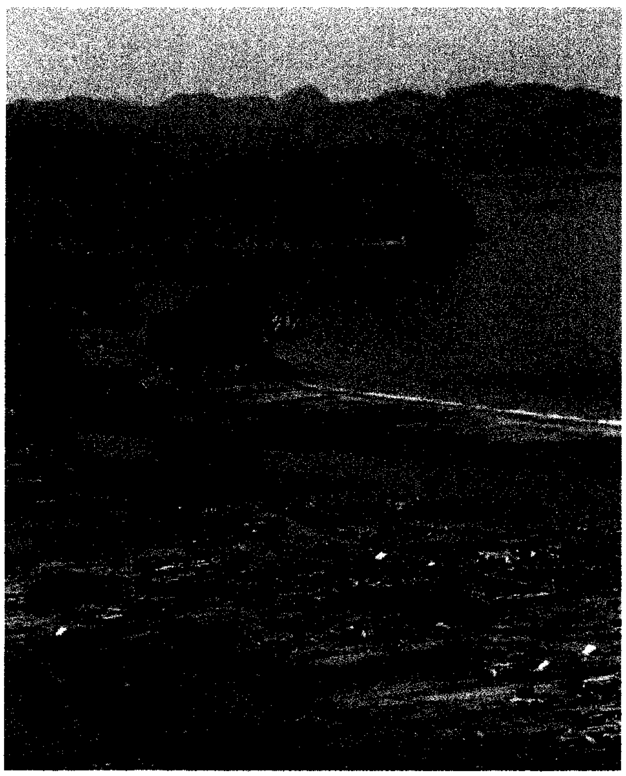

Fig. 2.6. Coastal damage caused by tsunami-induced bore at Banda Aceh Indonesia (Chanson 2005a).

2.2.1 Tsunami-Induced Bores; Analogy with Dam-Break Flow

Chanson (2005b, 2006) hypothesized that the bores generated from the breaking of tsunami waves are analogous to dam-break waves. In order to investigate this hypothesis, he compared the characteristics of a tsunami-induced bore carrying floating bodies with dam-break flows, considering various initial and boundary conditions. Dam-break wave calculations were based on his simple analytical solution and the derived explicit expressions for free-surface profile of the dam-break wave (Eq. 2.3 and 2.4) described in Sec. 2.1.1. The flow profile data for the tsunami-induced bore were obtained from a frame-by-frame analysis of a video recording taken during the 2004 Indian Ocean Tsunami at Banda Aceh, Indonesia. Several frames from this video are shown in Fig. 2.7. Water depth (d) and flow velocity (V) were estimated at three points in each frame, by means of the objects in the frames such as floor heights, and the distance traveled between each frame, respectively. Water depth values against time are shown in Fig. 2.8 (a), where t equal to zero corresponds to the time that the flow reached the first point. While the exact distance to the shoreline from where the video was taken remains unknown, it is believed to be approximately four kilometers onshore. Based on the frame-by-frame analysis of the video, bore velocity was estimated to be in the range of 1.5 to 1.6 m/s.

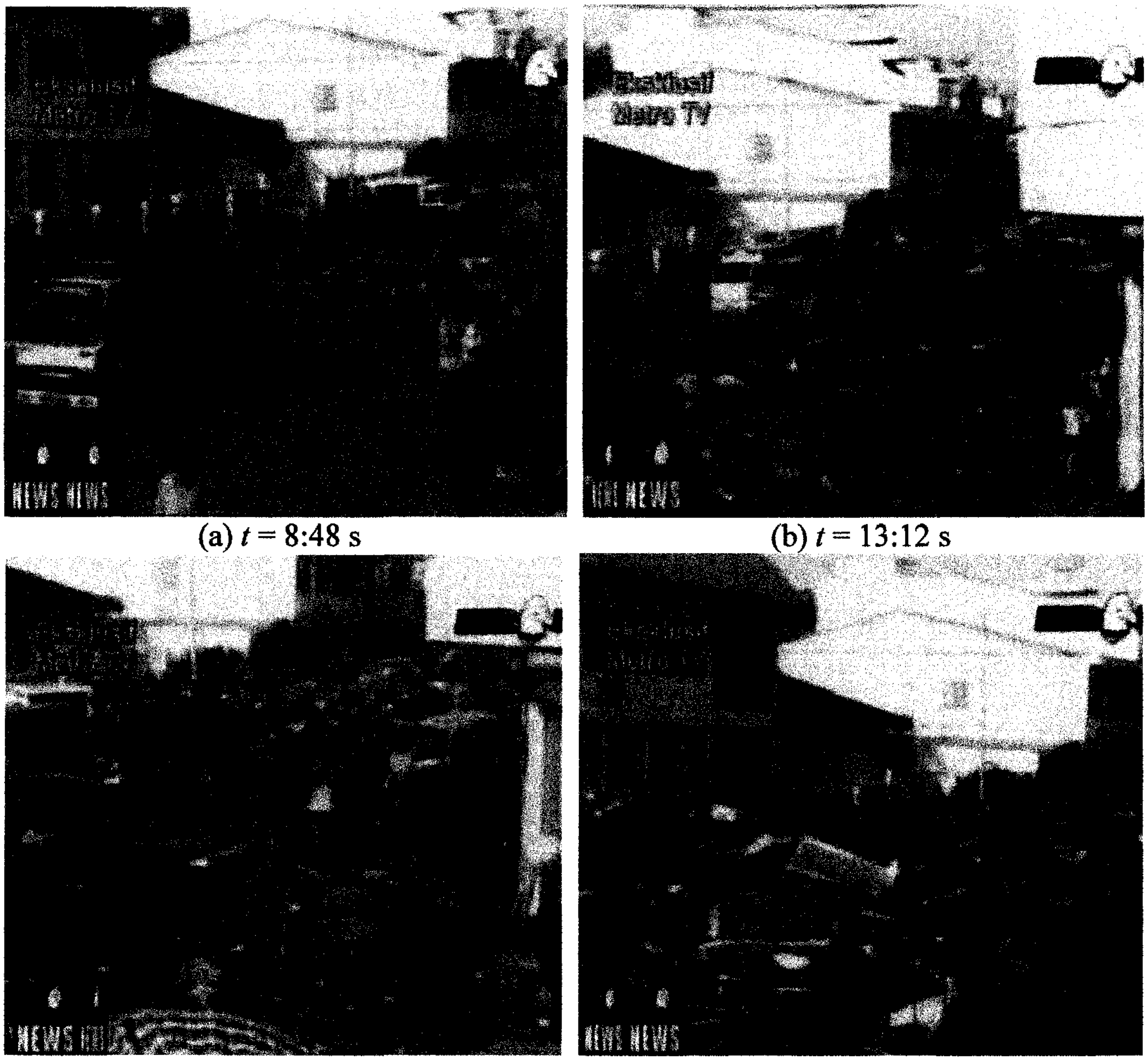

(a) $t = 8{:}48$ s (b) $t = 13{:}12$ s

(c) $t = 16{:}00$ s (d) $t = 39{:}00$ s

Fig. 2.7. Advancing mud and debris surge in Banda Aceh (26 December 2004 tsunami) (Chanson 2005b,2006).

A few assumptions were made before comparing the data obtained from the video analysis with the theoretical development. Also, various cases in terms of initial and boundary conditions were considered. Firstly, it was assumed that the bore shown in Fig. 2.7, was generated by a 1 m high solitary wave that traveled 2,000 m from deep water (1,000 m) to reach the breaking point at the shoreline. Based on solitary wave theory, the corresponding breaking wave height was calculated to be equal to 10.5 m with a velocity of 12 m/s. Then, it was assumed that further onshore from the point of wave breaking, the generated bore would be similar to a dam-break wave on a horizontal bed. Therefore, dam-break wave calculations were conducted for d_0 = 10.5 m and a horizontal bed. Four cases were considered: ideal and real flows (i.e. flow resistance was assumed $f = 0$ and 0.5), with and without initial motion (i.e. $V_0 = 0$ and 12 m/s). Results in dimensionless form are presented in Fig. 2.8 for the case of $V_0 = 0$ and $f = 0.5$. Both calculations (dotted line) and observed data are presented. It is shown that data obtained from the video analysis are in good agreement with the analytical solution, in terms of free surface flow profile. Moreover, a bore velocity of 1.2 m/s was calculated, which is close to the value obtained from the video analysis. The agreement supports Chanson's hypothesis that bores generated from the breaking of tsunami waves are analogous to dam-break flows. Yet, existing data is not sufficient to support a general conclusion.

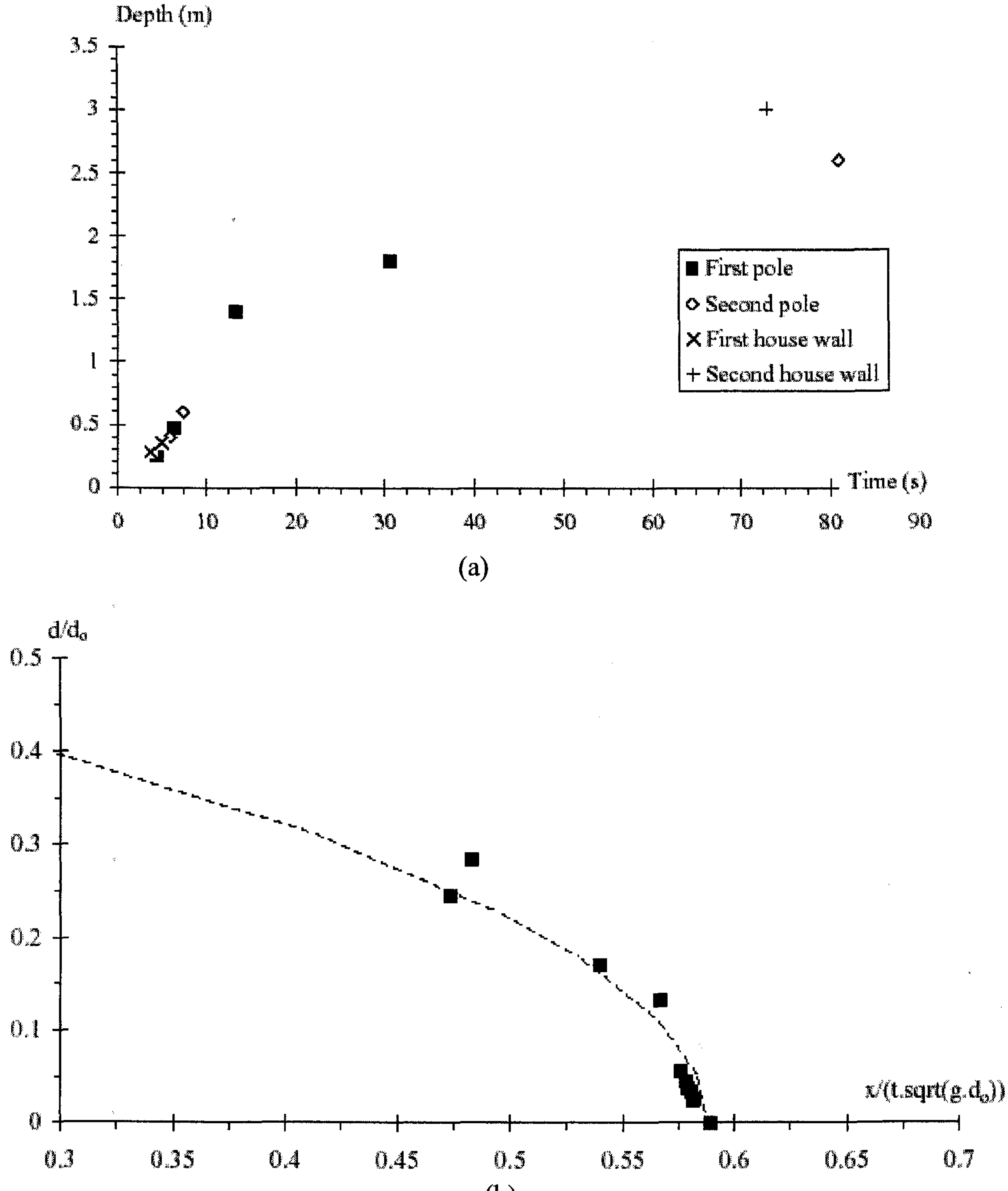

Fig. 2.8. Time-variation of water depth for the tsunami surge shown in Fig. 2.7: (a) field observations and (b) dimensionless comparison with dam-break wave, Chanson (2006).

2.3. Tsunami-Induced Forces

Snodgrass *et al.* (1951) noticed that broken waves induced larger hydrodynamic horizontal forces on a test pile compared to waves breaking at the pile location. As previously mentioned, broken tsunami waves inundate the shoreline in the form of a hydraulic bore, which is a fast moving body of water with an abrupt front. However, mechanisms of impingement of broken tsunami waves on structures located inland are not yet well understood. Pioneering analytical and experimental attempts to quantify bore characteristics and forces due to bores date back to Stoker (1957), Cumberbatch (1960), Fukui (1963), Cross (1967), and Dames and Moore (1980).

Stoker (1957) studied bore characteristics by solving nonlinear shallow water wave equations for a moving hydraulic jump advancing into still water, and derived an equation for the bore celerity ($\frac{c^2}{gh} = \left[\left(2\frac{H}{h}+3\right)^2 - 1\right]$ where c is the bore celerity, g is the gravitational acceleration, h is the still water depth and H is the bore height at the wall). Also, the reflection of a bore from a rigid vertical wall was investigated, and an analytical equation for the exerted force on the wall was presented.

Cumberbatch (1960) presented a solution for the impact of a two-dimensional fluid wedge on a vertical wall ($F = C_F \rho b H c^2$ where C_F is the force coefficient, which was shown to be only a function of the incident wedge angle, ρ is the density of the fluid, b is the width of the wall, H is the water level at wall location and c is the celerity). Gravity was ignored in the problem formulation, and the solution was intended to model the dynamics of the impact before gravitational acceleration affected the flow along the wall. A force coefficient, relating the force on the wall to the momentum flux which would occur at the wall location if the wall were not present, was included in the solution.

Cross (1967) studied the properties of surges advancing into still water and their impact forces on vertical walls, using the same approach as Cumberbatch (1960). The equation for the exerted force due to surges was further developed by including the gravity terms, which can be simplified for the maximum force due to a bore as follows (see Ramsden 1996):

$$F = \frac{1}{2}\gamma b (H+h)^2 + \rho b H c^2 \qquad (2.5)$$

where γ is the weight of water per volume, ρ is the water density, b is the width of the wall, H is the bore height at the wall, h is the still water depth and c is the celerity that can be calculated using the equation derived by Stoker.

Fukui *et al.* (1963) measured the pressures generated on walls due to the reflection of bores with varying bore heights that advanced into still water and impacted the wall on a sloped bed. The measured pressure values showed a distinctive difference between the *impulsive pressure* (obtained soon after the bore impacts the wall) and the *continuous pressure* (which corresponds to the hydrostatic pressure at the wall once the bore is reflected by the wall). Using linear regression, it was found that the *impulsive pressure* was proportional to the fourth power of the bore celerity.

Comprehensive experimental investigation of the interaction of solitary waves, bores and dry-bed surges with a vertical wall was performed by Ramsden and Raichlen (1990) and Ramsden (1993, 1996). Fig. 2.9 shows the experimental set-up of the study, where fast vertical removal of a pneumatic gate by means of an actuator released a mass of water to generate bores (initial still water downstream of the gate) and dry-bed surges (no initial water depth downstream of the gate). The experiments were carried out using a 0.396 m wide, 0.61 m deep and 36.6 m long horizontal wave tank. In addition, steep solitary waves were generated in a tilting tank by a hydraulically actuated piston. Flow profiles (wave and bore heights and runup against a wall) were measured by a laser-induced fluorescence device. In these experiments, forces and pressures exerted on a solid vertical wall were measured. Also, overturning moments were calculated using the recorded forces. The forces were inferred from the measurements of displacement sensors. However, since the sensors could not capture impulsive displacements, the results of these studies are not applicable to the estimation of impulsive forces. Further details can be found in (Ramsden 1993, 1996).

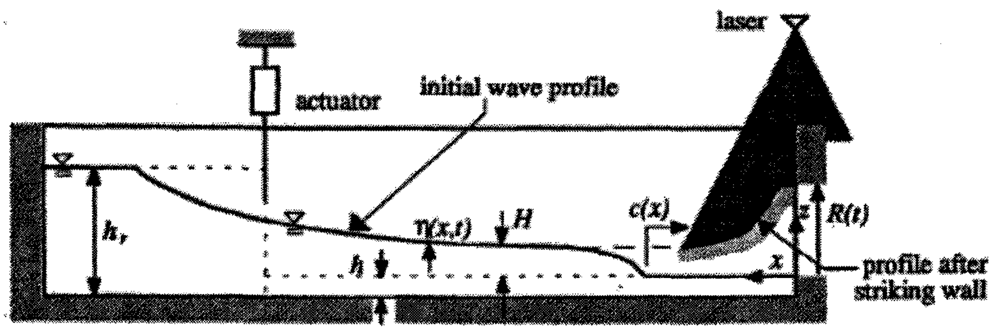

Fig. 2.9. Experimental set-up for bore and dry bed surges in horizontal tank (Ramsden, 1993).

It was observed that the pressure distribution during impact is essentially non-hydrostatic. Therefore, the pressures and forces right after the bore impact would not be obtained using shallow water equations. The experiment also demonstrated that the transition from undular to turbulent bores led to a discontinuous increase in water surface slope, followed by an increase in measured runup, pressure head, and exerted forces and moments. Fig. 2.10 shows the difference between a strong turbulent bore (on a wet bed) and a dry-bed surge with approximately the same celerity.

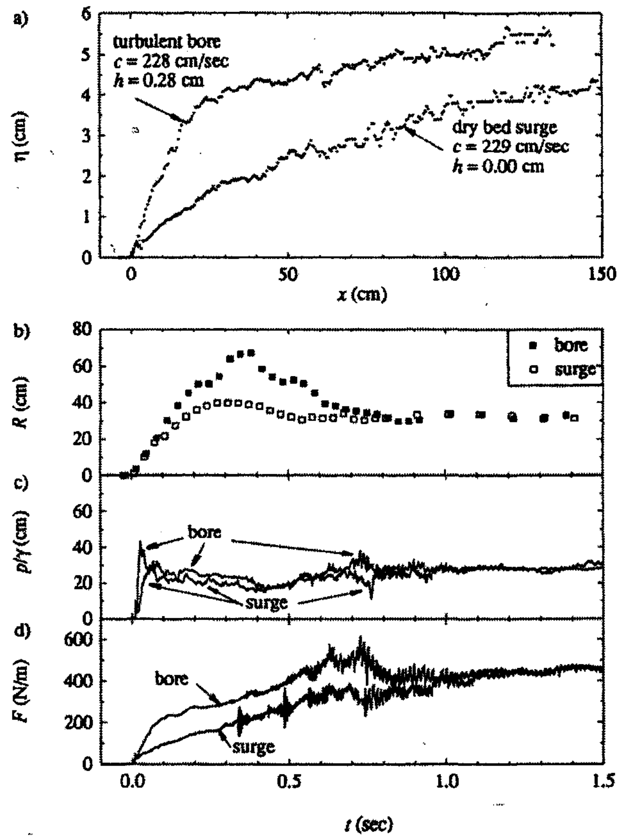

Fig. 2.10. Comparison of the experimental a) wave profile; b) runup; c) pressure head; and d) force due to a strong turbulent bore and a dry bed surge (Ramsden, 1993).

Ramsden (1993) observed that the maximum measured force due to the bores, surges and solitary waves is less than the computed forces from the maximum measured runup, assuming a hydrostatic condition. He concluded that this is due to the occurrence of vertical flow accelerations. He also found that the model of Cross (1967) underpredicts the measured forces due to the bores on dry bed by 20-50%. It was shown that the recorded forces gradually increased to an approximately constant value for both the case of a surge and a bore. No impulsive (shock) force exceeding the approximately constant force was observed. However, an initial impulsive pressure equal to three times the pressure head, corresponding to the measured runup, was recorded. Ramsden (1993) further derived empirical formulae for the maximum force and moment exerted on a vertical wall due to the bore impact (Eqs. 2.6 and 2.7).

$$\frac{F}{F_l} = 1.325 + 0.347\left(\frac{H}{h}\right) + \frac{1}{58.5}\left(\frac{H}{h}\right)^2 + \frac{1}{7160}\left(\frac{H}{h}\right)^3 \tag{2.6}$$

$$\frac{M}{M_l} = 1.923 + 0.454\left(\frac{H}{h}\right) + \frac{1}{8.21}\left(\frac{H}{h}\right)^2 + \frac{1}{808}\left(\frac{H}{h}\right)^3 \tag{2.7}$$

where F is the force on the wall, F_l is the force on the wall due to a runup equal to twice the wave height, assuming hydrostatic pressure; H is the wave height at the wall; h is still water depth, M is the moment on the wall and M_l is the moment corresponding to F_l.

Okada *et al.* (2005) conducted a survey of previous studies on tsunami wave forces and pressures, and identified five empirical formulae for tsunami-induced forces or pressures. It was found that calculation of tsunami load on structures using these formulae would result in approximately the same magnitude of load. These formulae are presented as follows:

- **Equation for tsunami wave pressure without soliton break up, Asakura *et al.* (2000):**

  $$p_m(z) = (3\eta_{\max} - z)\rho g \tag{2.8}$$

  where p_m is the maximum tsunami wave pressure ($0 \le z/\eta_{max} \le 3$), z is height of the relevant portion from ground level, g is the gravitational acceleration, η_{max} is the maximum inundation depth and ρ is the mass per unit volume of water.

- **Equation for tsunami wave pressure with soliton break up, Asakura *et al.* (2000):**

  $$p_m(z) = max(5.4\eta_{max} - 4z, 3\eta_{max} - z)\rho g \tag{2.9}$$

  where p_m is the maximum tsunami wave pressure ($0 \le z/\eta_{max} \le 3$).

  It should be noted that Eqs. 2.8 and 2.9 are proposed based on tests of tsunami waves flowing over perpendicular revetments.

- **Equation for tsunami wave pressure without soliton break up, Ikeno *et al.* (2001):**

$$p_m(z) = 2.2(a_h - z/3)a\rho g \tag{2.10}$$

where p_m is the maximum tsunami wave pressure ($0 \le z/a_H \le 3$: above the surface of the still water), a_h is the tsunami wave amplitude and a is the impact coefficient (= 1.36).

- **Equation for tsunami-induced wave forces on houses, Iizuka and Matsutomi (2000):** This empirical equation is proposed based on the degree of damage and destruction to the houses, observed during tsunamis.

$$F_{HD} = \frac{1}{2}\rho C_D u^2 h_f B_h \tag{2.11}$$

where F_{HD} is the horizontal force, C_D is the drag coefficient (= 1.1 ~ 2.0), u is the inland velocity, h_f is the inundation depth in front of the house and B_h is the width of the structure.

- **Equation for tsunami force exerted on houses, proposed by Ohmori (2000):**

$$F_H = \frac{1}{2}\rho C_D u|u|B\eta + \rho C_M \dot{u} BL\eta + \frac{1}{2}\rho C_S(\theta)u|u|B\eta + \rho g BL\eta\frac{\partial u}{\partial x} \tag{2.12}$$

where F_H is the tsunami force, B is width of the structure, C_D is the drag coefficient (= 2.05), C_M is the mass coefficient (= 2.19), $C_s(\theta)$ is the impact coefficient (= 3.6tanθ), θ is the angle of wave, u is the velocity of tsunami wave in the direction of advance, $\dot{u}$ is the acceleration of tsunami wave in the direction of advance and η is the inundation depth.

Currently, there is a lack of empirical data on the variation and vertical distribution of the force and pressure exerted on a structure by the impact of a hydraulic bore. Gomez-Gesteira and Dalrymple (2004) mentioned results from a small-scale experiment referred to as a "bore in a box", performed by Petroff and Yeh at the University of Washington where a dam-break wave impacted a tall rectangular structure. Dam-break waves were generated for both cases: dry bottom (no initial water depth downstream of the gate) and wet bottom downstream with an impoundment depth of h_0 = 0.3 m. Fig. 2.11 shows an example of the measured vertical distribution of the exerted force on the upstream face of the structure, where force was measured with a load cell. The distribution is given only for one instant and the location of this instant on the total force time-history has not been specified (presumably at the maximum force). This figure shows that in the case of a dry downstream more than 95% of the force was exerted on the lower part of the upstream face (up to 0.1 m above the bottom), whereas most of the force was exerted between 0.1 and 0.2 m above the bottom for the case of a wet bed.

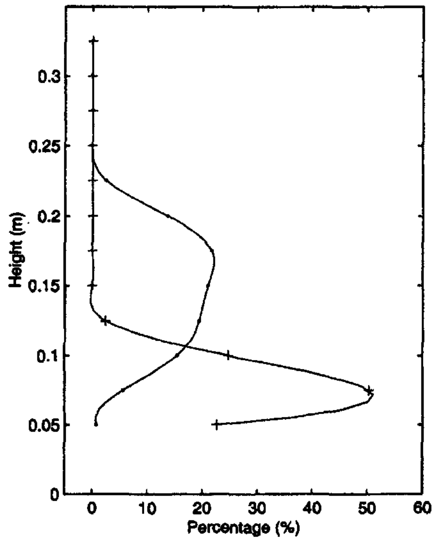

Fig. 2.11. Vertical distribution of force exerted on the front of a rectangular structure. Dry bottom (crosses) and wet bottom (circles). (Experiments were performed by Yeh and Petroff, see Gomez-Gesteira and Dalrymple, 2004)

Arnason (2005) studied the interaction of a hydraulic bore with free-standing structures (with rectangular, rhomboidal and circular cross sections) on a dry bed. The experiments were conducted using a 16.6 m long, 0.61 m wide tank where the bore was generated using impoundment depths of up to 0.3 m (Fig. 2.12). The flow profile was recorded using wave gauges and a laser profiler. The energy and momentum of flow were analyzed using data gathered by particle image velocimetry and a laser Doppler velocimeter that recorded the two-dimensional flow field and flow velocities at single points, respectively.

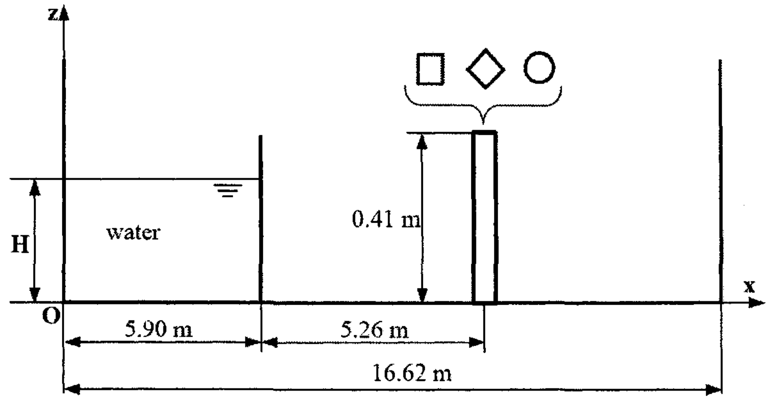

Fig. 2.12. Side view of experimental set-up, Arnason (2005).

The structures were attached to a six degree-of-freedom load cell that recorded exerted forces during the passage of hydraulic bores. It was observed that the initial impact (surge force) overshot the force due to the passing bore in the case of a square column for small bore heights as shown in Fig. 2.13. On the other hand, this overshoot was not observed for larger bore heights. Also, no overshoot was recorded for the case of circular columns (Fig. 2.14) and rhomboidal columns.

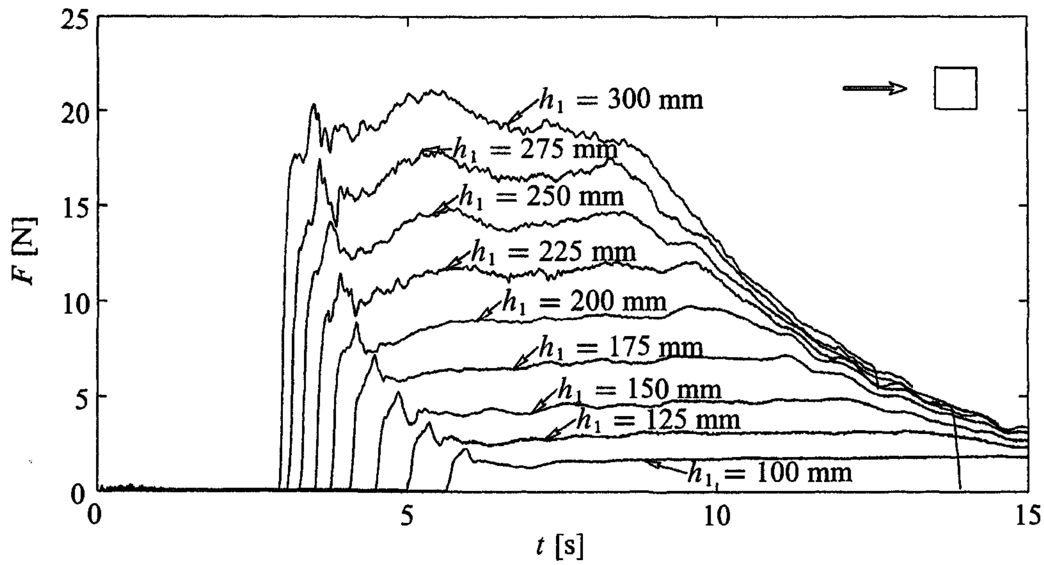

Fig. 2.13. Time history of exerted force on a square structure due to bores of varying heights (Arnason 2005).

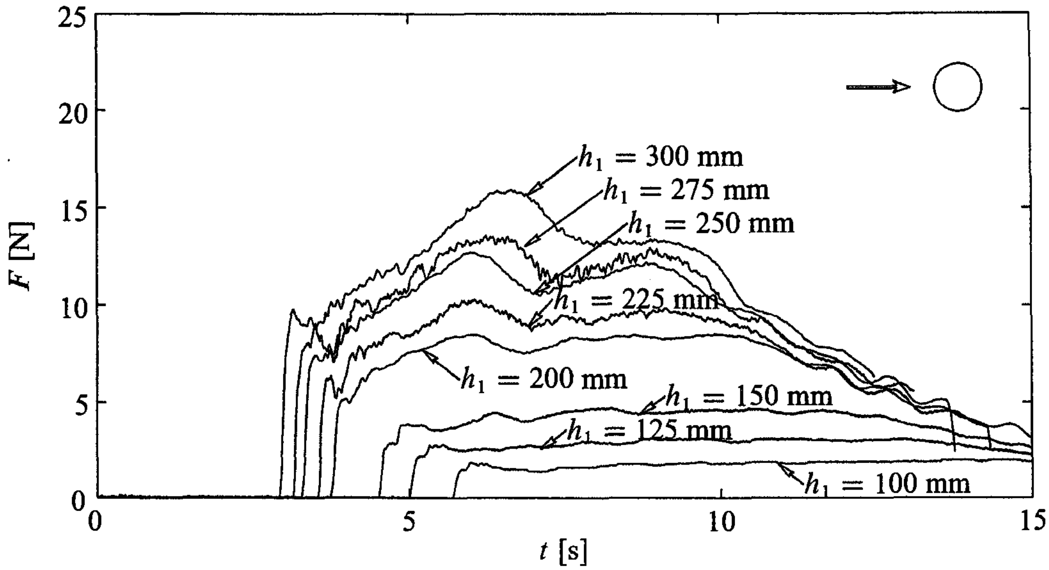

Fig. 2.14. Time history of exerted force on a circular structure due to bores of varying heights (Arnason 2005).

2.4. Debris impact Force

Matsutomi (1999) performed small- and full-scale experiments on the impact forces generated by driftwood impacting rigid structures. Dam-break waves generated in a small flume carried pieces of lumber to the point of impact on a downstream wall. Also, full-scale experiments in which wooden logs impacted a frame were conducted in open air and impact forces were measured. An empirical formula for estimating the impact force, F, was derived using regression analysis of collected data (Eq. 2.13).

$$\frac{F}{\gamma_w D^2 L} = 1.6 C_M \left(\frac{u}{\sqrt{gD}} \right)^{1.2} \left(\frac{\sigma_f}{\gamma_w L} \right)^{0.4} \tag{2.13}$$

where γ_w is the specific weight of wood, D is the diameter of the log, L is the length of the log, C_M is a coefficient which depends on the flow passing around the receiving wall ($\approx$ 1.7 for bore or surge, and 1.9 for steady flow), u is the velocity of the log at impact, and σ_f is the yield stress of the log. Fig. 2.15 shows a design chart based on Eq. 2.13.

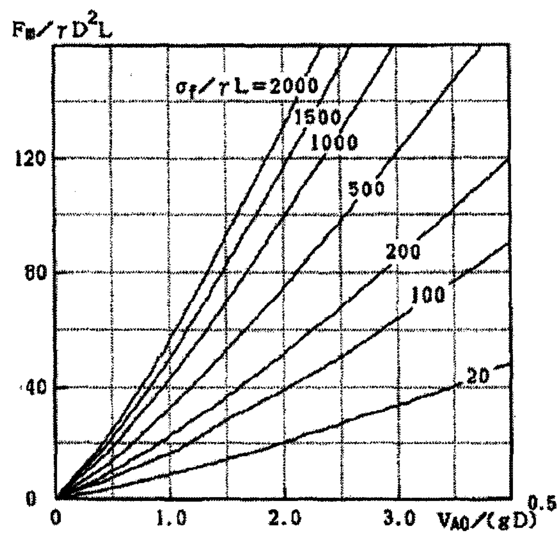

Fig. 2.15. Impact forces due to wood logs carried by bores and surges (Matsutomi 1999).

Currently, three basic models are proposed for estimating forces due to impact of debris on structures, which are used by a few design codes. In these models, the impact force is calculated based on the mass and velocity of debris, while ignoring the mass and rigidity of the structure. However, other than the mass and velocity of debris, each model needs an additional parameter. The three models and their corresponding additional parameters are:

- **Contact Stiffness** – stiffness between debris and structure,
- **Impulse-Momentum** – stopping time of debris after impact and time history of impact,
- **Work Energy** – distance travelled from where initial contact occurs, to where debris stops.

For example, maximum impact force, $F_{i,max}$, in contact stiffness method can be calculated using Eq. 2.14.

$$F_{i,\max} = Max\langle \hat{k}x \rangle = u\sqrt{\hat{k}m_1} \qquad (2.14)$$

where u is the impact velocity of the log, $\hat{k}$ is the constant effective stiffness between the log and the structure, and m_1 is the mass of the log. Haehnel and Daly (2002, 2004) used a single degree-of-freedom model with effective collision stiffness as an additional parameter. They reviewed the current models discussed above and demonstrated that none of the additional parameters are independent. Hence, the three models are equivalent, provided that the additional parameters are appropriately selected. Further, small- and large-scale experiments were performed in order to develop the single degree-of-freedom model. Small-scale tests were performed in a flume where wooden logs released into the flow impacted a load frame located further downstream. Large-scale experiments were performed in a large basin where water was stationary and logs were placed on a movable carriage. The effect of parameters such as added mass of the water and the eccentricity and obliqueness of the collision were also considered. Fig. 2.16 shows the effect of impact orientation on the measured force. Based on these experiments, Haehnel and Daly (2002) found the value of $\hat{k} = 2.4$ MN/m to be representative for the upper envelope of the collected data that could be used in Eq. 2.14 to compute debris impact forces.

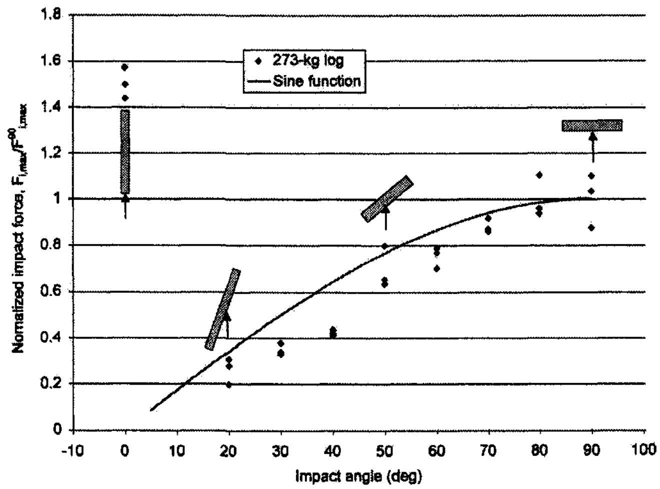

Fig. 2.16. Effect of impact orientation on force (Haehnel and Daly 2002).

2.5. Conclusion

The literature survey indicates that there is limited research on the vertical distribution of exerted forces and pressures due to bores on walls and free standing structures and demonstrates the need for further research. Also, effects of other parameters such as obstacles located upstream of the structure on the exerted forces have not been investigated. Since scale effects have significant effect on forces and pressures exerted due to bores, experimental studies with larger scales should be performed in order to verify the current understanding of the bore-structure interaction. The effects of floating debris on the characteristics of bores should also be further investigated.

Chapter 3. Tsunami-Induced Design Forces

The existing codes for structural design of onshore structures are introduced in the present chapter. This chapter also outlines the tsunami-induced force components, providing a brief description, along with the existing analytical and empirical formulae to calculate each of the components. In addition, shortcomings and discrepancies among the existing codes with regard to tsunami-induced forces are highlighted. Furthermore, loading combinations for the force components are described.

3.1. Existing Codes and Guidelines

The design of structures in flood prone areas has previously been investigated and is well established. On the contrary, only few existing codes specifically address the design of onshore structures built in tsunami prone areas. Post-tsunami field investigations of the December 2004 Indian Ocean Tsunami documented the extensive damage resulting from the extreme loads generated by tsunami inundation flow (Ghobarah *et al.* 2006 and Nistor *et al.* 2006), and outlined the need for developing new design guidelines. Tsunami-induced forces and the impact of debris are not properly accounted for in existing codes and significant improvement is needed. There are several design codes (sometimes country-specific) which contain prescriptions and design guidelines for flood induced loads. Examples of the widely used codes are indicated below:

- 1997 Uniform Building Code, Appendix 33, proposed by the International Conference of Buildings Officials (ICBO),
- ASCE 7-05 of the American Society of Civil Engineers, and
- 2006 International Building Code by the International Code Council.

However, none of the above codes address tsunami-induced forces directly, which represents the focus of this chapter. These codes provide guidance for the design of structures subjected to flood-induced loads other than tsunamis: coastal flooding due to storm surges, flooding of river banks above bank-full conditions, etc. At present, only four design codes and guidelines specifically account for tsunami-induced loads as listed below:

- FEMA 55: The code is adopted by the Federal Emergency Management Agency, US, and recommends formulae for tsunami-induced flood and wave loads,
- The City and County of Honolulu Building Code (CCH): The code, developed by the Department of Planning and Permitting of Honolulu, Hawaii, US, makes provisions for regulations that apply to districts located in flood and tsunami-risk areas,
- Structural Design Method of Buildings for Tsunami Resistance (SMBTR): The code is proposed by the Building Center of Japan (Okada *et al.* 2005) and outlines structural design for tsunami refuge buildings, and
- Development of Guidelines for Structures that Serve as Tsunami Vertical Evacuation Sites: The guidelines were prepared by Yeh *et al.* (2005) for estimating tsunami-induced forces on structures for the Washington State Department of Natural Resources.

It should be noted that Okada *et al.* (2006) have published another document titled "Tsunami Loads and Structural Design of Tsunami Refuge Buildings". There are few minor differences between the new document and SMBTR.

3.2. Tsunami-Induced Forces

A broken tsunami wave running inland generates forces that affect structures located in its path. Three parameters are essential for defining the magnitude and application of these forces: (1) inundation depth, (2) flow velocity and (3) flow direction. The parameters mainly depend on: (a) tsunami wave height and wave period; (b) coastal topography and (c) roughness of the coastal inland. Forces associated with tsunami bores consist of: (1) hydrostatic force, (2) hydrodynamic (drag) force, (3) buoyant force, (4) surge force and (5) impact of debris. A brief description of these forces is presented below.

3.2.1 Hydrostatic Force

The hydrostatic force is generated by still or slow-moving water acting perpendicular to planar surfaces. The hydrostatic force per unit width (F_{HS}) can be calculated using Eq. 3.1, which is proposed by CCH and accounts for the velocity head. Alternatively, FEMA 55 does not include the velocity head in its formulation since it is assumed to be a negligible component of the hydrostatic force.

$$F_{HS} = \frac{1}{2}\rho g\left(d_S + \frac{u_p^2}{2g}\right)^2 \tag{3.1}$$

where ρ is the sea water density, g is the gravitational acceleration, d_s is the inundation depth and u_p is the normal component of velocity against a wall.

The point of application of the resultant hydrostatic force is located at one third from the base of the triangular hydrostatic pressure distribution. In the case of a broken tsunami wave, the hydrostatic force is significantly smaller than the drag and surge forces. Conversely, Dames and Moore (1980) noted that the hydrostatic force becomes important when the tsunami is similar to a rapidly-rising tide.

3.2.2 Buoyant Force

The buoyant force is the vertical force acting through the center of mass of a submerged body. Its magnitude is equal to the weight of the volume of water displaced by the submerged body. The effect of buoyant forces generated by tsunami flooding was clearly evident during post-tsunami field observations (Nistor *et al.* 2006 and Saatcioglu *et al.* 2006a,b). Buoyant forces can generate significant damage to structural elements such as floor slabs, and are calculated as follows (Eq. 3.2):

$$F_B = \rho g V \tag{3.2}$$

where V is the volume of water displaced by submerged structure.

3.2.3 Hydrodynamic (Drag) Force

As a tsunami bore moves inland with moderate to high velocity, structures are subjected to hydrodynamic forces caused by drag. Currently, there are differences in estimating the magnitude of the hydrodynamic force. The general expression for this force is shown in

Eq. 3.3. Existing codes use the same expression, but different drag coefficient values (C_D). For example, values of 1.0 and 1.2 are recommended for circular piles by CCH and FEMA 55, respectively. For the case of rectangular piles, the drag coefficient recommended by FEMA 55 and CCH is 2.0.

$$F_D = \frac{\rho C_D A u^2}{2} \tag{3.3}$$

where F_D is the total drag force acting in the direction of flow, A is the projected area of the body normal to the flow direction and u is the bore velocity.

The flow is assumed to be uniform, so the resultant force will act at the centroid of the projected area. As indicted, the hydrodynamic force is directly proportional to the square of the tsunami bore velocity. The estimation of the bore velocity remains one of the critical elements on which there is significant disagreement in the literature. A brief discussion on the tsunami-bore velocity is presented below.

Tsunami-bore Velocity:

Previous research shows that significant differences in estimating forces exerted on structures by tsunami bores, as well as impact of debris, are due to differences in estimating bore velocity. Since the hydrodynamic and debris impact force are proportional to the bore velocity with a power of two and one respectively, uncertainties in estimating velocities induce large differences in the magnitude of the resulting forces. Tsunami-bore velocity and direction can vary significantly during a major tsunami inundation. Current estimates of the velocity are crude; a conservatively high flow velocity impacting the structure at a normal angle is usually assumed. Also, the effects of runup, backwash and direction of velocity are not addressed in current design codes.

Although there is certain consensus in the general form of the equation for the hydrodynamic force, many researchers proposed different empirical coefficients. The general form of the bore velocity is shown below (Eq. 3.4):

$$u = C\sqrt{g d_S} \tag{3.4}$$

where u is the bore velocity, d_S is the inundation depth and C is a constant coefficient.

Various formulations were proposed by FEMA 55 (based on Dames and Moore (1980)), Iizuka and Matsutomi (2000), CCH, Kirkoz (1983), Murty (1977), Bryant (2001) and Camfield (1980) for estimating the velocity of a tsunami bore in terms of inundation depth (Fig. 3.1). Velocities calculated using CCH and FEMA 55 represent a lower and upper boundary, respectively.

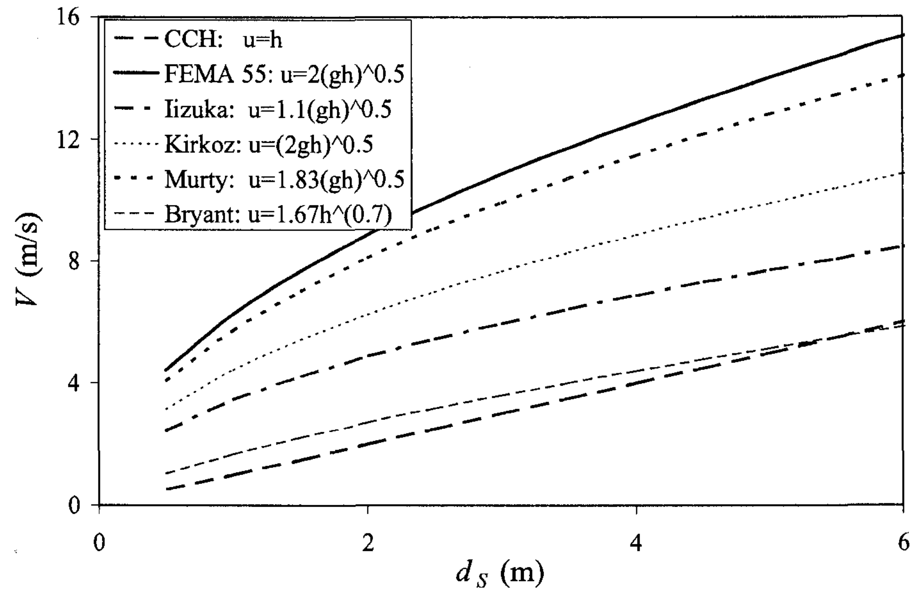

Fig. 3.1. Comparison of various tsunami-bore velocities as a function of inundation depth, Nouri *et al.* (2007).

3.2.4 Surge Force

The surge force is generated by the impingement of the advancing water front of a tsunami bore on a structure. Due to a lack of detailed experiments specifically applicable to tsunami bores running up the shoreline, the calculation of the surge force exerted on a structure is subject to substantial uncertainty. Accurate estimation of the impact force in laboratory experiments is a challenging and difficult task. CCH recommends using Eq. 3.5 (based on Dames and Moore (1980)).

$$F_S = 4.5\rho g h^2 \tag{3.5}$$

where F_S is the total surge force per unit width of wall and h is the surge height.

The point of application of the resultant surge force is located at a distance h above the base of the wall. This equation is applicable for walls with heights equal to, or greater than $3h$. Structural walls with height less than $3h$ require surge forces to be calculated using an appropriate combination of hydrostatic and drag force for each specific situation.

SMBTR recommends using the equation for tsunami wave pressure without soliton break up derived by Asakura *et al.* (2001) (Eq. 3.6). The equivalent static pressure resulting from the tsunami impact is associated with a triangular distribution where water depth equals three times the tsunami inundation depth.

$$qx = \rho g\left(3h_{\max} - z\right) \tag{3.6}$$

where qx is the tsunami wave pressure for structural design, z is the height of the relevant portion from ground level ($0 \le z \le 3h$), ρ is the mass per unit volume of water and g is the gravitational acceleration (Fig. 3.2).

Integration of the wave pressure formula for walls with heights equal to or greater than $3h$ results in the same equation as the surge force formula recommended by CCH (Eq. 3.5). The magnitude of the surge force calculated using Eqs. 3.5 and 3.6 will generate a value equal to nine times the magnitude of the hydrostatic force for the same flow depth. However, a number of experiments (Ramdsen 1993, Arnason 2005) did not capture such differences in magnitude. Yeh *et al.* (2005) commented on the validity of Eq. 3.5 and indicated that this equation gives "excessively overestimated values". On the other hand, Nakano and Paku (2005) conducted extensive field surveys in order to examine the validity of the proposed tsunami wave pressure formula (Eq. 3.6). The coefficient 3.0 in Eq. 3.6 was taken as a variable, α, and was calculated such that it could represent the boundary between damage and no damage in the surveyed data. A value of α equal to 3.0 and 2.0 was found for walls and columns, respectively. The former is in agreement with the proposed formulae by both CCH and SMBTR (Eqs. 3.5 and 3.6).

The tsunami wave force may be composed of drag, inertia, impulse and hydraulic gradient components. However, SMBTR does not specify different components for the tsunami-induced force, and the proposed formula presumably accounts for other components.

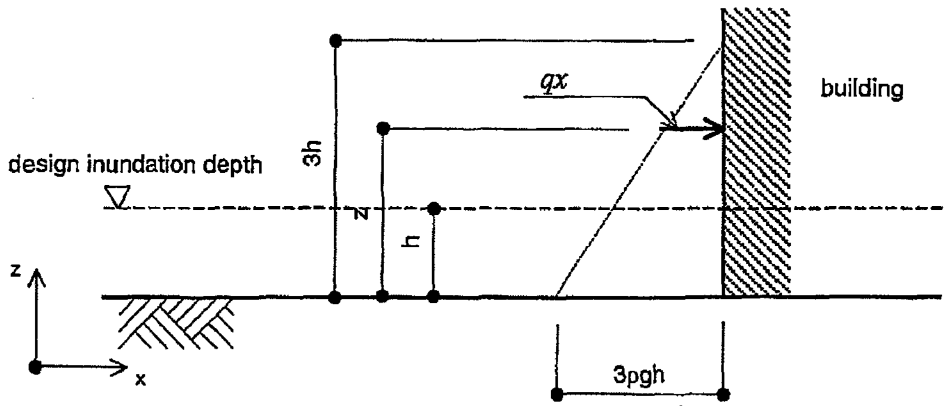

Fig. 3.2. Tsunami wave pressure distribution, without soliton break-up for structural design recommended by SMBTR (based on Asakura *et al.* (2000)).

3.2.5 Debris Impact Force

A high-speed tsunami bore traveling inland carries debris such as floating automobiles, floating pieces of buildings, drift wood, and boats and ships. The impact of floating debris can induce significant forces on a building, leading to structural damage or collapse (Saatcioglu *et al.* 2006a,b). Both FEMA 55 and CCH codes account consistently for debris impact forces, using the same approach and recommend using Eq. 3.7 for estimation of debris impact force.

$$F_i = m_b \frac{du_b}{dt} = m \frac{u_i}{\Delta t} \tag{3.7}$$

where F_i is the impact force, m_b is the mass of the body impacting the structure, u_b is the velocity of the impacting body (assumed equal to the flow velocity), u_i is the approach velocity of the impacting body (assumed equal to the flow velocity) and Δt is the impact duration taken equal to the time between the initial contact of the floating body with the building and the instant of maximum impact force.

The only difference between CCH and FEMA 55 resides in the recommended values for the impact duration which has a noticeable effect on the magnitude of the force. For example, CCH recommends the use of impact duration of 0.1 seconds for concrete structures, while FEMA 55 provides different values for walls and piles for various construction types as shown in

Table 3.1.

Table 3.1. Impact duration of floating debris (FEMA 55).

Type of Construction	Impact Duration (seconds)	
	Walls	Piles
Wood	0.7 – 1.1	0.5 – 1.0
Steel	N.A.	0.2 – 0.4
Reinforced Concrete	0.2 – 0.4	0.3 – 0.6
Concrete Masonry	0.3 – 0.6	0.3 – 0.6

According to FEMA 55, the impact force (a single concentrated load) acts horizontally at the flow surface or at any point below it. Its magnitude is equal to the force generated by 455 kg (1000 lb) of debris traveling at the bore velocity and acting on a 0.092 m^2 (1 ft^2) surface of the structural element. The impact force is to be applied to the structural element at its most critical location, as determined by the structural designer. It is assumed that the velocity of the floating body varies from u_b to zero over some small finite time interval (Δt). Finding the most critical location of impact is a trial and error procedure that depends, to a large extent, on the experience and intuition of the engineer.

3.2.6 Breaking Wave Force

Tsunami waves tend to break offshore and approach a shoreline as a broken hydraulic bore or a soliton, depending on wave characteristics and coastal bathymetry. Consequently, classic breaking wave force formulae are not directly applicable to the case of tsunami bores. Hence, this chapter does not discuss the estimation of breaking wave forces.

3.3. Loading Combinations for Tsunami-Induced Forces

Based on the location and type of structural elements, appropriate combinations of tsunami-induced force components (hydrostatic, hydrodynamic, surge, buoyant and debris impact force) should be used in calculating the total tsunami force. This is due to the fact that a certain element may not be subjected to all of these force components simultaneously. Loading combinations can significantly influence the total tsunami force and the subsequent structural design. Unlike the case of tsunami waves, loading combinations for flood-induced surges are well-established and have been included in design codes. The literature review revealed that proposed tsunami loading combinations must be significantly improved and incorporated in new design codes. Tsunami-induced loads are different from flood-induced loads. Therefore, load combinations based on flood surges are not directly applicable to tsunamis. Loading combinations proposed in the literature are as follows:

- **FEMA 55** does not provide loading combinations specifically for calculation of tsunami force. However, flood load combinations can be used as guidance. Flood load combinations for piles or open foundations, as well as solid walls (foundation) in flood hazard zones and coastal high hazard zones are presented as follows:

  Pile or open foundation:

  F_{brkp} (on all piles) + F_i (on one corner or critical pile only), or

  F_{brkp} (on front row of piles only) + F_{dyn} (on all piles but front row) + F_i (on one corner or critical pile only).

  Solid (wall) foundation:

  F_{brkw} (on walls facing shoreline, including hydrostatic component) + F_{dyn} (assumes one corner is destroyed by debris).

  where F_{brkp}, F_i, F_{dyn} and F_{brkw} refer to the breaking force on piles, impact force, hydrodynamic force, and breaking force on walls, respectively.

- **Yeh *et al.*** (2005) modified flood load combinations provided by FEMA 55 and adapted them for tsunami forces as follows:

Columns:

F_{brkp} (on column) + F_i (on column), or

F_d (on column) + F_i (on column).

Solid (wall) foundation (perpendicular to flow direction):

F_{brkw} (on walls facing shoreline) + F_i (on one corner), or

F_S (on walls facing shoreline) + F_i (on one corner), or

F_d (on walls facing shoreline) + F_i (on one corner).

where F_{brkp}, F_i, F_d, F_S and F_{brkw} refer to the breaking force on piles or columns, impact force, hydrodynamic force, surge force on walls and breaking force on walls, respectively.

- **Dias *et al.*** (2005) proposed two load combinations called 'point of impact' and 'post-submergence/submerged' (Fig. 3.3). These load combinations are based on two conditions: (i) the instant that tsunami-bore impacts the structure, and (ii) when the whole structure is inundated, and are presented as follows:

Point of Impact:

F_d (on walls facing shoreline) + F_S (on walls facing shoreline).

Post-submergence/Submerged:

F_d (on walls facing shoreline) + F_b (on submerged section of the structure).

where F_S is defined as the hydrostatic force while $F_b = \gamma V$ is the buoyant force (γ is the unit weight of sea water and V is the volume of the submerged section of the structure).

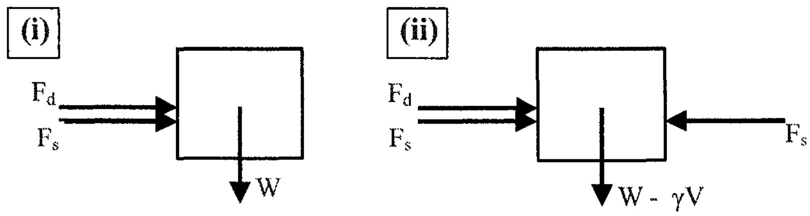

Fig. 3.3. Loading combinations: (i) point of impact/not submerged; and (ii) post-submergence/submerged (Dias *et al.* 2005).

- **Nouri *et al.*** (2007) proposed load combinations based on the two conditions considered by Dias *et al.* (2005), as shown in Fig. 3.4. The load combinations proposed by Nouri *et al.* (2007) are adapted to follow a consistent format as the above combinations:

<u>Columns:</u>

F_S (on front row of columns only) + F_i (on one critical column in the front row only), or

F_d (on all columns) + F_i (on one critical column only).

<u>Solid (wall) foundation (perpendicular to flow direction):</u>

F_S (on walls facing shoreline) + F_i (on one corner), or

F_d (on walls facing shoreline) + F_i (on one corner) + F_b (on submerged section of the structure).

where F_S, F_i , F_d and F_b refer to the surge force on walls and columns, debris impact force, hydrodynamic force and buoyant force, respectively.

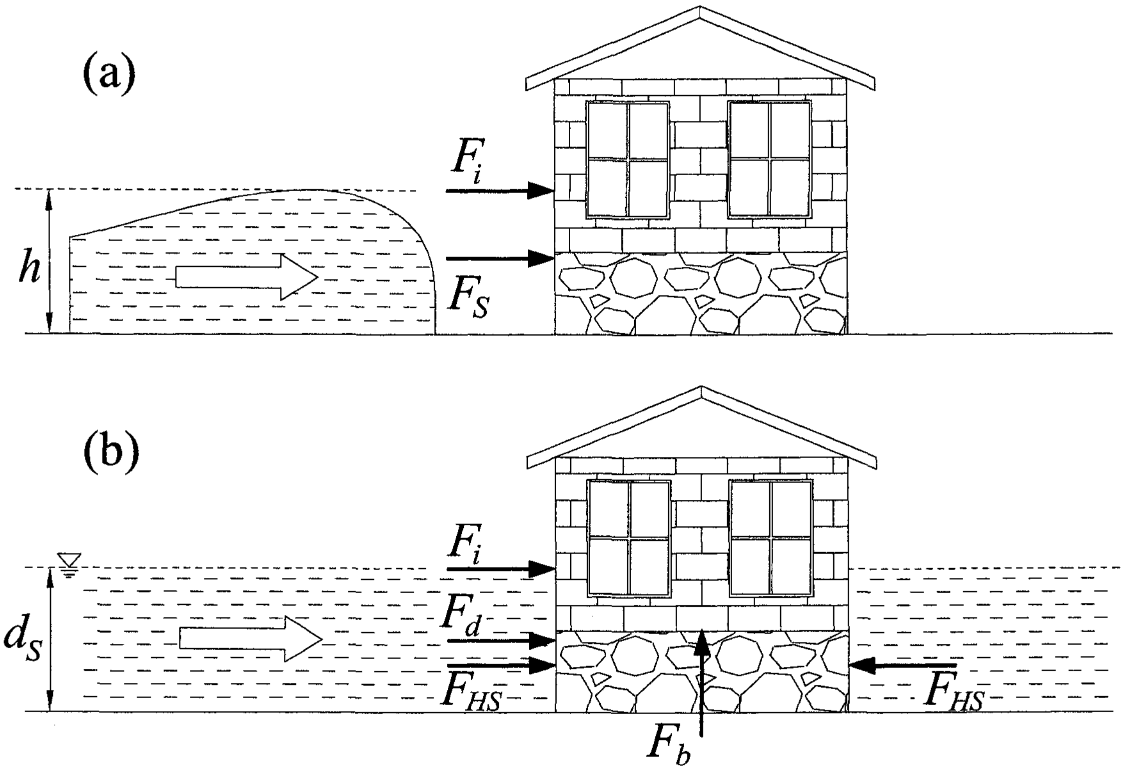

Fig. 3.4. Proposed loading conditions: (a) point of impact; and (b) post-impact, (Nouri *et al.* 2007).

Chapter 4. Experimental Program

4.1. Experimental Set-up

4.1.1 Facilities

The experimental program was carried out in a 10.6 m long, 2.7 m wide and 1.4 m deep high discharge flume at the Canadian Hydraulics Centre, National Research Council of Canada (NRC-CHC), in Ottawa. The experiments were performed in a 1.3 m wide channel formed by erecting a temporary partition wall within the 2.7 m wide flume. The discharge in the flume could be continuously adjusted from 0 to 1.7 m^3/s using a variable pitch pump. The water level is controlled by an adjustable sluice gate at the downstream end of the flume. The flume has two side windows to enable visualization of the flow. A steel frame was installed on the top of the flume and supported a crane that could be used for moving objects in the flume. A schematic figure of the flume is presented in Fig. 4.1.

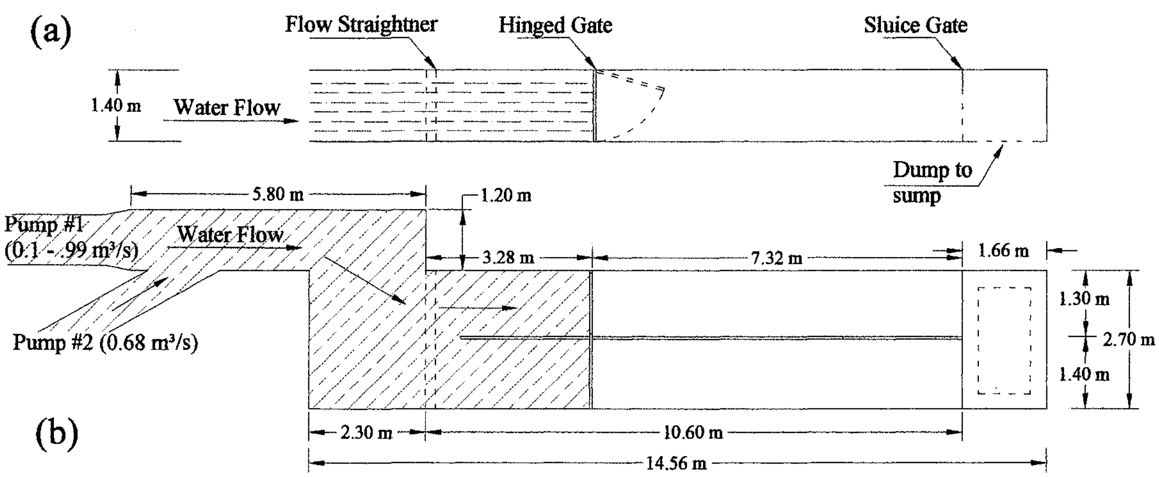

Fig. 4.1. Outline of the high discharge flume: (a) side view; (b) plan view.

The various test structures were located near the centre of the side windows in order to make visualization and capturing videos of flow profile possible. A removable gate comprised of a stainless steel frame covered with plywood sheets was constructed. The gate was located such that a relatively large reservoir (approximately 5.6 m long) was provided upstream of the gate in order to hold a reasonably large volume of water behind the gate. Fig. 4.2 shows a schematic layout of the flume where the location of the gate and structures is specified. In this figure, x is the horizontal axis along the flume.

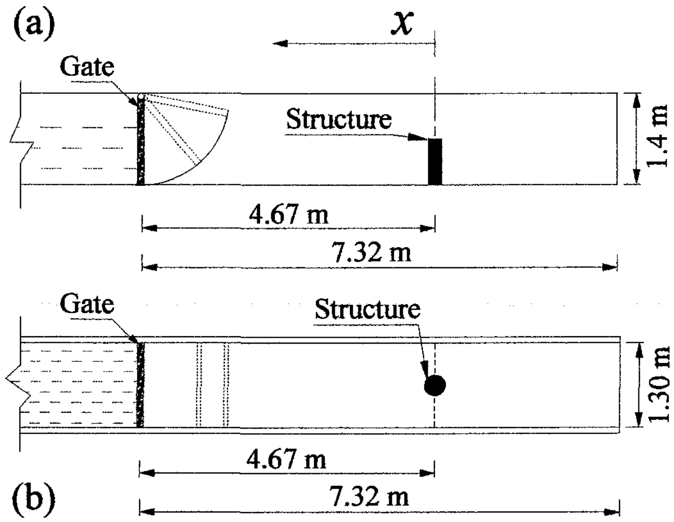

Fig. 4.2. Layout of the flume and position of the column.

The gate was hinged at the top and secured with a locking system, which could be opened by means of a 2000 N electric winch. A counter-weight mechanism provided adequate leverage to hold the gate open after its release. Rectangular steel channels (5.08×5.08×1400 cm) were welded to the sides of the flume and strips of plywood were screwed to the steel channels that the gate rested on. Rubber gaskets were installed to minimize leakage when the gate was closed. However, there was a thin layer of water (approximately 6 mm) downstream of the gate. Fig. 4.3 shows the preparation of the flume and the construction of the gate, whereas Fig. 4.4 shows downstream and upstream views of the gate.

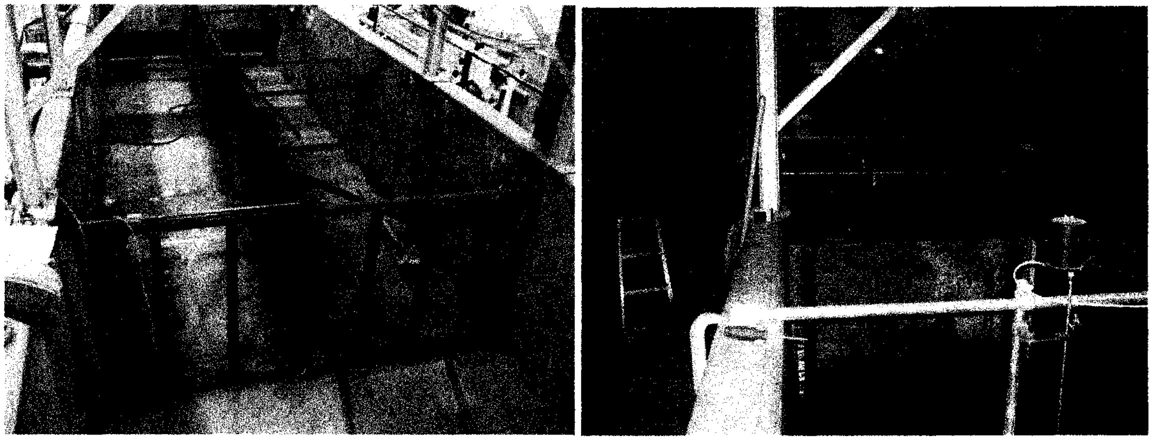

(a) (b)

Fig. 4.3. The high discharge flume: (a) preparation of the flume and gate; (b) flume and the gate in operation.

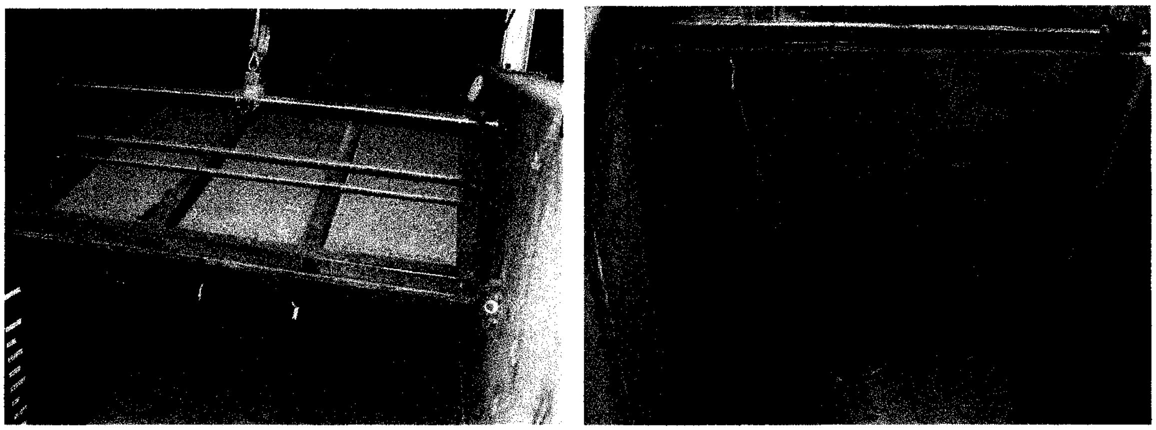

(a) (b)

Fig. 4.4. The hinged gate: (a) downstream view; (b) upstream view.

The opening time, evaluated from digital video recordings, was 0.7 s. The time it took the gate to separate from the water surface varied between 0.35 s and 0.42 s, depending on the impoundment depth (the initial still water level upstream of the gate when the gate is closed), h_0. Fig. 4.5 shows that the gate has separated from the water surface in 0.45 s for an impoundment depth of $h_0 = 0.5$ m.

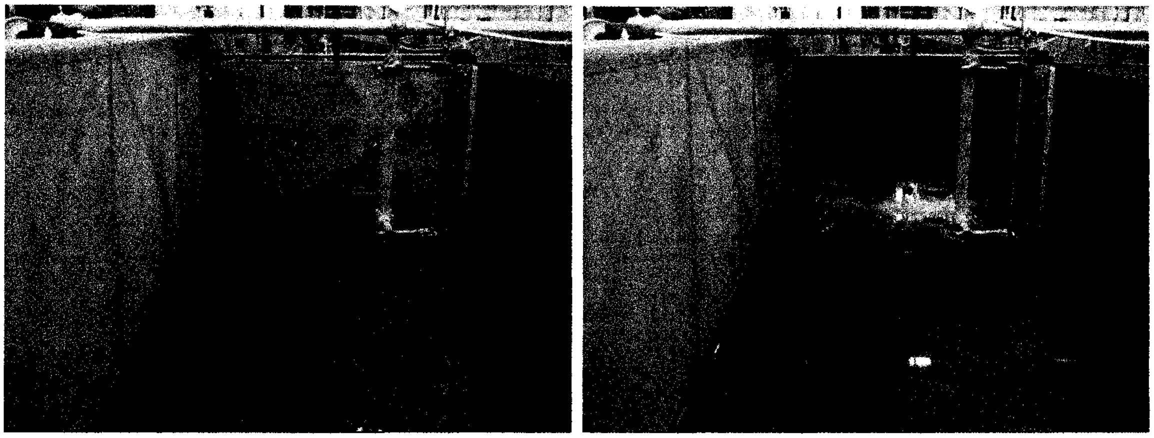

(a) (b)

Fig. 4.5. The opening time of the gate for $h_0 = 0.5$ m: (a) the gate is opened at $t = 0.0$ s; (b) the gate has separated from the water surface at $t = 0.45$ s.

4.1.2 Methodology

In order to perform the tests, first, the test structure and the measurement devices were located at the specified positions (as explained later in Sec. 4.6) and the gate was closed and locked. Next, the reservoir, located upstream of the gate (approximately 5.6 m long and 2.7 m wide), was filled with water up to the specified impoundment depth using the variable pitch pump. As the water level in the reservoir approached the specified impoundment depth, the pump blade pitch was adjusted to ensure that at the instant of the gate opening the water level was approximately constant during the test. Also, the data acquisition system was turned on and data recording started at this stage. Then, as soon as the water level reached the specified impoundment depth, the electric winch was manually operated to release the lock and open the gate. The gate swung open and the water flowed downstream as a hydraulic bore past the test structure while various data were recorded.

Fig. 4.4 shows the gate extended to the full width of the flume. It was therefore expected that a two-dimensional flow would be generated. However, the gate rested on 0.08 m wide ledges that acted as a constriction to the flow. These constrictions induced cross waves (i.e. three-dimensional effects) downstream of the gate. These cross waves initiated from the location of the ledges and extended approximately 1.5 m downstream of the gate. Since the test structures were located further downstream of the point, their existence could not have affected the exerted forces significantly. Bore characteristics are studied in Sec. 5.2.2 in order to address the possible influence of these three-dimensional features.

A number of steel pipes were installed on the top of the flume along and across the longitudinal axis of the flume forming a frame that could be easily moved (Fig. 4.6). The pipes were attached to each other using key clamps and fixed on the flume sides using C clamps. Other pipes were attached vertically to this frame using key clamps. Wave gauges and acoustic Doppler velocimeters (ADVs) were mounted to these vertical pipes. These measurement devices could be positioned at any location and height above the bottom of the flume. Bubble levels were used to ensure that the measurement devices were positioned vertically.

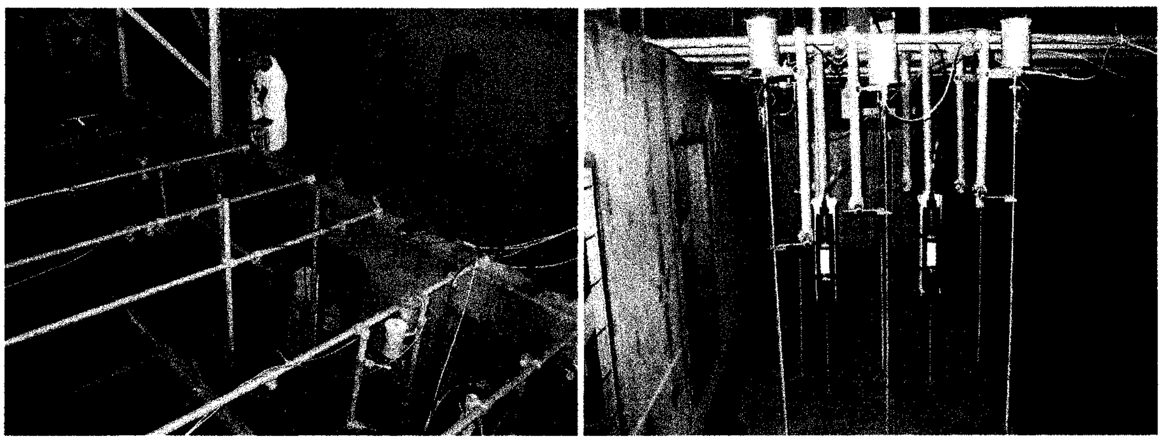

(a) (b)

Fig. 4.6. Wave gauges and ADVs were mounted on vertical pipes attached to a frame of pipes.

4.2. Instrumentation

4.2.1 Capacitance Wave Gauges

Seven wave gauges were used to measure water levels and the bore height at various locations throughout the experiment. Each wave gauge consists of a wire (≈ 0.6-0.7 m long) and a head containing electronic components connected to the data acquisition system. The capacitance of the wire changes, depending on the length of the wire that is wet. The head is connected to the data acquisition system. The voltage measured from the wire is proportional to the resistance of the wire. The accuracy of the wave gauges used for the experiments is of the order of millimetres. Attention must be paid in mounting the wave gauges in the flume, as they should be installed vertically. As explained in Sec. 4.1.2, wave gauges were mounted on the vertical pipes that were attached from the top to the horizontal lead pipes (Fig. 4.7). Sampling rate of data collection for the wave gauges was set to 1 kHz. It should be noted that the wave gauges were installed in a way that the end of the wire was located approximately 1 to 2 cm above the bottom of the flume. Therefore, they start to measure water level approximately 2 cm above the bottom of the flume.

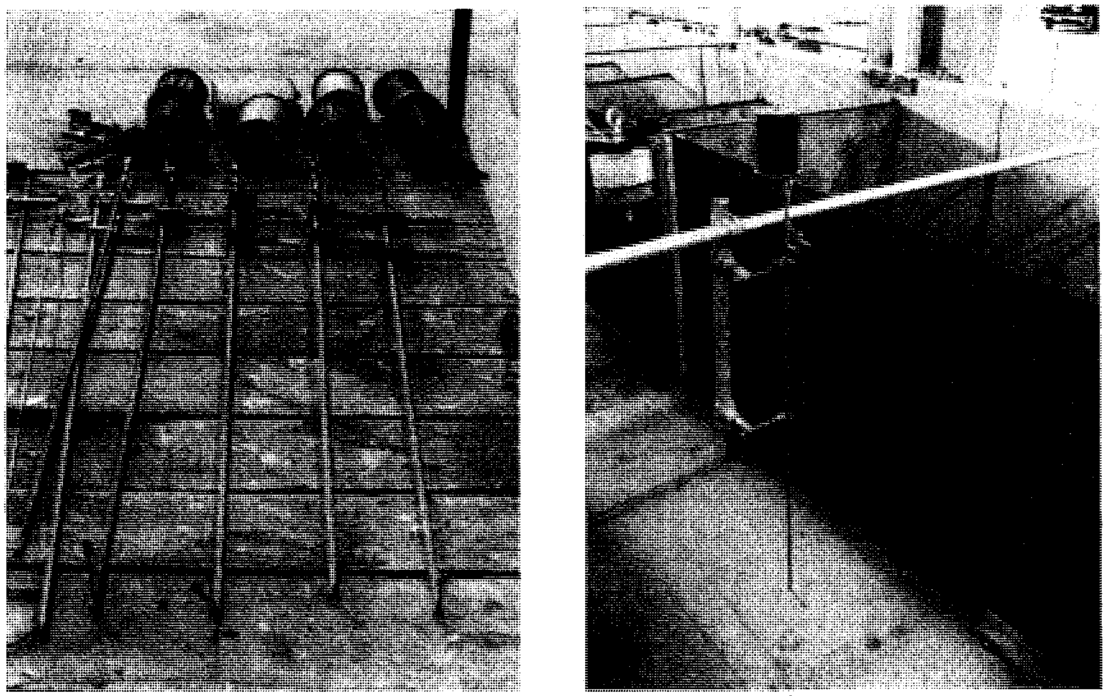

(a) (b)

Fig. 4.7. Wave gauges: (a) head and a wire; (b) mounted on the vertical pipes.

Calibration of wave gauges

A linear relation exists between the resistance of wire, i.e., water depth and the measured voltage. Calibration should be performed to find the slope of the line. Theoretically, the slope of the line can be found using two points. However, using more points increases the accuracy. For this experimental program, five points were used for the calibration of each wave gauge. The obtained calibration diagram for one of the wave gauges is shown in Fig. 4.8. Further details can be found in the paper of Miles (2001).

Calibration of [illegible]0312 Channel 15 15:37 23 April 2007

Calibrated by: Younes — Calibration Status: NORMAL
Project: U of O Tsunami Project — Facility: High Discharge Flume
Sensor: WP7 — Model: Robershaw — Serial No. N/A
Programmable Gain: 1 — Plug-In Gain: 1 — Filter Frequency: 1000.0 Hz

Data Point No.	Input Signal (volts)	Physical Value (m)	Fitted Curve (m)	Error (m)
1	-0.002	0.00000	0.00000	-0.0000004
2	-0.960	-0.20000	-0.20134	-0.0013401
3	-1.901	-0.40000	-0.39919	0.0008085
4	0.953	0.20000	0.20080	0.0008029
5	1.899	0.40000	0.39973	-0.0002709
Maximum Error = -0.168% of Calibration Range				

$Y = C_0 + C_1 V$
where $Y(t)$ = Water Depth (m)
$V(t)$ = input signal at A/D converter (volts)
C_0 = 0.000521713 m
C_1 = 0.210222 m/volt

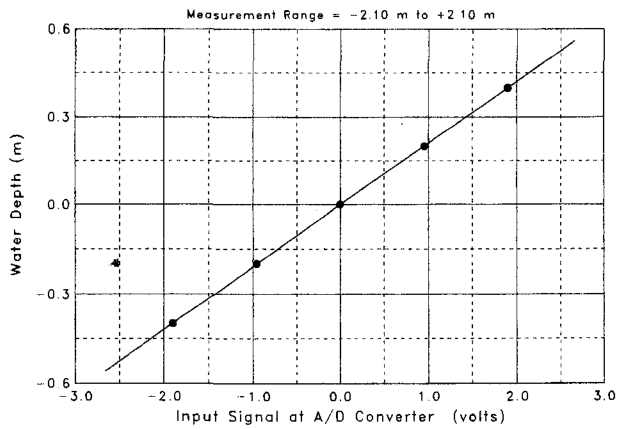

Fig. 4.8. Calibration diagram for one of the wave gauges.

Re-zeroing Wave Gauges

Before performing any tests, wave gauges should be re-zeroed. First, the adjustable sluice gate at the downstream end of the flume was closed, while the hinged gate was kept open. Next, water was added to the flume in order to obtain a constant level. A low pitch was used for the pump so that the water would not overflow the flume. The water level was checked by direct measurement through the side windows using a ruler. Also, the flow velocity was visually checked. Then, after the velocity was observed to be approximately equal to zero (no movement in the water), water level was measured repetitively every three minutes in order to ensure a constant water level. Finally, the corresponding water level was assigned to all wave gauges and the sluice gate was opened and water was released.

4.2.2 Load Cells

The load cells used in this experimental program were single-component force transducers (sealed superbeam load cell, Interface model SSB-AJ-50) capable of measuring force in two directions (tension and compression). The load cells were attached to a load bearing plate that was encased in a mount as shown in Fig. 4.9. Forces are applied to the load bearing plate that transfers the load to the load cell. In order to accurately measure the impact forces on a surface due to hydraulic bores, the load bearing plate should be flush with the surface. Because of the curved surface of the circular structure, load cells could not be mounted on the circular structure and were only used on the square structure. Load cells were calibrated and then adjusted such that the load bearing plate was perfectly flush with the surface of the mount. Thin, flexible rubber membranes were used to cover the mount in order to prevent water from going through the small gap between the load bearing plate and the mount.

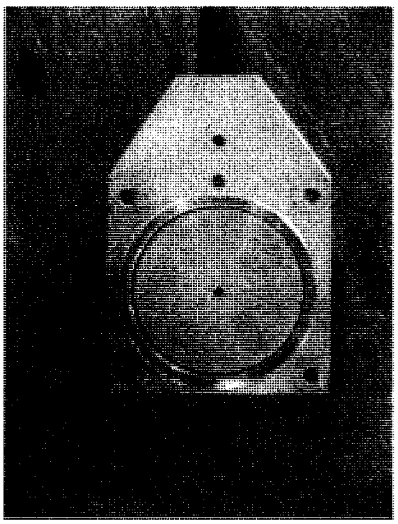
(a)

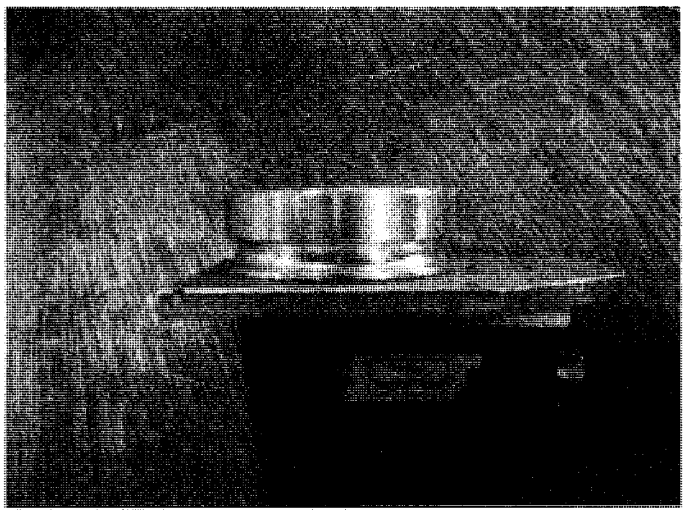
(b)

Fig. 4.9. Load cells, load bearing plates and mounts: (a) front view; (b) side view. (see Fig. 4.21 for scale)

Calibration of load cells

The amount of force applied on the load cells is converted to voltage and measured by the data acquisition system. A linear relation exists between the measured voltage and applied force. With a minimum of two points on this calibration line, any value of measured voltage can be converted to the corresponding applied force. Five points were used to derive the line and to increase the accuracy. Five load cells with a capacity of

0.222 kN (50 lbs) were used in this experimental program. The accuracy of the load cells was approximately one Newton. An example of an obtained calibration diagram for one of the load cells is shown in Fig. 4.10.

Calibration of PC16031E Channel 1   14:32   17 April 2007

Calibrated by: Younes — Calibration Status: NORMAL
Project: U of O Tsunami Project — Facility: High Discharge Flume
Sensor: FP1 — Model: Interface 50 lbs — Serial No. 77844
Programmable Gain: 1 — Plug-In Gain: 1 — Filter Frequency: 100.0 Hz

Data Point No.	Input Signal (volts)	Physical Value (kN)	Fitted Curve (kN)	Error (kN)
1	-0.046	0.00000	0.00032	0.00031637
2	-1.372	0.04906	0.04884	-0.00021789
3	-2.714	0.09812	0.09796	-0.00015911
4	-4.050	0.14718	0.14686	-0.00031996
5	-4.731	0.17171	0.17178	0.00006825
6	-5.408	0.19625	0.19656	0.00031233
Maximum Error = -0.163% of Calibration Range				

$$Y = C_0 + C_1 V$$

where $Y(t)$ = Force (kN)
$V(t)$ = input signal at A/D converter (volts)
C_0 = -0.00138061 kN
C_1 = -0.0366040 kN/volt

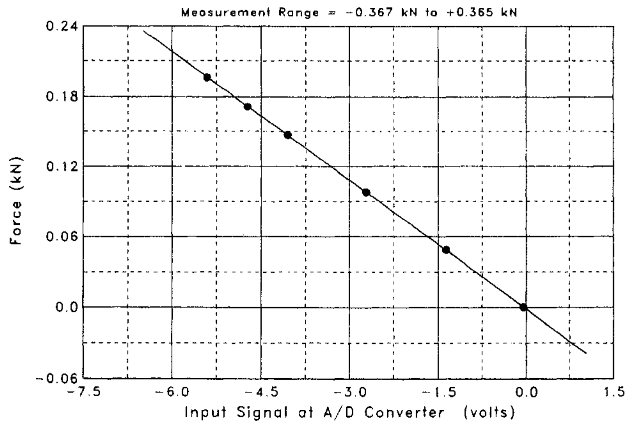

Fig. 4.10. Calibration diagram for one of the load cells.

Before performing the tests, load cells should be re-zeroed when there is no load exerted on them and no water in the flume. The load cells were sealed with a water proofing compound since, if during the tests water got inside the structure, load cell readings could no longer be accurate. Sampling rate of data collection for the load cells was set to 200 Hz.

4.2.3 Dynamometer

A multi-component dynamometer (AMTI MC6 series) was used to record the base reaction of the test structure due to the bore impact. The dynamometer was capable of measuring forces and moments in three directions (i.e. it is a six degree-of-freedom dynamometer). The dynamometer was rigidly bolted to the flume bottom as shown in Fig. 4.11. A mounting bracket was designed and fabricated to allow the cylindrical test structure to be mounted to the dynamometer, as explained in Sec. 4.3.1. The dynamometer readings were re-zeroed after the structure was mounted and before each test. The sampling rate of data collection for the dynamometer was set to 1 kHz.

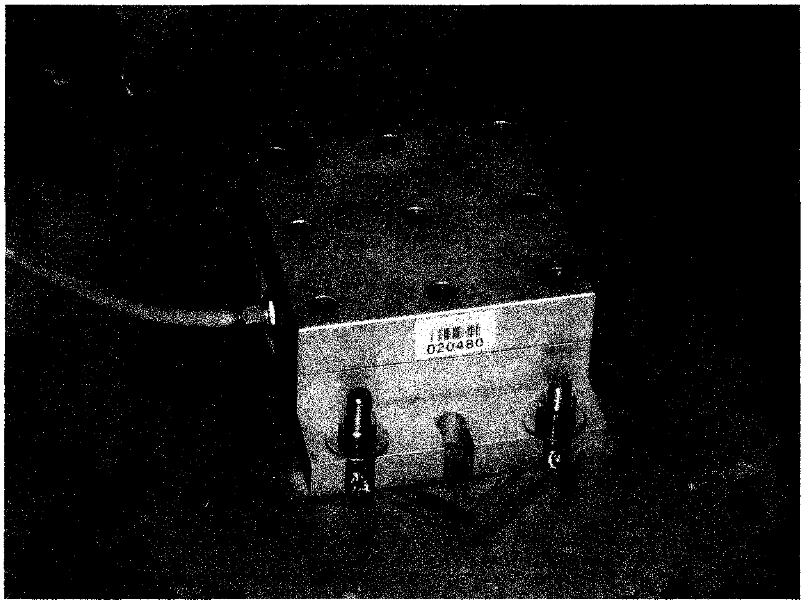

Fig. 4.11. The multi-component dynamometer bolted to the bottom of the flume.

Calibration of Dynamometer

The amount of force and moment applied on the dynamometer is converted to voltage and recorded by the data acquisition system. A linear relation exists between the measured voltage and the applied forces and moments. This linear relation depends on the sensitivity, excitation and gain of the device. The manufacturer calibrated the dynamometer before the tests and provided gain values for each component separately. The relation between the forces/moments and the measured voltage was obtained using the provided gain values and the selected values for sensitivity and citation according to the dynamometer's manual.

4.2.4 Pressure Transducers

Eleven differential pressure transducers (Honeywell model PK 80083) were used in the experiments in order to measure the exerted pressures on the upstream face and sides of the test structures due to bore impact. Each transducer was filled with two flexible transparent rubber tubes and measured the pressure difference between these tubes, (Fig. 4.12). One of the tubes was exposed to open air at the atmospheric reference pressure (P_{atm}), while the second tube was mounted flush with the surface of the test structure. The second tube was filled with coloured water in order to identify the unwanted presence of air bubbles as shown in Fig. 4.12 (b). The pressure sensors were coated in a protective water-proofing compound.

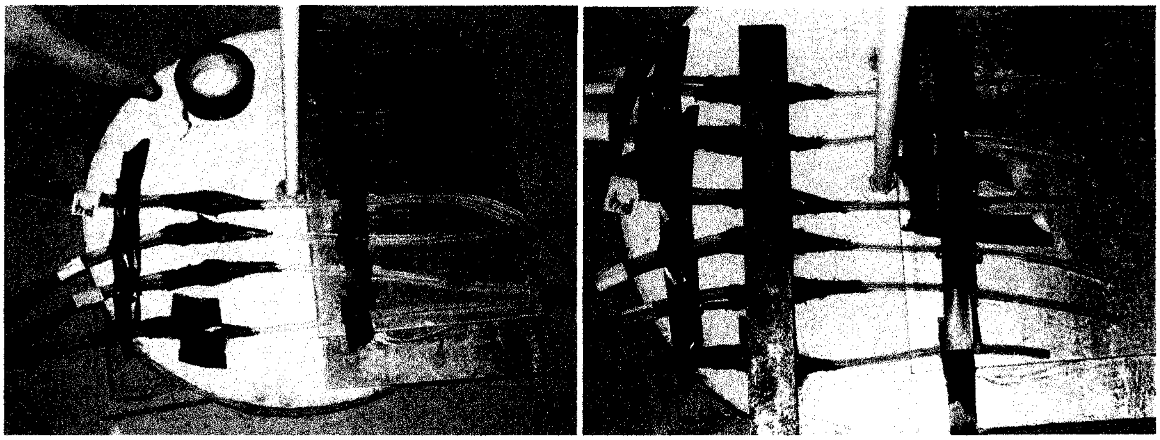

Fig. 4.12. Calibration of pressure transducers: (a) attached to a plate using tapes; (b) plastic tubes filled with a green dye.

Calibration of Pressure Transducers

The pressure difference between the two tubes connected to each sensor was converted to voltage and measured by the data acquisition system. A linear relation exists between the measured voltage and pressure difference. In order to calibrate the pressure transducers, they were attached to a steel board and placed at the bottom of a barrel. The barrel was filled with water in five steps. At each step, the water height in the barrel was measured using a ruler, while the transducer outputs were measured by the data acquisition system. The pressure corresponding to the measured water depth was calculated and assigned to the transducers. This way, five points were obtained and were used to derive the linear relation and to increase the measurement accuracy. Eleven pressure transducers were used in this experimental program with a capacity of 15.1 kPa. The accuracy of the pressure transducers was approximately one Pascal. The obtained calibration diagram for one of the pressure transducers is shown in Fig. 4.13.

[illegible] Channel 1[illegible] 13:5[illegible] 27 July 2007

Calibrated by: Younes | Calibration Status: NORMAL
Project: U of O Tsunami Project | Facility: High Discharge Flume
Sensor: PT1 | Model: N/A | Serial No. N/A
Programmable Gain: 1 | Plug-In Gain: 1 | Filter Frequency: 1.0 Hz

Data Point No.	Input Signal (volts)	Physical Value (kPa)	Fitted Curve (kPa)	Error (kPa)
1	−4.532	7.6616	7.6561	−0.0055586
2	−3.514	6.2686	6.2769	0.0082688
3	−2.773	5.2778	5.2726	−0.0051985
4	−1.798	3.9436	3.9511	0.0074687
5	−0.580	2.3054	2.3004	−0.0049825
Maximum Error = 0.154% of Calibration Range				

$Y = C_0 + C_1 V$

where $Y(t)$ = Pressure (kPa)

$V(t)$ = input signal at A/D converter (volts)

C_0 = 1.51421 kPa

C_1 = −1.35531 kPa/volt

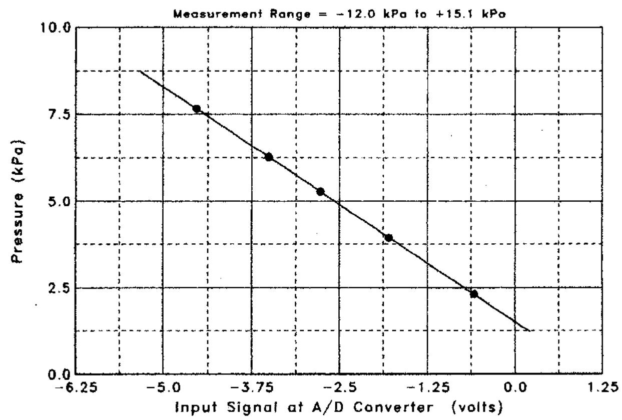

Fig. 4.13. Calibration diagram for one of the pressure transducers.

4.2.5 Acoustic Doppler Velocimeters (ADV)

An Acoustic Doppler Velocimeter (ADV) is capable of measuring flow velocity components (streamwise, transverse and vertical) at single points. The main advantage of ADVs is that they can sometimes, under certain conditions, provide non-intrusive flow measurements with high precision and high resolution. A 10MHz Nortek Vectrino + ADV was used in this experimental program, and consisted of three elements: the probe, the signal conditioning module and the processor. The probe is attached to the conditioning module, which contains low-noise receiver electronics encased in a submersible housing along with the processor. The probe consists of an acoustic transmitter and four acoustic receivers. Reflections of an acoustic pulse emitted by the transmitter from particles moving with the flow are received by the acoustic receivers. The Doppler effect (the change in frequency and wavelength of a wave as perceived by an observer moving relative to the source of the waves) is used to obtain the velocity based on the measured Doppler shift in frequency of reflections along the beam of each receiver in a small sampling volume, located at a fixed distance (5 cm) from the tip of the probe, Fig. 4.14 (a). The output from the processor was sent to a computer using a serial communication. Vectrino software was used to process and analyze the measured data. Further details can be found in the Nortek User Guide (2007).

The range of measured velocity was adjustable from ±1 to +400 cm/s, and a range of 200 cm/s was used in these experiments, with a sampling rate of 200 Hz. Measured velocities are accurate within ±0.5% of measured value ±1 mm/s. It should be noted that the fourth receiver is a new feature of this ADV that improves turbulence measurements and provides redundancy. In order to mount the ADVs in the flume, aluminum channels were specifically constructed in order to encase the ADVs. Steel clamps were used to rigidly fasten the ADV to the channel as shown in Fig. 4.14 (b). These channels could be attached to the vertical pipes and therefore positioned at any location and height in the flume.

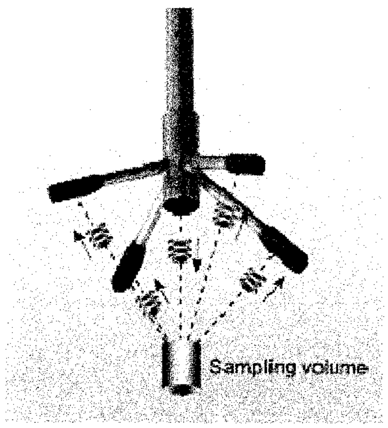

(a)

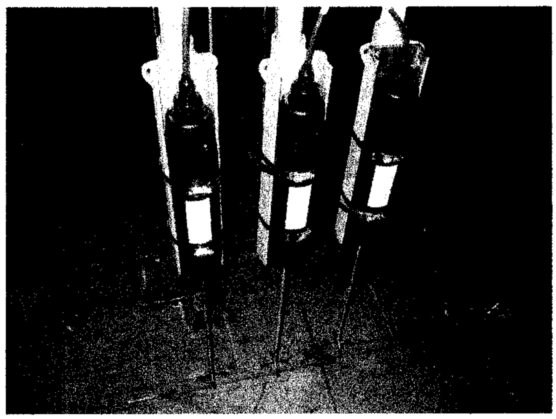

(b)

Fig. 4.14. (a) The four ADV receivers; illustration of the location of the sampling volume , Nortek User Guide (2007); (b) installation of the ADVs in the flume.

4.2.6 Data Acquisition system

Analog voltage signals from the different sensors deployed in the experiments were converted to digital format and saved into data files using a data acquisition system. All data were properly referenced to each other in time. NDAC data acquisition software developed by NRC-CHC was used in this study (Miles 2001). Signals from the transducers were routed through an interface unit to a data acquisition card (National

Instruments Inc. model 6031E) inserted into a PC. The card featured up to 32 channels of differential input, 16-bit resolution, and a maximum sampling rate of 1×10^{5} samples/sec.

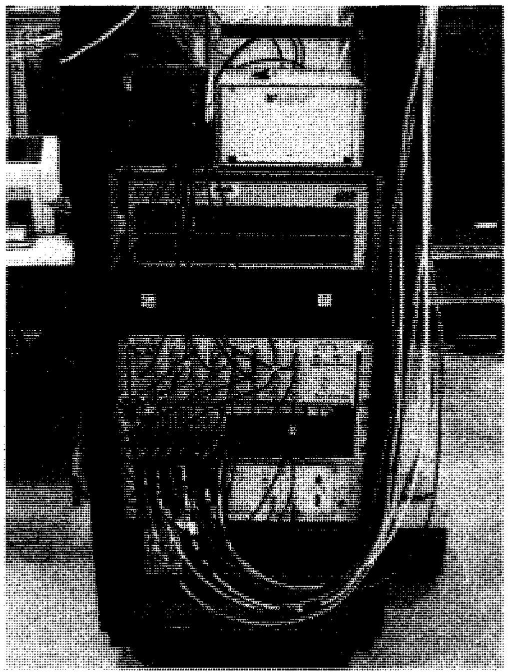

Fig. 4.15. Data acquisition system.

4.3. Test Structures

Two structures with circular and square cross sections were used in the experimental program in order to investigate the impact of hydraulic bore and water borne debris. Hereafter, the structures will be referred to as *circular* and *square*. In addition, the square structure was used in two configurations: (1) its side parallel to the flume; and (2) rotated at 45 degrees (hereafter referred to as the *diamond* structure). A description of the structures and their characteristics is presented in the next sections.

4.3.1 Circular Structure

A polyvinyl chloride (PVC) tube, referred to as the *circular* structure, with an outer diameter of 0.320 m, thickness of 9 mm and height of 0.7 m was used in the experiments. The circular structure had to be connected to the upper surface of the dynamometer, which has a height of 0.08 m. Had the structure been mounted on the dynamometer at its base, the bottom of the structure would have been located 0.08 m above the flume, and the impact of bores up to that height would have not been captured. Therefore, the diameter of the circular structure was selected such that it could enclose the dynamometer. A steel mount was constructed and bolted to the top of the dynamometer, as shown in Fig. 4.16. Then, the circular structure was connected to the steel mount with screws.

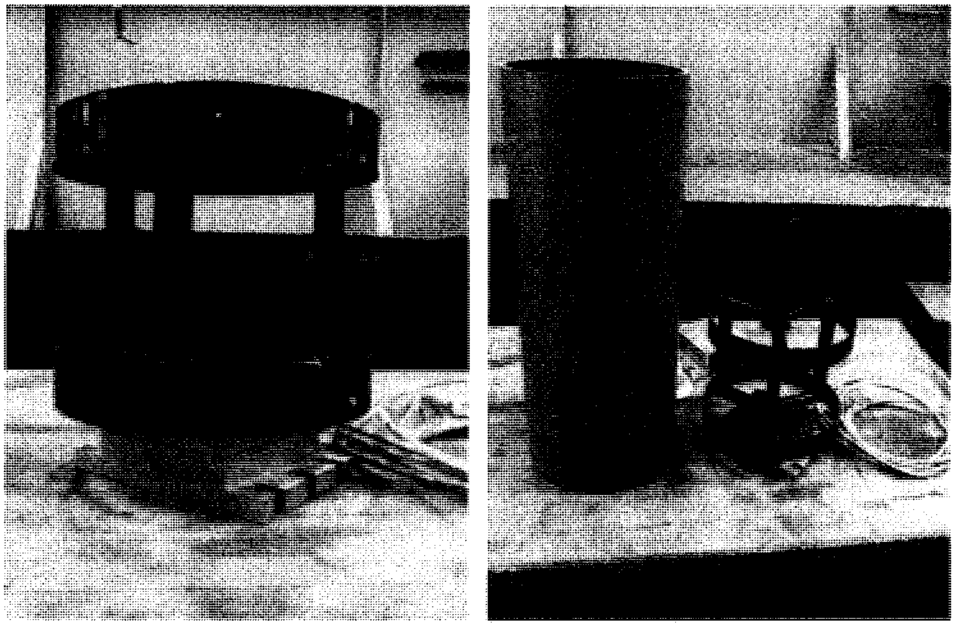

(a) (b)

Fig. 4.16. The circular structure: (a) the steel mount bolted to the dynamometer; (b) the circular structure beside the steel mount.

The arrangement of connections was such that the bottom of the circular structure was located 0.5 cm above the flume (i.e., a 0.5 cm wide gap existed between the structure's base and the flume). In order to prevent water seeping through the gap, silicone glue was used to fill it in and render the perimeter of the structure's base impermeable. Then, the silicone glue was cut around the perimeter so that the structure was not attached to the flume and could move due to exerted hydrodynamic forces.

Mounting the pressure transducers on the circular structure

Holes of 5 mm diameter were drilled at distances of 5 cm from each other along the height and on the upstream face of the circular structure, starting at 5 cm above the bottom of the flume. Pressure transducers were attached to the structure from the inside using silicone caulk, and were identified as P5, P10, P20, P25, P35, P40, P45, P50 and P55 (starting from bottom), as shown in Fig. 4.17. Flexible tubes, connected to the pressure transducers at one end and filled with green water, were placed such that their other end was flush with the outer surface of the structure. In order to verify the measurements of the transducers, the flume was gradually filled with water up to 0.7 m while the sensors recorded the exerted pressure on the structure as shown in Fig. 4.18a. Figure 4.18b shows the water level in the flume measured by five capacitance wave gauges (WG1, WG3, WG5, WG6, WG7) as the flume was filled up. It should be noted WG3 was not properly installed for this run, which caused the difference in recordings of the WG3 and other wave gauges in Fig. 4.18.

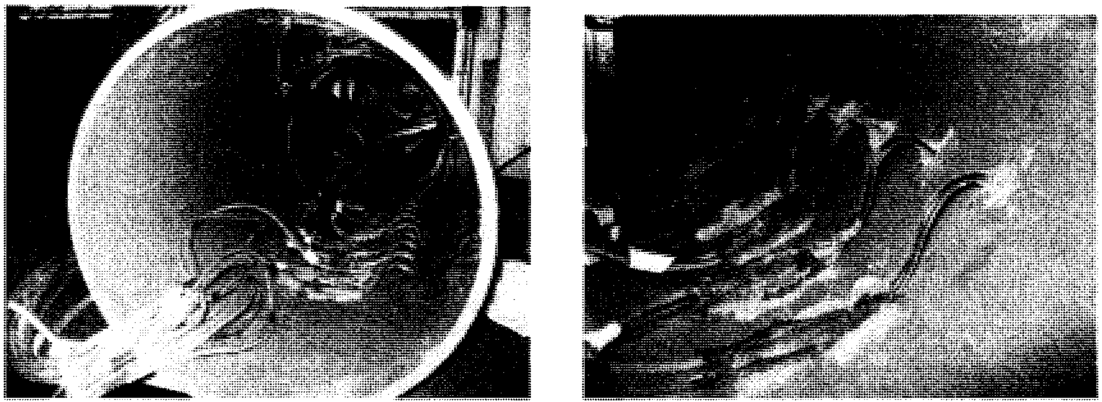

(a) (b)

Fig. 4.17. The circular structure: (a) the steel mount was bolted to the dynamometer; (b) pressure transducers mounted inside the circular structure.

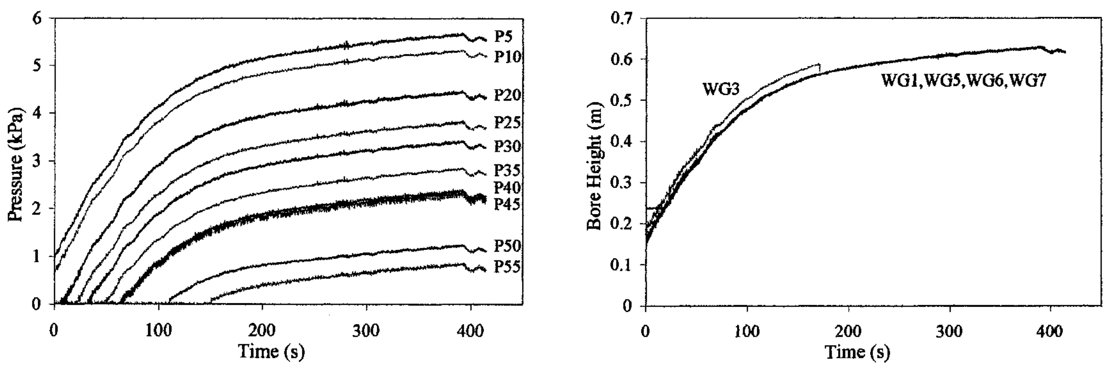

(a) (b)

Fig. 4.18. (a) Pressures and (b) water level measured simultaneously.

After mounting the circular structure, a reference load cell was used to validate the measurements of the dynamometer. Static loads were applied to the structure by pushing the structure in three directions and at different heights, using the reference load cell. The exerted forces and moments were measured by the dynamometer while the load cell also recorded the forces at the same time. Fig. 4.19 shows a comparison of the forces measured by the dynamometer and the reference load cell. The observed agreement between the collected data verifies the validity of the dynamometer measurements.

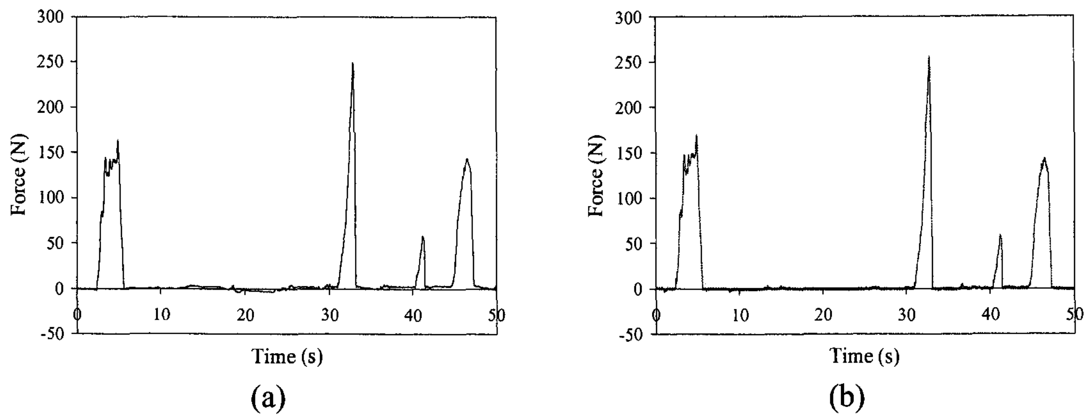

Fig. 4.19. Simultaneous comparison of forces measured by the: (a) dynamometer; and (b) a reference load cell.

Natural Frequency of the Structure

The dynamic response of a structure can affect the measured forces at the base in terms of magnitude and therefore, the time-history of exerted force. The forces measured by the dynamometer at the base of the circular structure may not be equal to the hydrodynamic force exerted on the structure. Therefore, the natural period of the circular structure had to be calculated in order to account for the dynamic response of the structure. Further explanation is provided in Chapter 5 and 6. The dynamic response of the circular structure was determined by subjecting the structure to a sudden *tap* and plotting the Fourier transform of the response. This revealed a dominant mode at 20 Hz in air and 13.5 Hz when submerged. Fig. 4.20 shows the Fourier transform of the structure in air and water.

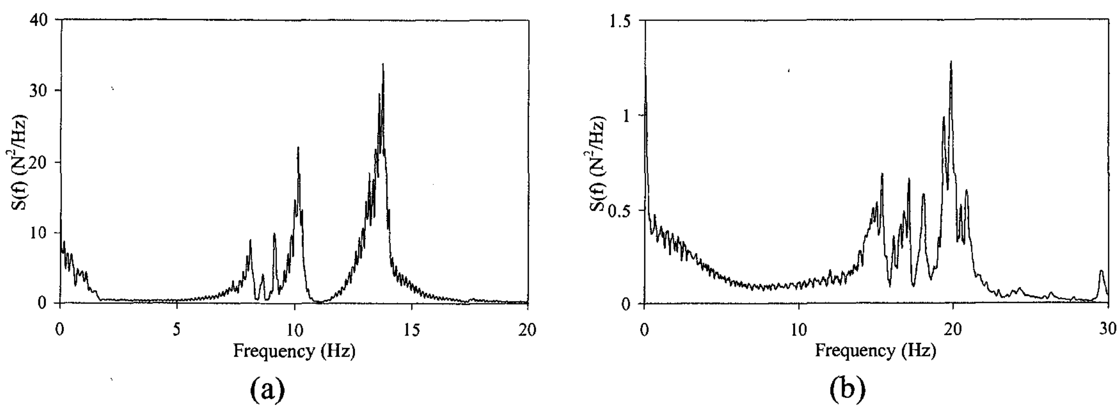

Fig. 4.20. The Fourier transform of the circular structure's response: (a) in water; and (b) in air.

4.3.2 Square Structure

A 0.2×0.2×0.6 m hollow column with a square cross section was constructed of acrylic Plexiglas. Plexiglas sheets were used for the sides and the base and were glued together using silicone glue. One hole with a diameter of 0.056 m was cut in each sheet except for the front sheet that had two holes, as shown in Fig. 4.21. Load cells were mounted on the column (through these holes) such that the load bearing plate was perfectly flush with the wall of the structure. The load cells were firmly attached to the structure with four No. 8 screws. Two load cells were installed on one side to account for runup, since the water level reached higher levels on the front face compared to the other three sides. The load cells mounted on the front are called LC3 (bottom) and LC5 (top). The load cells on the lateral sides are called LC4 (left) and LC6 (right) while the load cell mounted on the downstream face is called LC8.

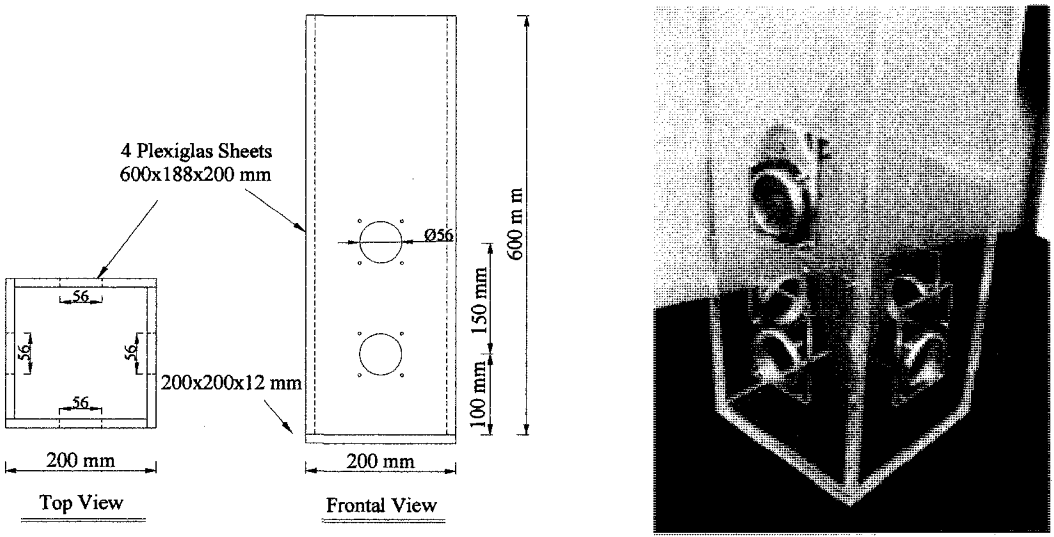

(a) (b)

Fig. 4.21. The square structure and location of load cells.

The structure was fixed to the bottom of the flume using silicone adhesive, and was made stable by adding up on top 80 kg of weight. As a safety precaution, the square structure was also partially restrained by a pair of steel pipes suspended from above. All of these measures can be seen in Fig. 4.22 and Fig. 4.23, which show the square structure installed in the flume, ready for testing.

At first, water was able to seep into the structure through small gaps around the load cell mounting plates. Later, these gaps were sealed with caulking in order to eliminate water intrusion.

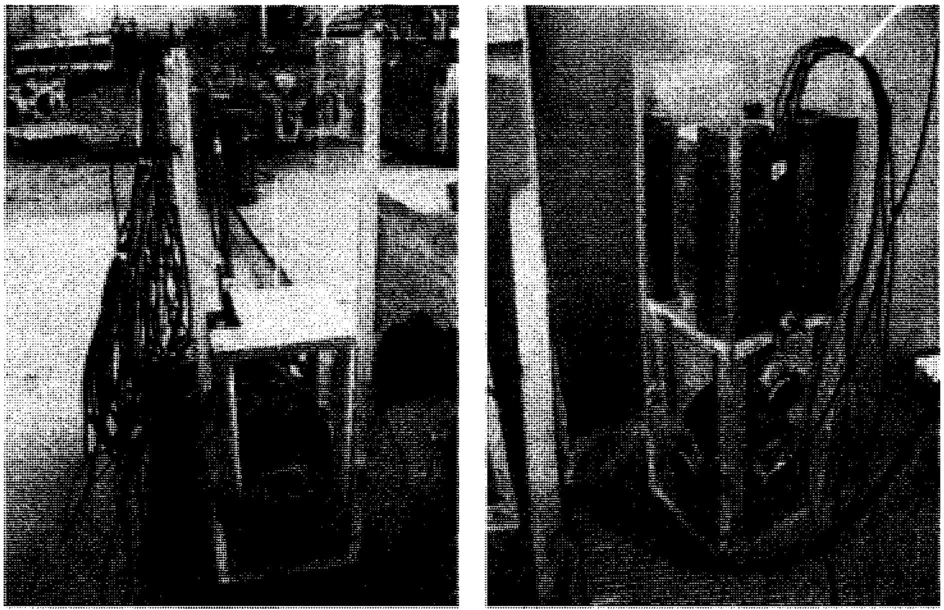

Fig. 4.22. Wooden frame for bearing the weights: a) frame and column, b) frame mounted inside the column.

Fig. 4.23. Pipes installed inside the column.

After mounting the load cells on the structure, a reference load cell was used to validate the measurements of the sensors. Static time-varying loads were applied to the load cells by pushing on the centre of the load bearing plate using the reference load cell as shown in Fig. 4.24. The exerted forces were measured by the load cells and the reference load cell simultaneously. Fig. 4.25 shows a comparison of the forces measured by the load cells mounted on the square structure and the reference load cell. The observed agreement between the collected data confirms the validity of the measurements.

Fig. 4.24. Testing the accuracy of load cells mounted on the structure using a reference load cell.

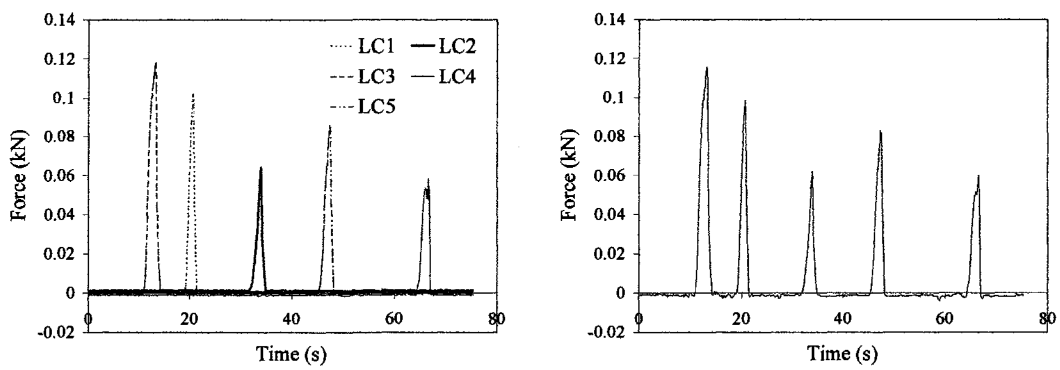

Fig. 4.25. Simultaneous comparison of the forces measured by the load cells (left) and a reference load cell (right).

4.4. Upstream Obstacles

In order to study the effect of upstream obstacles on the forces and pressures exerted due to bores, two types of upstream obstacles were selected: (1) constrictions, and (2) a second structure similar to the main one. However, the effect of the latter was only studied for the case of a circular structure and details are given in the following sections.

4.4.1 Constrictions

Since wooden logs could not be easily attached to the sides of the steel flume, two C sections were welded to each side of the flume at a distance $x = +1.50$ m (x is defined in Fig. 4.2). Then, the first wooden log was screwed to the sections while the next logs were screwed to the first log in order to create the constrictions shown in Fig. 4.26 and Fig. 4.27. Up to seven logs, each with a rectangular cross-section of 3.81×17.78 cm and a length of 60 and 80 cm were used on each side. The same number of logs was used on each side to ensure symmetrical constrictions in all tests. Logs could be easily attached or removed and tests were performed using different constriction widths.

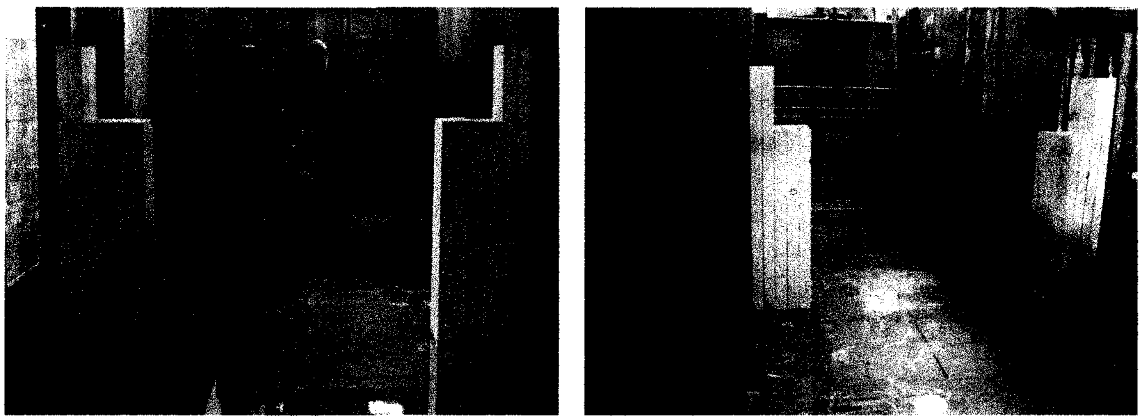

Fig. 4.26. Wooden logs installed as constrictions, upstream of the structure: (a) upstream view; (b) downstream view.

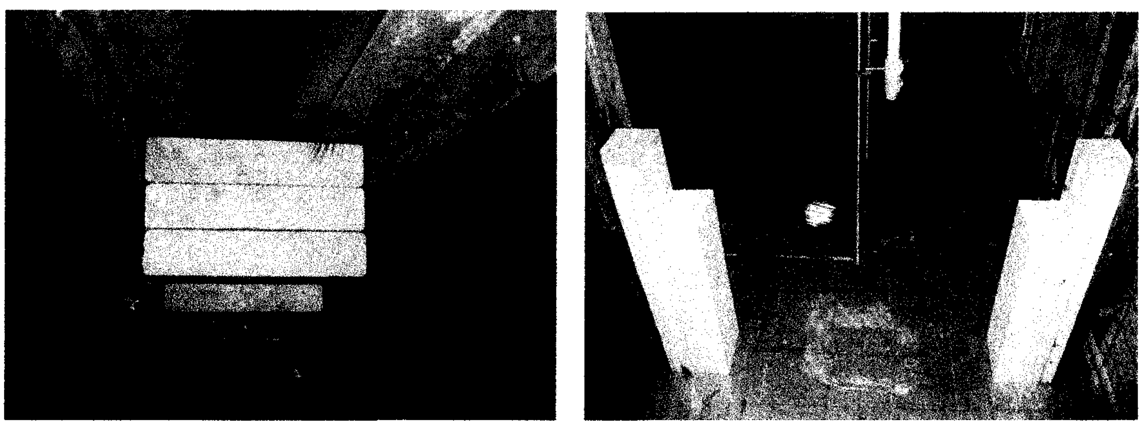

Fig. 4.27. Different constriction widths were tested using different number of logs: (a) four; (b) six.

In order to represent the constriction width in a dimensionless form, the Blockage Ratio was defined as shown in Eq. 4.1.

$$BlockageRatio = \frac{CW_1 + CW_2}{W} \tag{4.1}$$

where CW_1 and CW_2 are the width of the constriction on the left and right side, respectively, and W is the total flume width.

4.4.2 Cylinder

A second cylinder similar to the circular structure and having the same diameter (0.32 m) was used as an upstream obstacle to the flow as shown in Fig. 4.28. Weights were used to hold the cylinder in place as shown in Fig. 4.28 (a). Also, as a precaution, a vertical bar attached to the top frame was located in the cylinder, without contact with the inner surface. The distance between the bar and the cylinder was verified after each test, in order to make sure that the cylinder had not moved downstream. The centre-to-centre distance between the second cylinder and the circular structure was selected as $2d$, $3d$ and $4d$, where $d = 0.32$ m is the outer diameter of the circular structure.

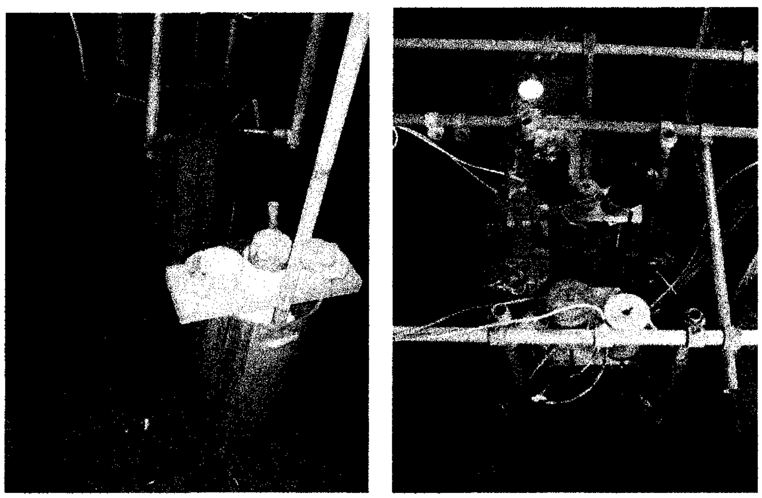

(a) (b)

Fig. 4.28. The cylindrical upstream obstacle.

4.5. Debris Impact Loading

Two rectangular wooden logs, hereafter referred to as the *small* and *large* logs, were used to study the debris impact force. The small log was 0.435 m long, with a rectangular cross-section of 0.06×0.045 m and a mass of 0.474 kg. The large log was 0.443 m long, with a square cross section of 0.09×0.09 m, and a mass of 1.479 kg. The logs were initially placed at the centreline and on the bottom of the flume at a distance, x = 1.75 m, with their long side parallel to the flume side. Two cotton strings were attached to each side of the log and the pipe frame in order to prevent the log from being washed away after the impact (Fig. 4.29). However, the length of the strings was carefully adjusted such that they remained slack at impact, therefore the strings did not affect the impact force. The generated dam-break waves carried the logs to the point of impact on the circular structure. Video recordings were taken to capture the impact orientation. Two still frames from the video are shown in Fig. 4.30.

Fig. 4.29. Strings attached to the sides of the log.

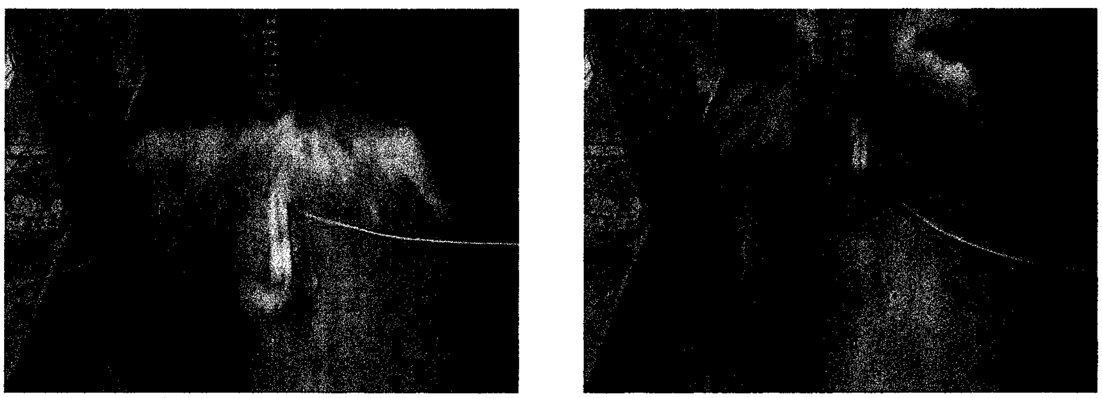

Fig. 4.30. The log is carried by the hydraulic bore and impacts the circular structure.

4.6. Experiments

The experiments performed were divided into ten different test series in order to study forces and pressures on the structures due to bore impact, considering the effect of various parameters, such as upstream obstacles and debris impact. Various configurations for the structures and the measurement devices were used and are described in the following sections. Table 4.1 provides a brief description of the conducted tests, where test series were performed with varying impoundment depths. In this table, PT denotes pressure transducers, DYN denotes the dynamometer, WG denotes wave gauges, LC denotes load cells and x is defined in Fig. 4.2. It should be noted that for all tests, one or two repetitions were performed in order to verify and assess the repeatability of results.

Table 4.1. Summary of test program.

Test Series No.	**Structure**	**Structure Location (m)**	**Measurement Devices**	**Debris Weight (kg)**	**Impoundment Depth (m)**	**Upstream Obastacles**
1	N/A	N/A	ADV,WG	N/A	0.50,0.75,0.85	N/A
2	N/A	N/A	WG	N/A	0.50,0.75,0.85	Constrictions
3	Cylindrical	$x = 0$	PT,DYN,WG	N/A	0.50,0.75,0.85,1.00	N/A
4	Cylindrical	$x = 0$	PT,WG	N/A	0.75,1.00	N/A
5	Cylindrical	$x = 0$	DYN,WG	0.474-1.479	0.75,1.00	N/A
6	Cylindrical	$x = 0$	DYN,WG	N/A	0.50,0.75,0.85	Cylinder
7	Cylindrical	$x = 0$	DYN,WG	N/A	0.50,0.75,0.85	Constrictions
8	Square	$x = 0$	LC,WG	N/A	0.50,0.75,0.85	N/A
9	Square	$x = 0$	LC,WG	N/A	0.50,0.75,0.85	Constrictions
10	Square	$x = +1.50$	LC,WG	N/A	0.50,0.75,0.85	N/A
11	Diamond	$x = 0$	LC,WG	N/A	0.50,0.75,0.85	Constrictions

4.6.1 Test Series 1

This series of tests was performed in order to investigate bore front velocities along the flume, without the structure. Tests were carried out with various impoundment depths. Bore heights were measured using six wave gauges that were arranged in two rows, located 0.6 m apart, as shown in Fig. 4.31. Tests were repeated with the instrument array located at three stations along the flume, as shown in Fig. 4.31. It should be noted that all gauges locations were tested for all impoundment depths.

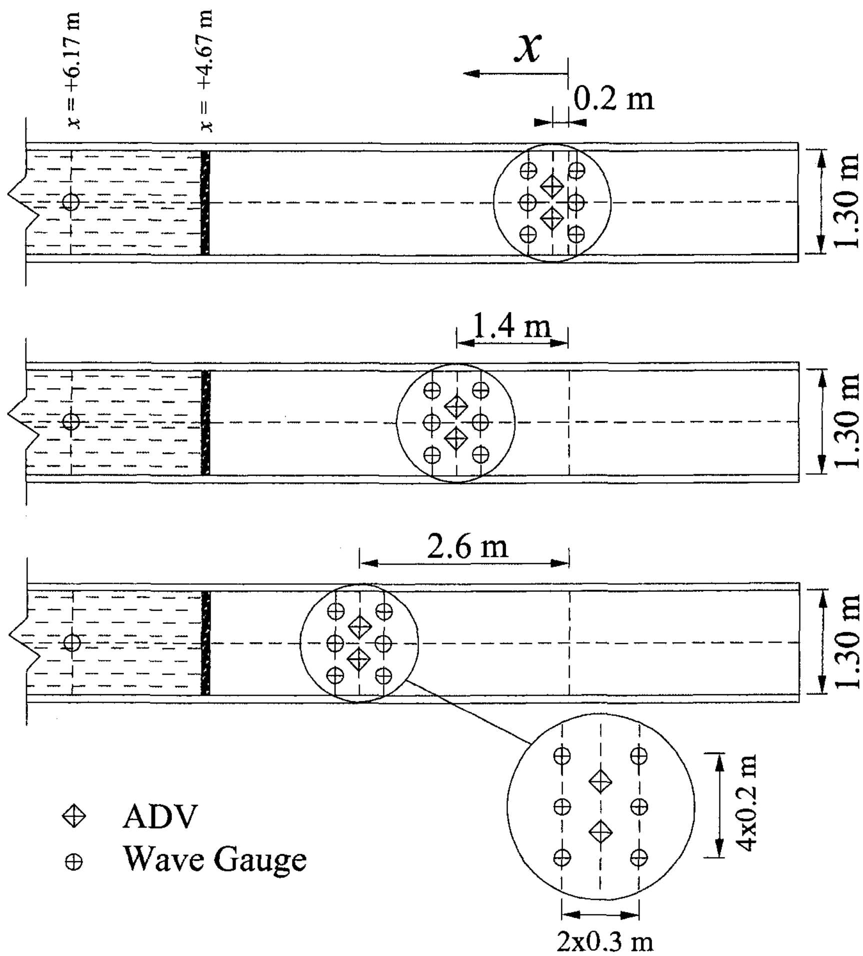

Fig. 4.31. Layout of measurement devices used in Test Series 1.

4.6.2 Test Series 2

This series of tests was performed in order to investigate bore front velocities after constrictions were installed and without the structures. The tests were carried out with various impoundment depths. Bore heights were measured using four wave gauges arranged in two rows located 0.3 m apart, as shown in Fig. 4.32.

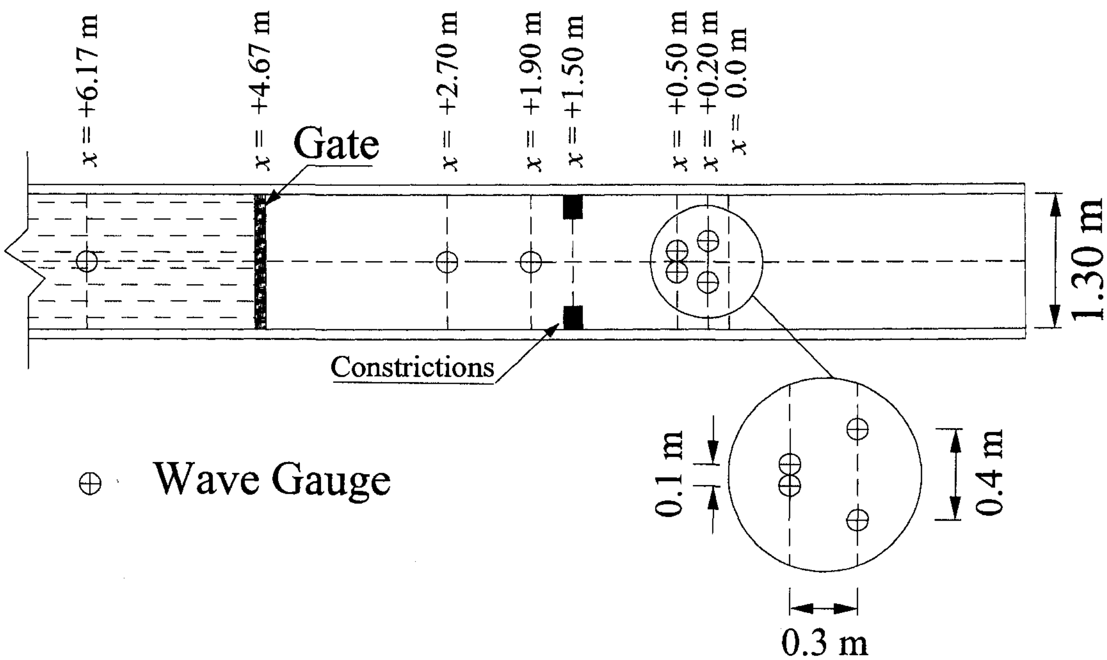

Fig. 4.32. Layout of measurement devices used in Test Series 2.

4.6.3 Test Series 3

In this test series, the circular structure was located at x = 0.0, without any upstream obstacles. Hydraulic bores were generated using impoundment depths of 0.5, 0.75, 0.85 and 1.00 m. Global forces and moments due to bore impact were measured using the dynamometer, while pressure transducers recorded the pressures exerted on the upstream face of the structure. Wave gauges were located as shown in Fig. 4.33.

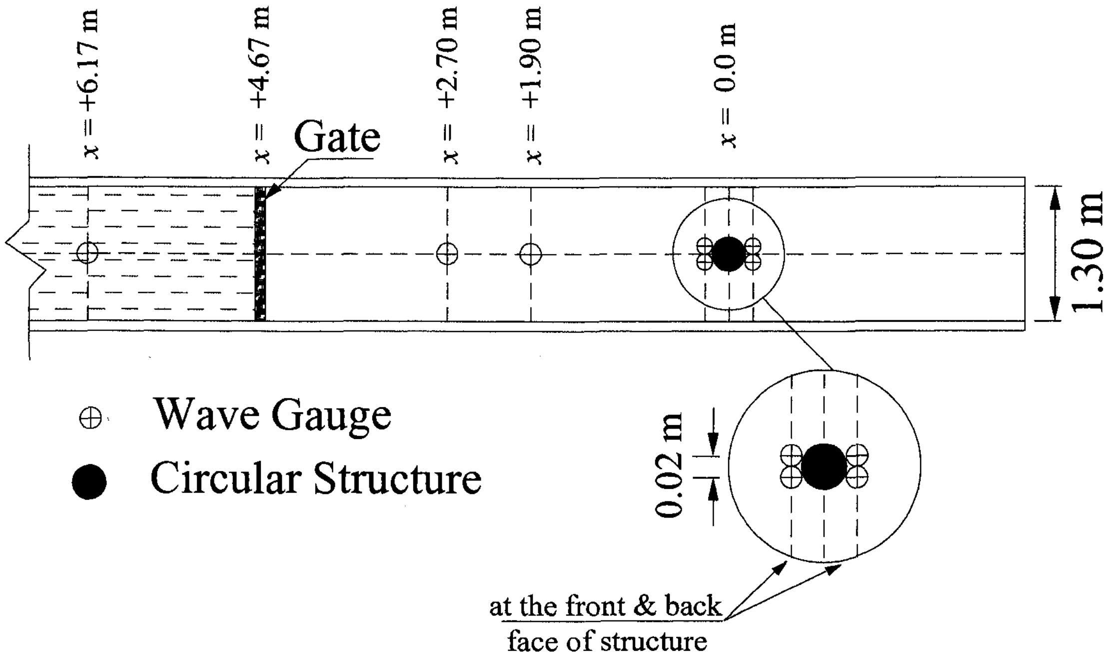

Fig. 4.33. Layout of measurement devices used in Test Series 3 and 4.

4.6.4 Test Series 4

Test series 4 was exactly the same as test series 3, except that the circular structure was rotated at 90, 180 and 270 degrees with respect to the initial position of the structure, in order to measure the pressures on sides and downstream face of the structure. The tests were performed using impoundment depths of 0.75 and 1.0 m.

4.6.5 Test Series 5

For test series 5, the circular structure was located at x = 0.0, without any upstream obstacles. Hydraulic bores (using impoundment depths of 0.75 and 1.00 m) picked up wooden logs, as described in Section 4.5. Forces and moments due to both the bore and debris impact were measured using the dynamometer. Only one wave gauge was used in order to measure the water level upstream of the gate, as shown in Fig. 4.34.

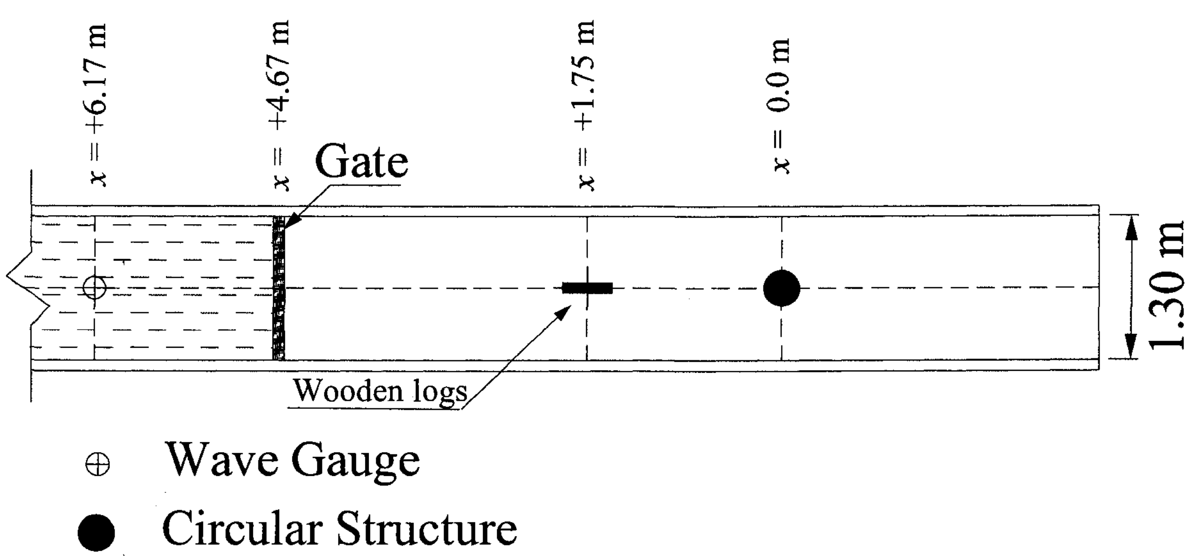

Fig. 4.34. Layout of measurement devices used in Test Series 5.

4.6.6 Test Series 6

In test series 6, the circular structure was located at x = 0.0, while a single cylindrical obstacle was located upstream at distances of 2*d*, 3*d* and 4*d* where *d* is the cylinder diameter, as previously explained in Sec. 4.4.2. Hydraulic bores were generated using impoundment depths of 0.5, 0.75 and 0.85 m. Exerted forces and moments due to bore impact were measured using the dynamometer. The layout for this test series is shown in Fig. 4.35.

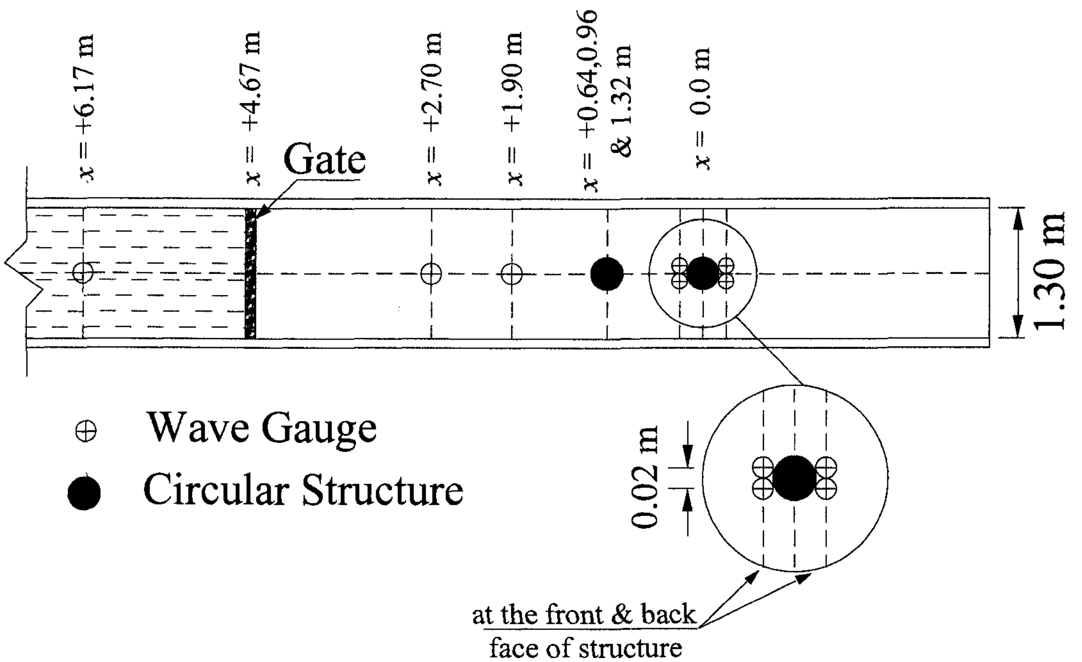

Fig. 4.35. Layout of measurement devices used in Test Series 6.

4.6.7 Test series 7

In test series 7, the circular structure was located at x = 0.0, with constrictions as upstream obstacles, as explained in Section 4.4.1. Hydraulic bores were generated using impoundment depths of 0.5, 0.75 and 0.85 m. Exerted forces and moments due to bore impact were measured using the dynamometer. The layout for this test series is shown in Fig. 4.36.

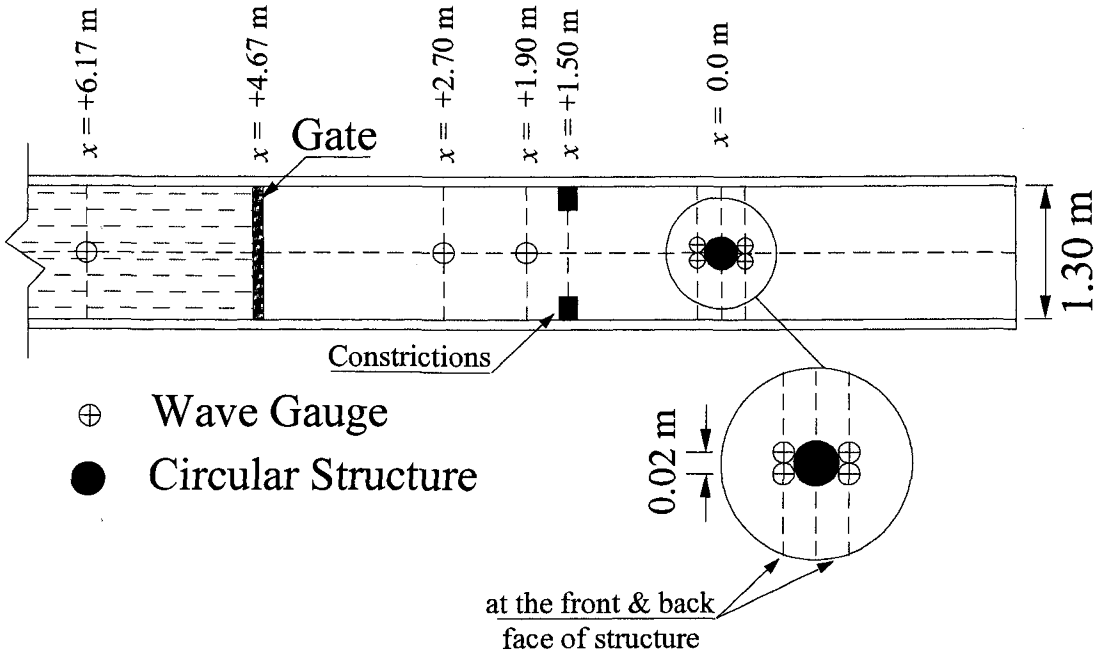

Fig. 4.36. Layout of measurement devices used in Test Series 7.

4.6.8 Test series 8

In test series 8, the square structure was located at x = 0.0, without upstream obstacles. Hydraulic bores were generated using impoundment depths of 0.5, 0.75 and 0.85 m. Exerted forces due to bore impact on all four sides of the structure were measured at single points using the load cells. The layout for this test series is shown in Fig. 4.37.

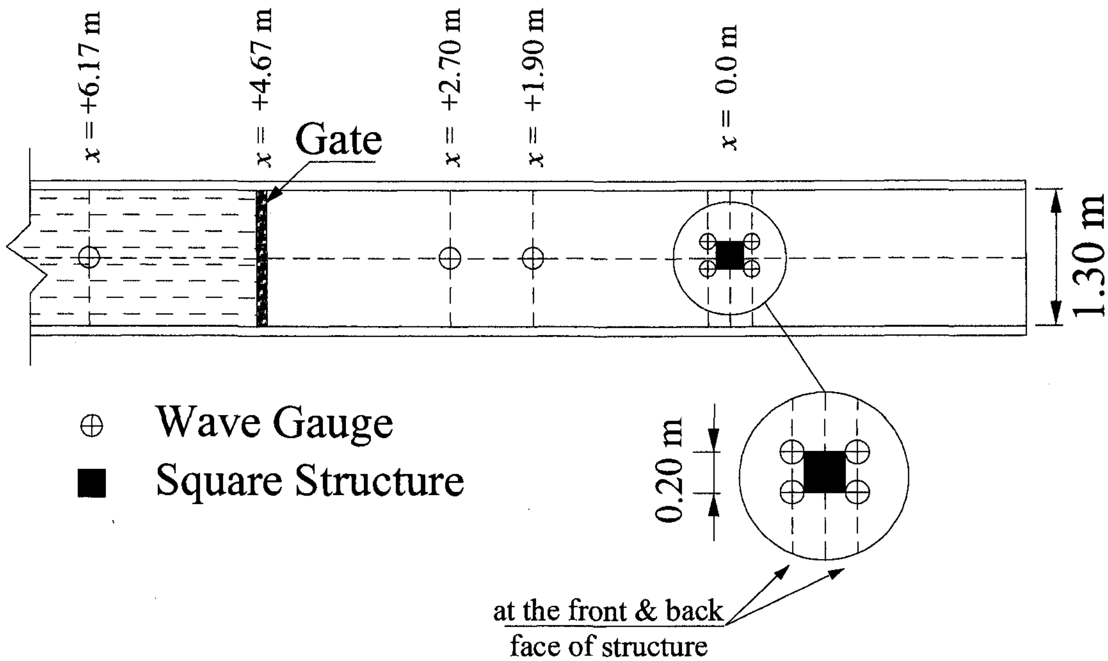

Fig. 4.37. Layout of measurement devices used in Test Series 8.

4.6.9 Test series 9

In test series 9, the square structure was located at x = 0.0, with constrictions to the flow upstream of the structure, as explained in Section 4.4.1. Hydraulic bores were generated using impoundment depths of 0.5, 0.75 and 0.85 m. Exerted forces due to bore impact on all four sides of the structure were measured at single points using the load cells. The layout for this test series is shown in Fig. 4.38.

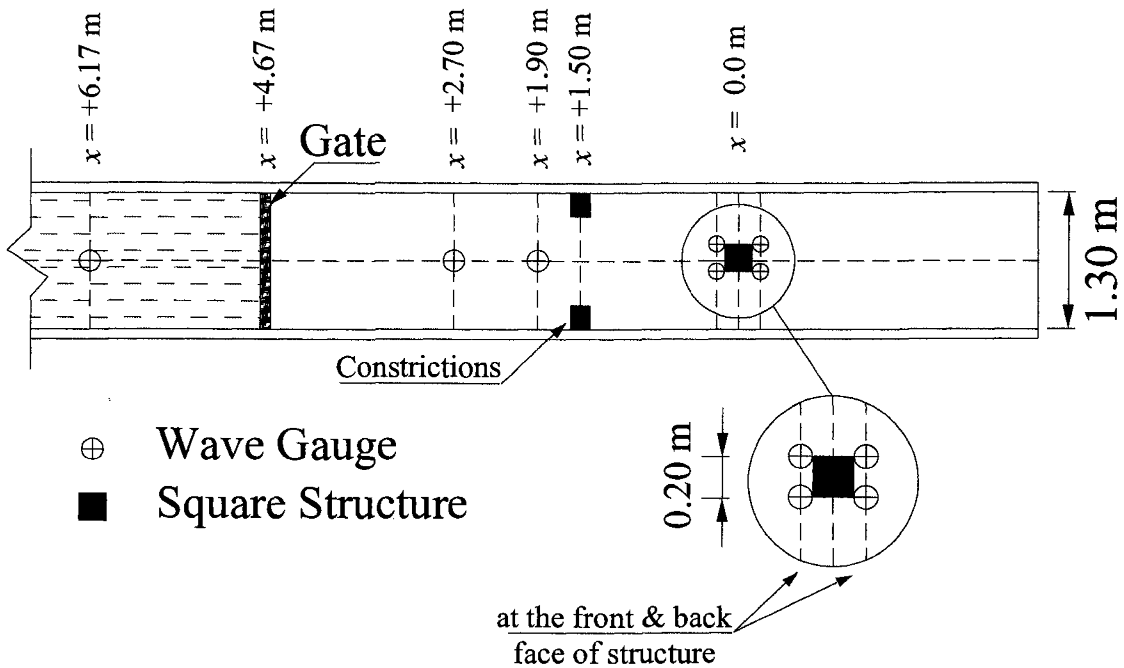

Fig. 4.38. Layout of measurement devices used in Test Series 9.

4.6.10 Test series 10

In test series 10, the square structure was located at $x = +1.50$ m, without any upstream obstacles. Hydraulic bores were generated using impoundment depths of 0.5, 0.75 and 0.85 m. Exerted forces due to bore impact on all sides of the structure were measured at single points using the load cells. The layout for this test series is shown in Fig. 4.39.

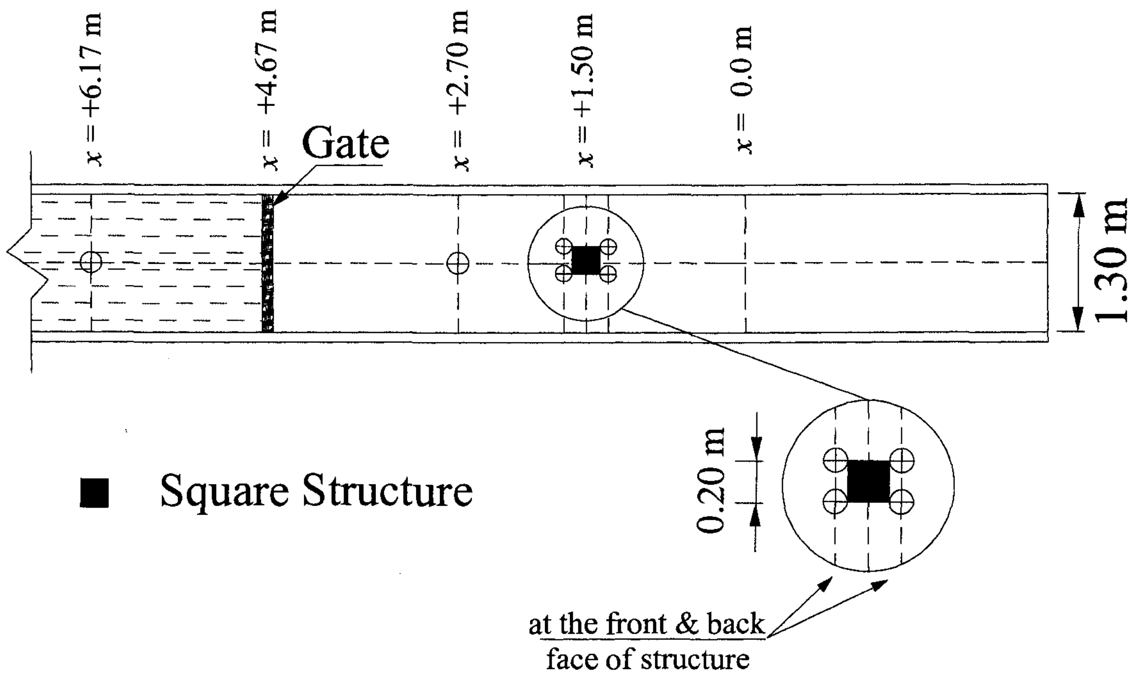

Fig. 4.39. Layout of measurement devices used in Test Series 10.

4.6.11 Test series 11

In test series 11, the diamond structure was located at x = 0.0, with constrictions to the flow upstream of the structure, as explained in Section 4.4.1. Hydraulic bores were generated using impoundment depths of 0.5, 0.75 and 0.85 m. Exerted forces due to bore impact on all sides of the structure were measured at single points using the load cells. The layout for this test series is shown in Fig. 4.40.

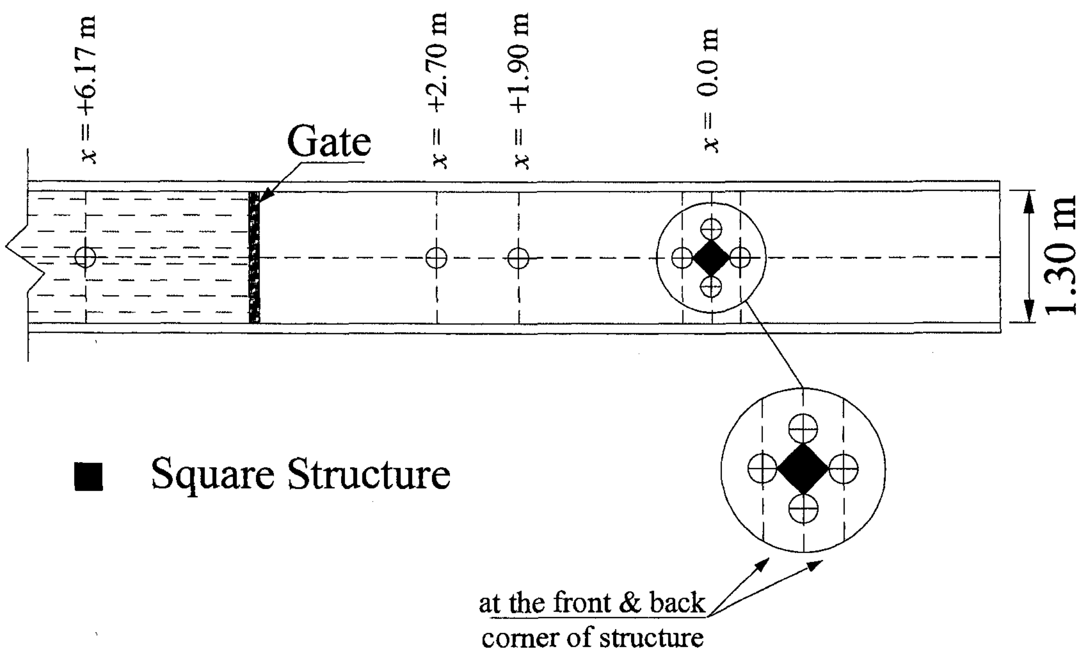

Fig. 4.40. Layout of measurement devices used in Test Series 11.

Chapter 5. Results and Discussion

5.1. Data Processing

5.1.1 FFT-Based Bandpass Filtering

The program FILT-FFT, from the GEDAP suite of analysis software developed and used at CHC-NRC, was used to help process the raw data collected during these tests. FILT-FFT applies a rectangular bandpass filter to a time series signal. This filter removes all energy in the signal that occurs at frequencies below F1 Hz and at frequencies above F2 Hz where the frequencies F1 and F2 are specified by the user. The Fourier transform of the input signal is computed by FFT and the rectangular bandpass filter is applied in the frequency domain. An inverse FFT is then used to obtain the filtered output signal.

The input signal may contain any number of points. This filter is also able to perform cubic spline interpolation to re-sample the signal to a larger number of points for compatibility with FFT operations. Consequently, the output signal computed by this filter may have a smaller time step than the input signal but both signals are defined over the same period of time. The mean value of the input signal is removed prior to applying the filter. The original mean value can also be added to the filtered output signal as an option. FILT_FFT does not remove any trends other than the mean value.

It should be noted that the output record is defined over the same time interval as the input record. However, it may contain more data points and a smaller time step than the input signal. Data processing was only performed on data measured by the dynamometer and FILT_FFT was applied to the data with F1 = 0 Hz and F2 = 50 Hz in order to remove noise, except for the data presented in Section 5.5 where no data processing was performed.

5.2. Flow Analysis

5.2.1 Bore Characteristics

In the present experimental program, wave-front velocities were measured using six wave gauges that were arranged in two rows, separated by either 0.6 m (Test Series 1) or 0.3 m (Test Series 2). The wave front velocity was calculated from the averaged measured time difference of the bore height reaching the same specific water depth (0.06 m) in both rows. Table 5.1 shows the measured data including the distance between the gate and the point where the velocity was calculated (x) (in the middle of the wave gauge rows), the time that it took the bore to reach that point after gate opening and bore-front velocity (U) as well as calculated non-dimensional space and time variables (X and T). Fig. 5.1 shows the measured values (points) along with a numerical model prediction (line) obtained by Leal *et al.* (2006) in non-dimensional (X, T) space (see Section 2.1.2). This figure shows that the measured velocities are in good agreement with previous studies. If the gate opening period is not short enough (shorter than the Lauber and Hager (1998) criterion, see Section 2.1.2), it would influence the free falling movement of the particles near the free surface, the formation of the dynamic wave, the wave-front propagation and consequently the exerted force on the structure. These results indicate that the gate opening period is short enough, such that it does not affect the bore characteristics significantly. Therefore, the bores generated in this study are typical dam-break flows.

Table 5.1. Calculated bore-front velocity and non-dimensional time and space variables.

h_0 (m)	x (m)	U (m/s)	t (s)	T	X
0.50	2.07	2.60	0.77	3.41	4.00
0.75	2.07	3.84	0.52	1.88	2.67
0.85	2.07	4.63	0.43	1.47	2.35
0.50	3.27	2.31	1.39	6.15	6.40
0.75	3.27	3.26	0.98	3.55	4.27
0.85	3.27	3.32	0.96	3.27	3.76
0.50	4.47	2.63	1.67	7.42	8.80
0.75	4.47	3.33	1.32	4.78	5.87
0.85	4.47	4.61	0.96	3.25	5.18

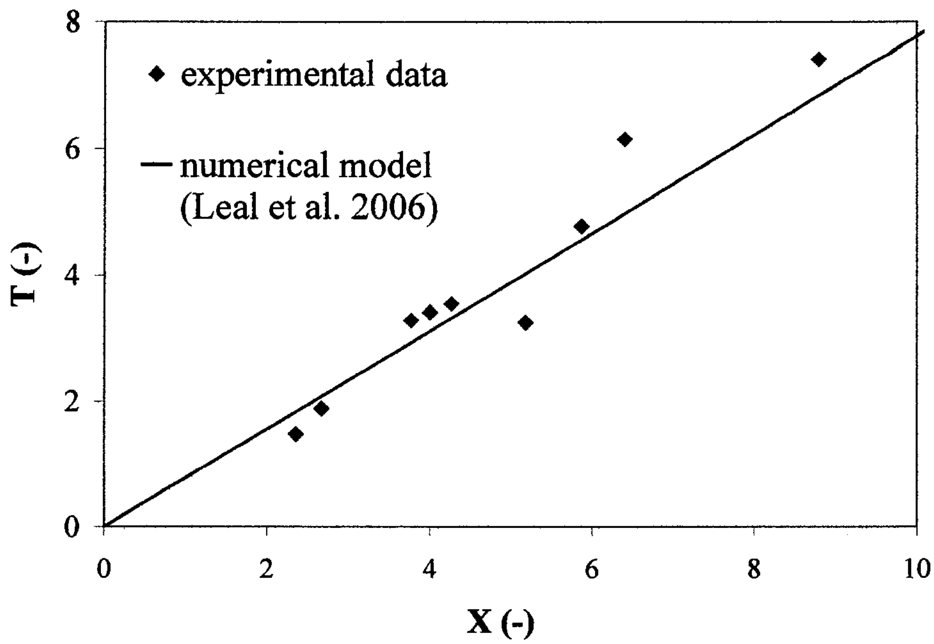

Fig. 5.1. Bore front velocities in non-dimensional space.

Acoustic Doppler Velocimeters (ADVs) were also used to measure the streamwise component of the velocity. As discussed in Sec 4.2.6, the reflection of acoustic pulses by particles in the water is essential for these instruments. Since there was no reflection before the bore passed the ADVs, bore front velocities were not captured. Also, cavitations were observed around the probe tips (Fig. 5.2), which prevented the instruments from functioning. For these reasons, reliable velocity measurements were only obtained in a small number of tests.


Fig. 5.2. Cavitations around the ADV probes.

5.2.2 Bore Profile

As discussed above, in Test Series 1, bore heights were measured at $x = +0.10$, -1.10 and -2.30 m using six wave gauges located in two rows in absence of the structures in order to calculate flow velocities. For example, the bore profile measured by the wave gauges in the first row and second row due to a hydraulic bore generated with impoundment depth of 0.5 m are shown in Fig. 5.3. The measured bore heights were compared using the least square method, and the relative difference of the obtained values from wave gauges in a row was found to be less than 10%. It was observed that largest differences existed at $x = +0.10$ where cross waves did not have a negligible effect. This effect was negligible further downstream of this point where the structure was located. Assuming a constant velocity for the bore front travelling between the first and second rows, the bore front slope was estimated by converting the obtained values for bore height from time space to location space. Bore front slopes of 1/10, 1/7.1 and 1/6.25 were calculated for bore heights generated with impoundment depths of h_0 = 0.5, 0.75 and 0.85 m respectively. Thus, larger impoundment depths generated bores with steeper fronts.

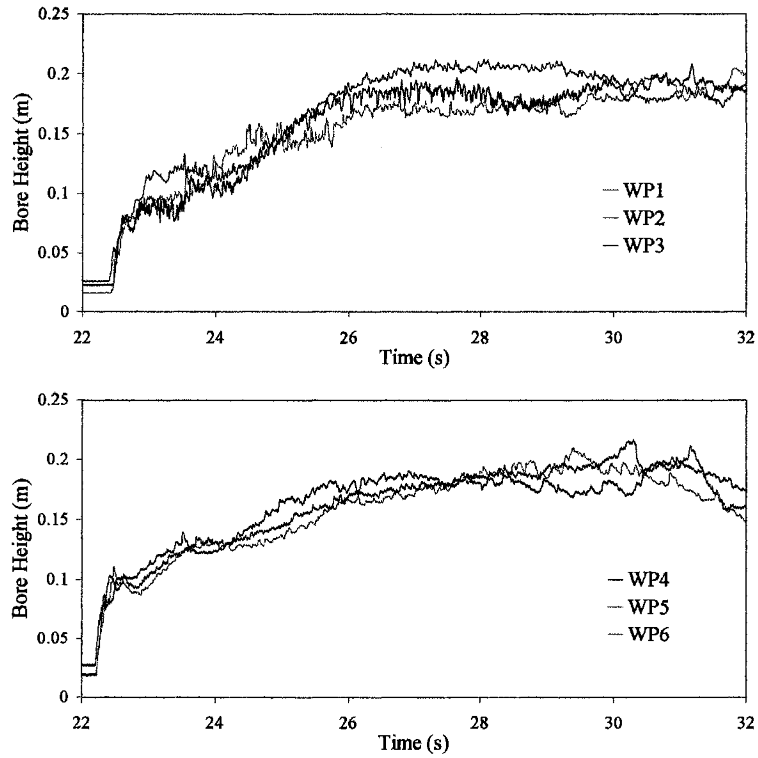

Fig. 5.3. Bore heights measured by wave gauges located in two rows due to a bore generated with impoundment depth of h_0 = 0.50 m.

5.3. Bore-Structure Interaction

5.3.1 Time History of Global Forces

The forces exerted on the circular structure, in the stream-wise, cross-stream and vertical directions as well as moments about these axes were measured by the dynamometer in Test Series 3, 5, 6 and 7. However, it should be noted that only measured forces in the stream-wise direction have been investigated throughout this study. Fig. 5.4 shows time histories of the horizontal force exerted in the stream wise direction due to bores generated with impoundment depths of h_0 = 0.5, 0.75, 0.85 and 1.00 m. An obvious distinction is observed between the time history of force for impoundment depth of h_0 = 1.00 m and other impoundment depths. This figure shows that impact of a bore front generated by impoundment depths of h_0 = 0.5, 0.75 and 0.85 exerts a relatively large force over a short period of time. This sudden rise is due to the first contact of the bore with the upstream face of the structure. After this rise, the force reduces to 60% of the peak value and then gradually increases to an approximately constant greater value. This value is due to a semi-steady state of the flow where the bore has surrounded the structure and is expected to be equal to the hydrodynamic (drag) force. However, for the hydraulic bore generated with an impoundment depth of 1.00 m, the first rise is almost equal to the force in the steady state. This is due to a higher slope of the bore front that leads to a bore with larger bore height impacting the structure.

The sudden rise in the measured time history of forces corresponds to a surge force as discussed in Chapter 3, whereas the force due to the passing bore corresponds to the hydrodynamic (drag) force. As stated earlier, the important unknown in design for tsunami-induced forces is the surge component and its value compared to the hydrodynamic force. It is observed that the initial rise due to the first impact does not overshoot the constant force due to a passing bore. This means that surge force is equal or less than the hydrodynamic force in these experiments. As mentioned earlier in Sec. 2.3 Ramsden (1993) observed that the exerted force on a wall highly depends on the slope of bore front. Also, Arnason (2005) observed that initial rises were less than the hydrodynamic force in the case of a circular structure.

Force rise times equal to 0.045, 0.049, 0.053 and 0.060 s were measured due to the impact of bores generated with impoundment depths of h_0 = 0.5, 0.75, 0.85 and 1.00 m, respectively. The force rise times are significantly larger compared to pressure rise times, as explained in the following section. It is observed that oscillations exist in the measured time history of the force prior to the bore impact. These oscillations were caused by vibration of the flume's bottom plate, which was not rigidly attached to underlying beams. As the bore impacts the structure and passes over the plate, these vibrations were attenuated and their effects became small.

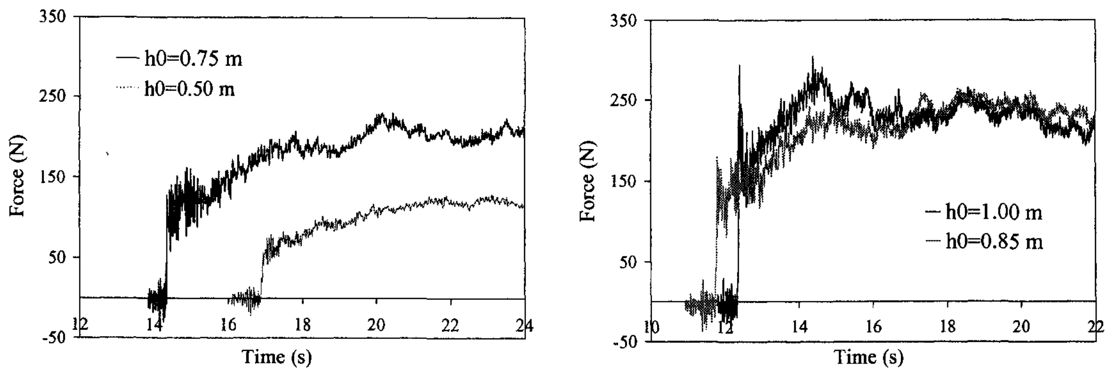

Fig. 5.4. Time history of stream-wise horizontal force exerted on the circular structure.

5.3.2 Time History of Local Forces

The local exerted force on all sides of the square structure was measured by the load cells in Test Series 8 and 10. The square structure was located at $x = \pm 0.0$ and $+1.50$ m in Test Series 8 and Test Series 10, respectively. Time histories of the exerted force due to bores generated with impoundment depths of h_0 = 0.5, 0.75 and 0.85 is presented in the following Sections.

Upstream Face

Figures 5.5 and 5.6 show time histories of the forces measured by the two load cells on the upstream face of the square structure when the structure was located at $x = +1.50$ and ± 0.0, respectively. As expected, it is observed that forces measured by the lower load cell (LC3) are approximately two times larger than the corresponding values measured by the upper load cell (LC5). The bore front directly impacts LC3 while forces exerted on LC5 are caused by bore runup. Furthermore, it is observed that forces measured by LC3 increase abruptly from zero to a peak value while this sudden rise is not observed in the time history of forces measured by LC5. Comparison of Figs. 5.5(a) with 5.6(a) shows that the structure location did not affect the magnitude and time history of exerted forces. However, comparison of Figs. 5.5(b) with 5.6(b) shows a slight reduction in the exerted forces when the structure is located further downstream of the gate. Also, forces exerted on LC5 (Fig. 5.6(b)) increase to a peak value over a shorter period, compared to corresponding forces in Fig. 5.5(b). This might be caused by bore height reduction along the flume.

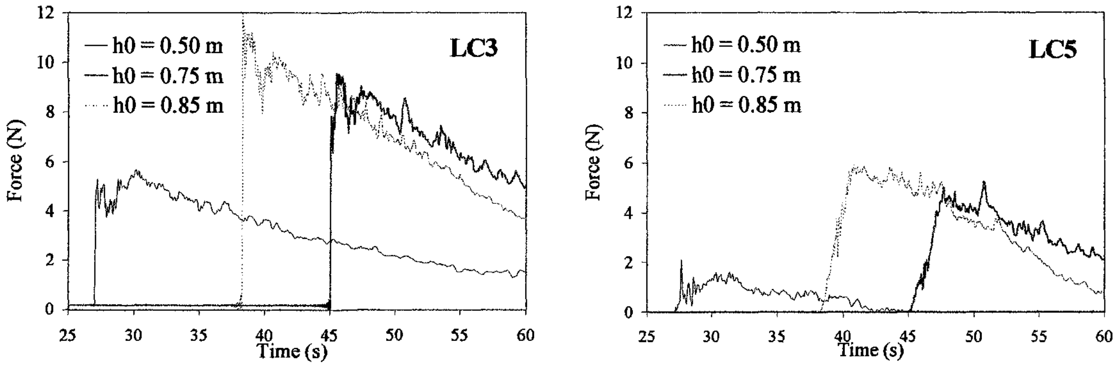

(a) (b)

Fig. 5.5. Time history of local force exerted on the upstream face of the square structure: (a) LC3; and (b) LC5 ($x = +1.50$).

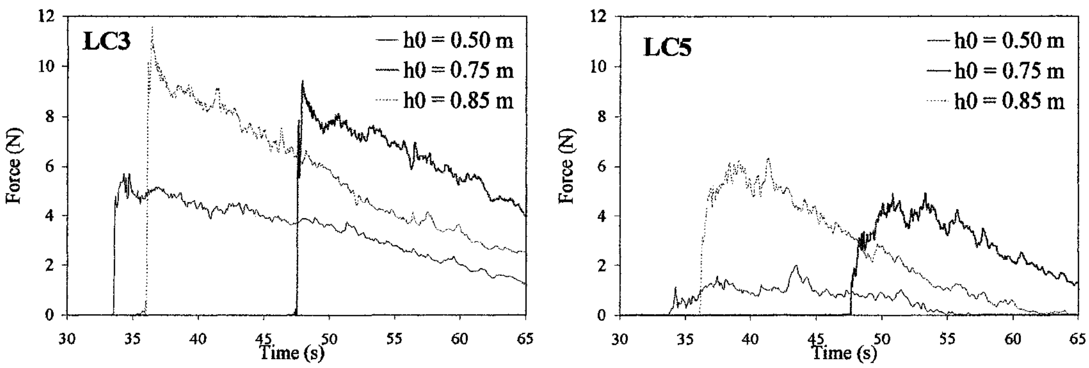

(a) (b)

Fig. 5.6. Time history of local force exerted on the upstream face of the square structure: (a) LC3; and (b) LC5 ($x = \pm 0.0$).

Downstream Face

Figures 5.7(a) and (b) show time histories of the forces measured by the load cell on the downstream face of the square structure when the structure was located at $x = +1.50$ and ± 0.0 m, respectively. It is observed that the pattern of the time histories is the same as for the upstream face of the structure, with reduced magnitudes. These forces represent only hydrostatic pressure in absence of drag. Maximum forces are smaller when the structure is located further downstream. This pattern indicates a reduction of bore height as the bore travels downstream, and is in agreement with measured forces on the upstream face of the structure, discussed in the previous section.

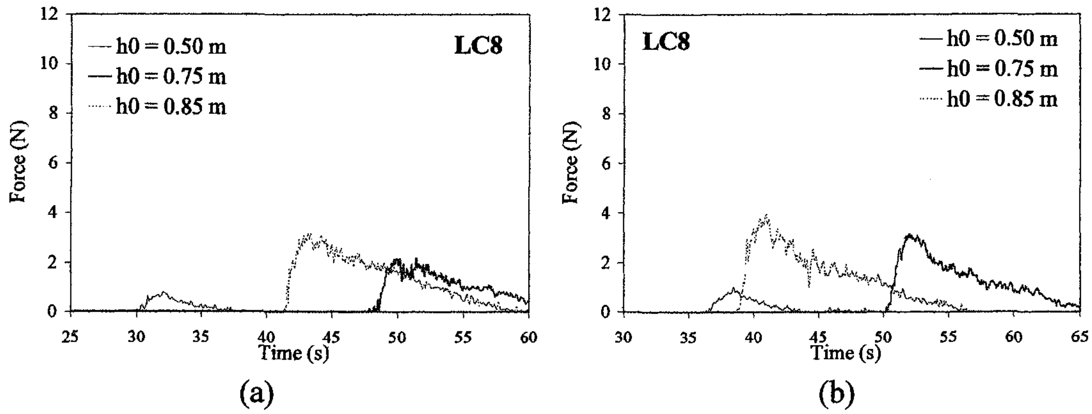

Fig. 5.7. Time history of local force exerted on the downstream face of the square structure: (a) $x = +1.5$ m; and (b) $x = \pm 0.0$ m.

Lateral Sides

Figures 5.8 and 5.9 show time histories of the forces measured by load cells on the lateral sides of the square structure when the structure was located at $x = \pm 0.0$ and $+1.50$ respectively. The local forces acting on the sides of the square structure were smaller when the structure was located further downstream, which could be due to the smaller bore height at this location. It is observed that significant oscillations exist in time history of the forces. It should be noted that forces exerted on the sides of the structure are expected to be fluctuating between negative and positive values. However, the load cells used in the experiments are only able to capture forces in one direction, and therefore the suction forces on the sides of the structure are not measured.

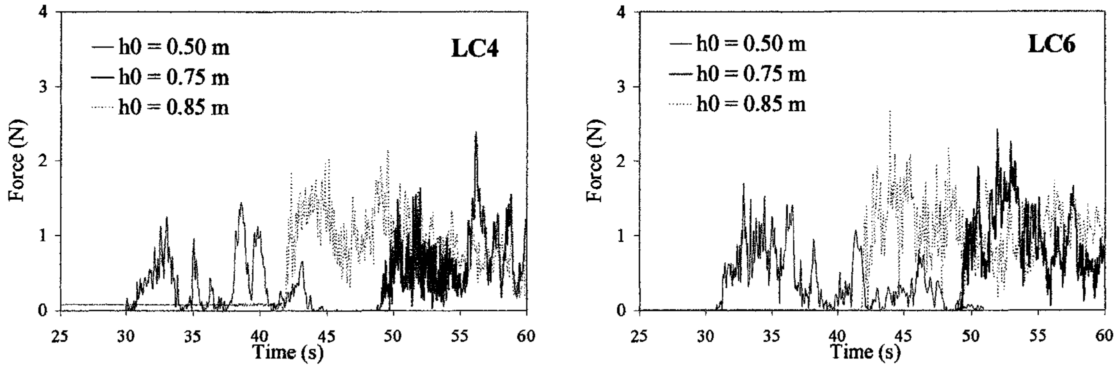

(a) (b)

Fig. 5.8. Time history of force exerted on the (a) left (LC4); and (b) right (LC6) side of the square structure ($x = \pm 0.0$).

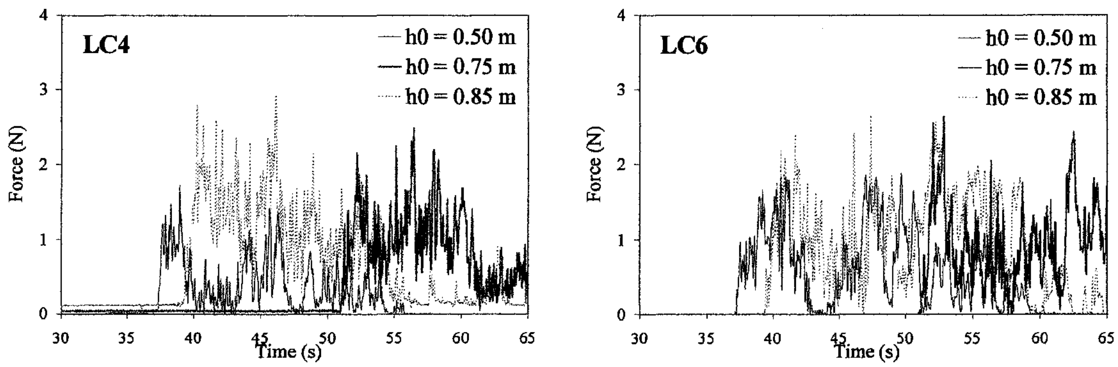

(a) (b)

Fig. 5.9. Time history of force exerted on the (a) left (LC4); and (b) right (LC6) side of the square structure ($x = +1.50$).

5.3.3 Runup

It is expected that a relation exists between the runup at the structure and the exerted force. Haritos *et al.* (2005) obtained a prediction of the forces exerted on a vertical wall due to bore impact using a numerical model. Four points (wave slamming, initiation of runup, maximum runup and post-slamming peak were specified on the time history of the force shown in Fig. 5.10. As explained in Sec. 4.6, wave gauges were used in the experimental program in order to measure the runup at the upstream and downstream face of the structures. Fig. 5.11 shows an example of the runup and horizontal force measured by the wave gauges and dynamometer respectively in Test Series 3. It is observed that contrary to Fig. 5.10, the runup initiates with the sudden rise in the exerted force, simultaneously (this is based on the understanding that Haritos *et al.* 2005 used the same definition for runup as the one used in this study i.e., 'water depth at the face of the structure', as opposed to 'water depth greater than steady bore height'). The maximum runup occurs shortly after the initial force peak, indicating that the first abrupt rise in the force is caused mainly by the impact of the bore front and is not affected by the runup. Maximum runup is associated with a gradual increase in the force and it is likely that it contributes to a post-slamming peak as shown in Fig. 5.11. The measured runup at the structure is approximately constant for a period of 10 s, which depends on the length of the reservoir and volume of water held behind the gate. The same trend is observed in the exerted force. Finally, the runup and exerted force gradually decrease as the water level decreases in the reservoir.

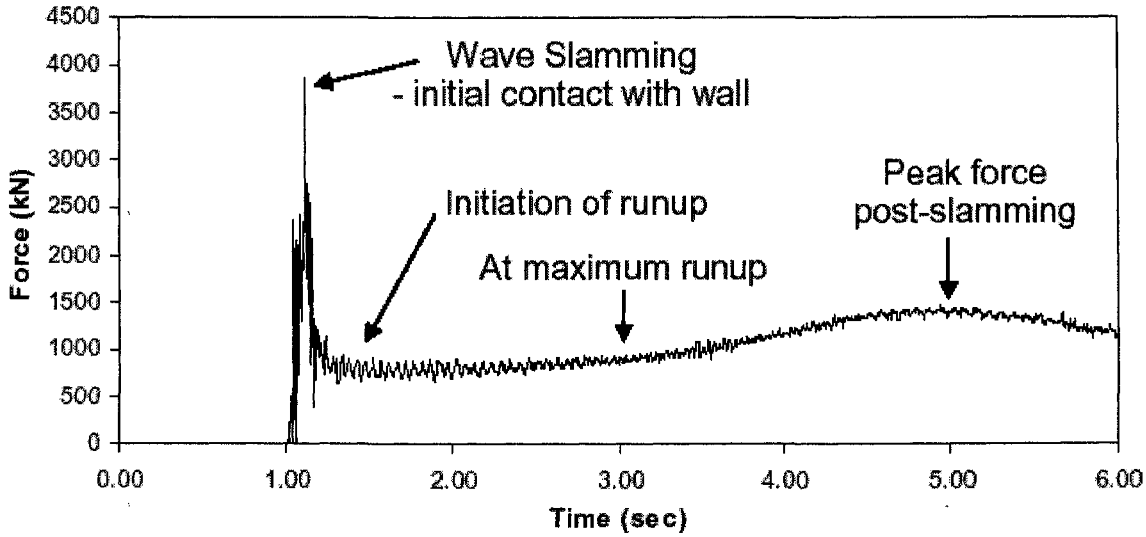

Fig. 5.10. Tsunami force on a rigid vertical wall (Haritos *et al.* 2005).

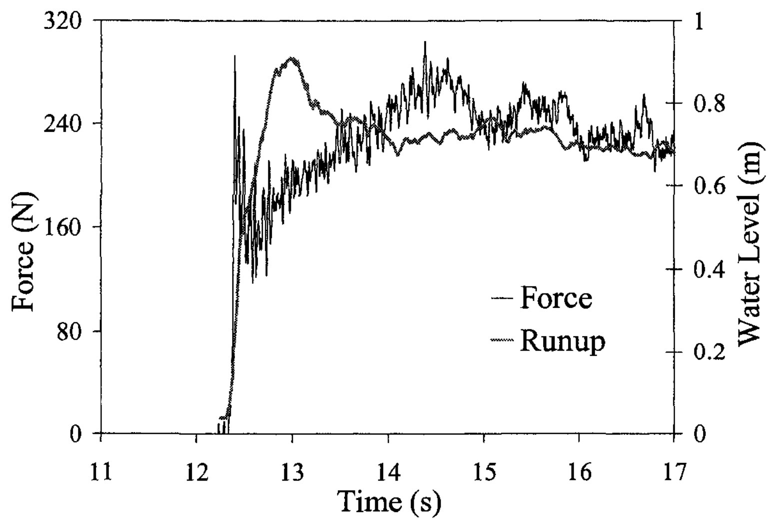

Fig. 5.11. Measured runup and exerted force on the circular structure.

5.3.4 Time History of Pressures

Upstream Face

Fig. 5.12 shows time histories of the pressure exerted on the upstream face of the circular structure due to bores generated with impoundment depths of h_0 = 0.5, 0.75, 0.85 and 1.0 m, measured at P5, P10, P20 and P25. It should be noted that Fig. 5.4 and Fig. 5.12 are based on results obtained from the same test from Test Series 3.

A sudden rise is observed in the time history of the exerted pressure, which corresponds to the impact of the bore front on the upstream face of the structure. Unlike the exerted forces, the initial rise is the global peak in the time history of exerted pressure and the pressure reduces to approximately 50% of this value very quickly. It is observed that the rise time for peak pressures is 0.013, 0.012, 0.010 and 0.009 s for impoundment depths of h_0 = 0.5, 0.75, 0.85 and 1.0 m, respectively. The rise times for peak pressure are approximately 20% of the corresponding force rise times for the same hydraulic bore. This impulsive pressure is followed by oscillations that indicate presence of entrapped air. Then, the measured pressure reduces to an approximately constant value equal to calculated pressure from the corresponding runup based on a hydrostatic distribution.

Fig. 5.12 also shows that an impulsive pressure was recorded for P5, P10 and P20 (only for h_0 = 1.0 m) whereas such a sudden rise was not recorded at P25 and the measured pressure increased gradually and approached a line parallel to other time histories. This observation suggests that the initial bore height was less than the height of P25. Therefore, the pressure is not due to the impact, but is caused by the bore runup. The runup measurements also endorse this explanation. It can be concluded that impact of a bore front exerts a relatively large pressure whereas pressure exerted by bore runup is significantly less due to vertical accelerations of the flow.

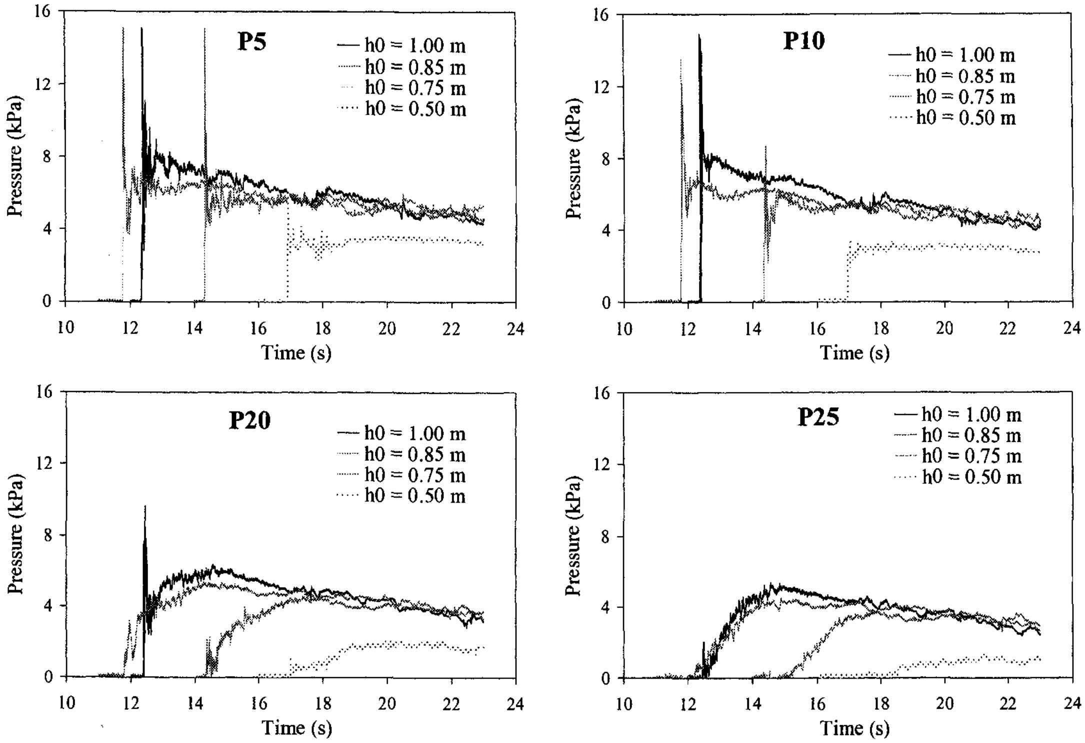

Fig. 5.12. Time history of pressure on the upstream face of the circular structure recorded at: (a) P5; (b) P10; (c) P20; and (d) P25.

Downstream Face

During Test Series 4, the circular structure was rotated 180 degrees such that the pressure transducers were located on the downstream face of structure, facing downstream. Fig. 5.13 shows time histories of pressure exerted on the downstream face of the circular structure due to bores generated with impoundment depths of h_0 = 0.75 and 1.0 m, measured at P5, P10, P20 and P25. It is observed that larger oscillations exist in the pressure time histories. The bore height measured by wave gauges near the downstream face of the structure demonstrated the same trend. This is most likely caused by the strong turbulent wake occurring at the back of the structure. The videos taken during the tests illustrate this wake and the resulting fluctuation in bore height at the back of the structure and endorse this explanation. It is also observed that the time histories of pressure on the downstream face differ markedly from those on the upstream face. The pressure increases to a peak value very slowly with rise times of 3.2 and 2.4 s for impoundment depths of h_0 = 0.75 and 1.00, respectively. The rise times are approximately two times larger than the corresponding values for pressure rise times on the upstream face. It should be noted that the measured pressures shown in Fig. 5.13 are similar to measurements recorded by P25 as shown in Fig. 5.12 (d). This similarity suggests that both pressures are caused by a gradual increase of water level at the structure's face that results in gradual rise of the pressure to the hydrostatic value.

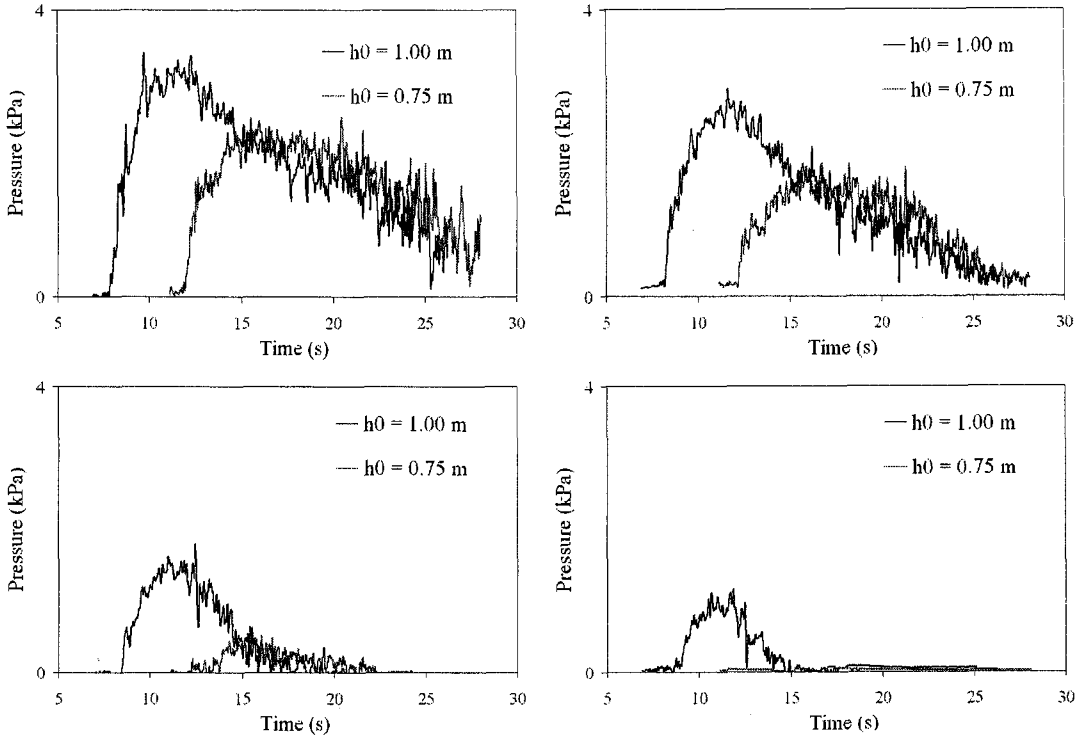

Fig. 5.13. Time history of pressure on the downstream face of the circular structure recorded at: (a) P5; (b) P10; (c) P20; and (d) P25.

Lateral Sides

The circular structure was rotated 90 degrees clockwise, such that the pressure transducers were located on the left side of structure, facing the side of the flume. Fig. 5.14 shows the time histories of the pressure measured on the side of the circular structure due to bores generated with impoundment depths of h_0 = 0.75 and 1.0 m measured at P5, P10, P20 and P25 from Test series 4. It is observed that a negative pressure (suction) is exerted on the sides of the circular structure. The pressure magnitude is less than the corresponding values for the upstream and downstream faces of the structure.

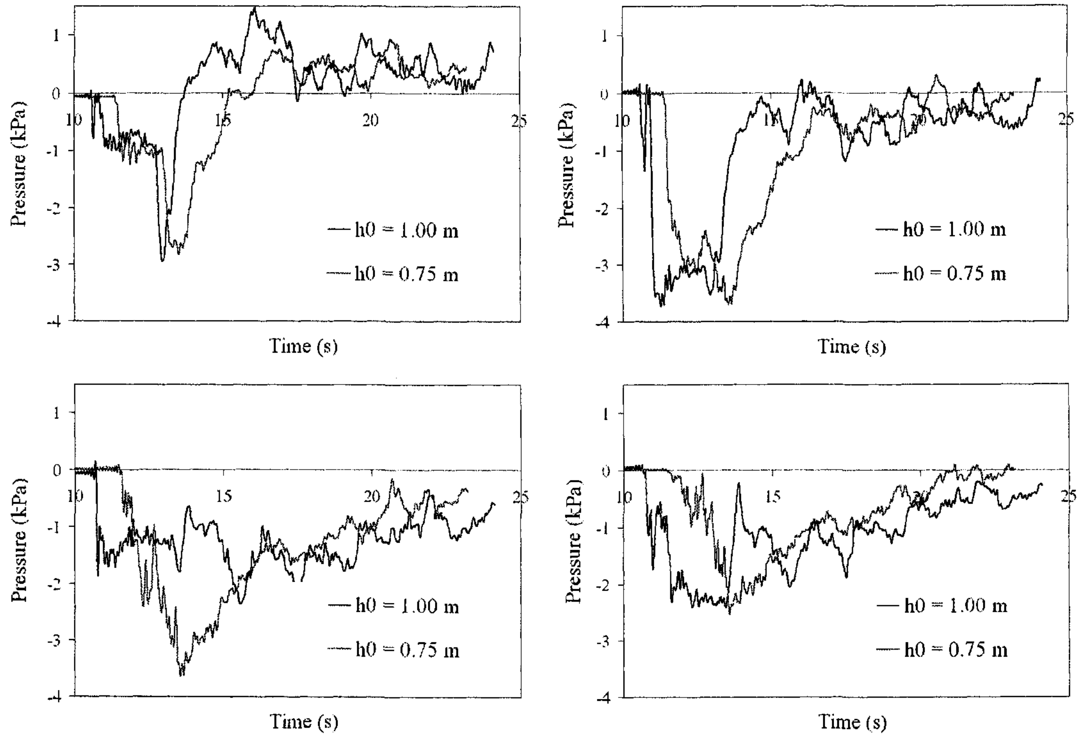

Fig. 5.14. Time history of exerted pressures on the left side of the circular structure recorded at: (a) P5; (b) P10; (c) P20; and (d) P25.

5.3.5 Vertical Pressure Distribution

Upstream Face

As discussed in Chapter 2, there is a lack of reliable experimental data on the temporal variation and vertical distribution of the force/pressure exerted on a structure by the impact of a hydraulic bore. Fig. 5.15 shows the variation of the vertical distribution of the pressure exerted on the circular structure from the impact of a bore generated by an impoundment depth of 1.0 m (where t = 0.0 s is the instant when the bore reaches the structure). Experiments were also carried out with impoundment depths of 0.5, 0.75 and 0.85 m, and similar variations and distributions of pressure were observed. Selected snapshots of the pressure distributions are shown in Fig. 5.15.

Fig. 5.15 (a) shows that, after the bore reaches the structure, the pressure measured by P5 suddenly increases to a maximum pressure of p = 15.1 kPa (t = 0.004 s). This is followed by the same trend at P10, Fig. 5.15 (b). Next, and as the runup height in front of the structure increases, pressure starts to increase at P20 and P25, while the maximum pressures at P5 and P10 diminish to approximately 50 to 75% of their values at previous time steps (Fig. 5.15 (c)). Finally, as the bore approaches a semi-steady condition, the pressure distribution remains almost constant, with the point of maximum pressure at approximately 40% of the bore height, Fig. 5.15 (d). However, this does not seem to be in agreement with Fig. 2.11. Future studies with a higher concentration of measurements close to the bottom may be able to explain the disagreement between Fig. 5.15 and Fig. 2.11.

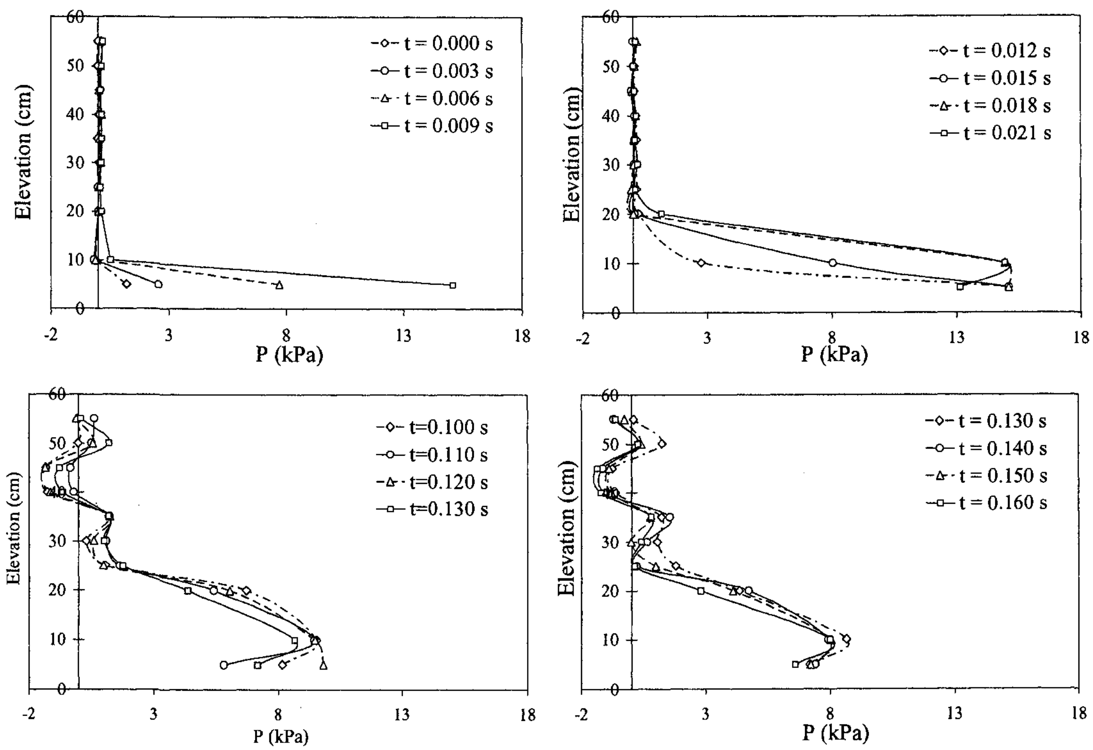

Fig. 5.15. Variation of the vertical pressure distribution on the upstream face of the circular structure for a bore generated with an impoundment depth of h_0 = 1.0 m.

An interesting aspect is that, the recorded pressure distribution is significantly different from the hydrostatic distribution (triangular) from the bottom of the flume up to 10 cm along the height of the structure. Gomez-Gesteira and Dalrymple (2004) have referred to an experiment performed by Yeh and Petroff where the same trend was observed (Fig. 2.11). This could be due to oscillations caused by air entrapment. However, time histories of pressure measured at P5, P10, P20 and P25 shown in Fig. 5.16 do not support this explanation. Surprisingly, the pressure at P10 overshoots the measured pressure at P5, and led to the current pressure distribution.

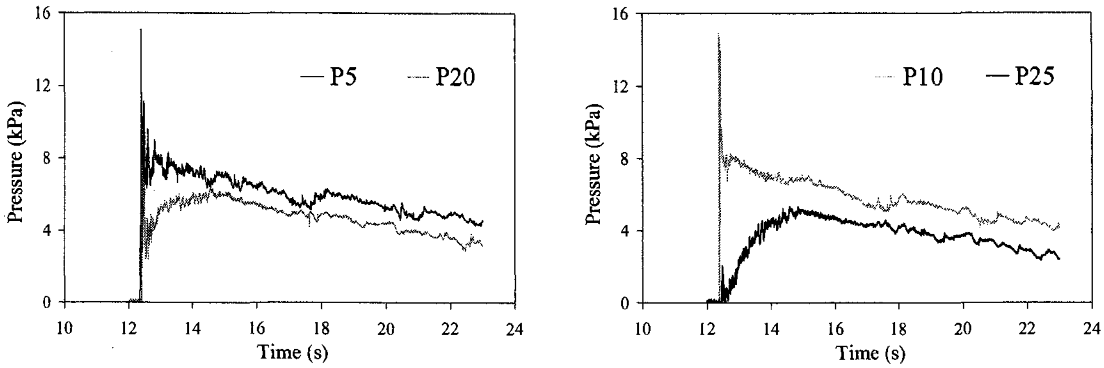

Fig. 5.16. Time histories of pressure on the upstream face of the circular structure: (a)P5 & P20; (b)P10 & P20 (bore was generated with impoundment depth of h_0 =1.0 m).

Lateral Sides

Fig. 5.17 shows the variation of the vertical distribution of pressure exerted on the side of the circular structure due the bore generated by an impoundment depth of 1.0 m. The data were obtained in Test Series 4, and, here, t = 0.0 s is the instant when the bore front reaches the side of the structure.

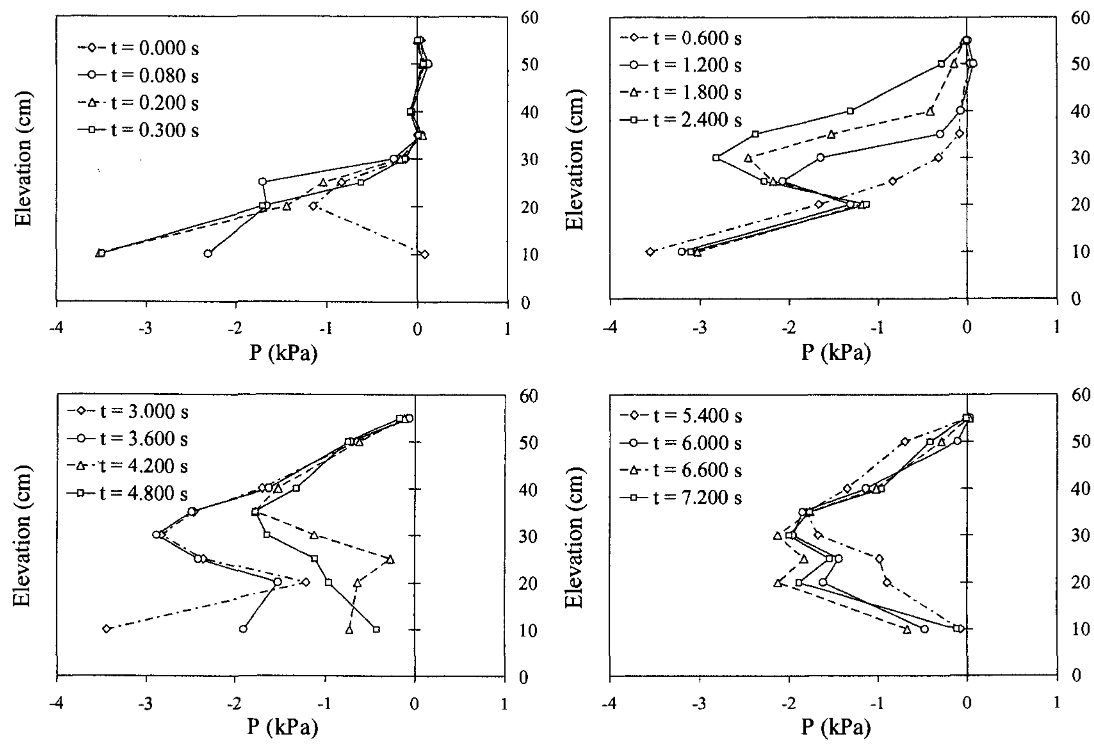

Fig. 5.17. Variation of the vertical pressure distribution on the lateral left side of the circular structure (bore generated with impoundment depth of h_0 = 1.0 m).

The pressure distributions, shown in Fig. 5.17, are clearly different from a hydrostatic (triangular) distribution. It is observed that maximum pressure is exerted at P30 (i.e. 0.30

m above the bottom of the flume). However, it seems that after t = 5.4 s, the pressure distribution is approaching a distribution that can be approximated by a triangle with its maximum at mid-height of the bore runup.

Downstream Face

Fig. 5.18 and Fig. 5.19 show the variation of the vertical distribution of pressure exerted on the downstream face of the circular structure from the impact of a bore generated by an impoundment depth of 1.0 and 0.75 m, respectively. The data were obtained during Test Series 4 and here, t = 0.0 s is the instant that the bore front reaches the downstream face of the structure.

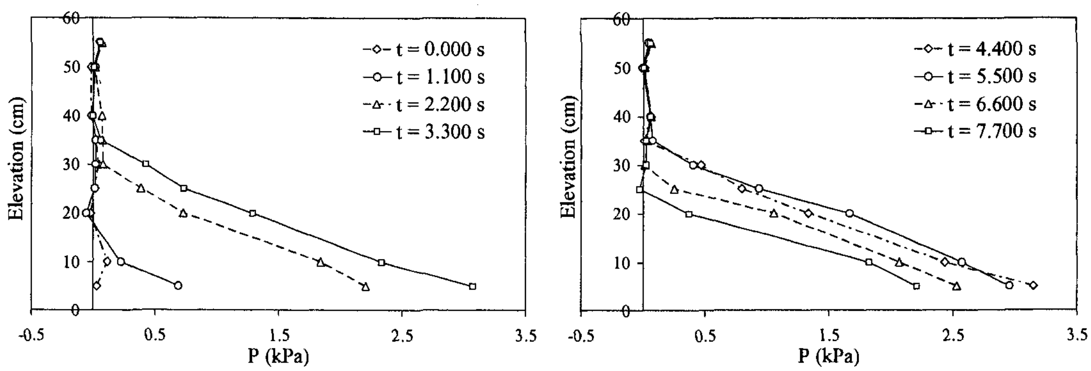

Fig. 5.18. Variation of pressure distribution on the downstream face of the circular structure (bore generated with impoundment depth of h_0 = 1.0 m).

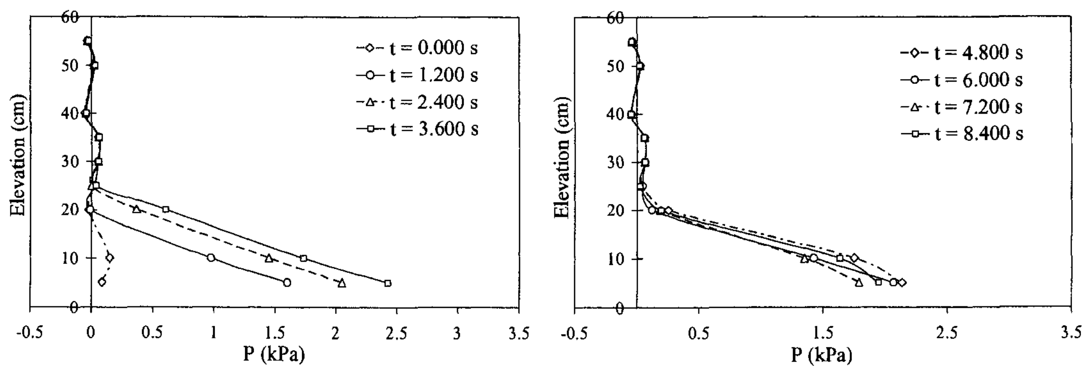

Fig. 5.19. Variation of vertical pressure distribution on the downstream face of the circular structure (bore generated with impoundment depth of h_0 = 0.75 m).

It is observed that the pressure gradually increases to its maximum over the rise time while the pressure distribution is hydrostatic. Then, after reaching the peak pressure, a gradual decrease is observed while the pressure distribution still remains hydrostatic.

5.4. The Effect of Upstream Obstacles

5.4.1 Flow

In order to quantify the effect of constrictions on flow characteristics, bore-front velocities were measured downstream of the flow constrictions using the method described in Sec. 5.2.1. Wave front velocities were measured using four wave gauges that were arranged in two rows at a distance of 0.3 m apart along the longitudinal axis of the flume. The first row was located 0.6 m downstream from the end of the constriction. The wave front velocity was calculated from the averaged measured time difference of the bore height reaching the same specific water depth (0.06 m) in both rows. Fig. 5.20 shows the ratio of measured velocities with and without constrictions. This figure shows that as the blockage ratio increases, the ratio of velocities decreases up to 20% for the case of blockage ratio equal to 0.45. These results show that the variation in bore-front velocity with blockage ratio is complex and also depends on the initial impoundment depth. For $h_0 = 0.5$ m, the bore-front velocity decreases with increasing blockage ratio.

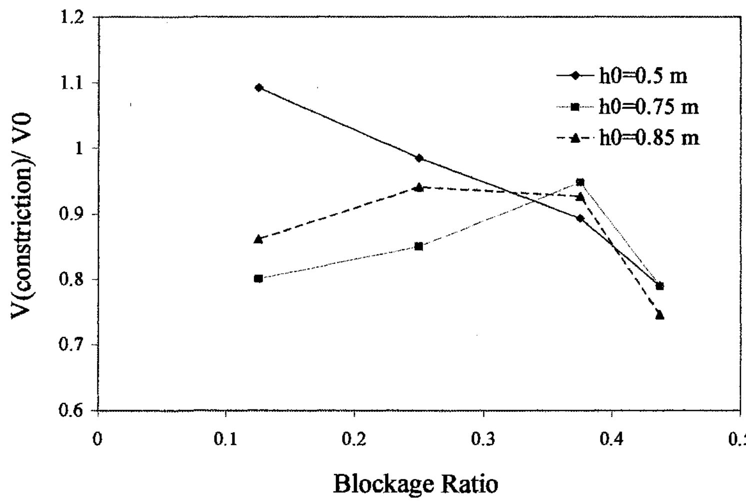

Fig. 5.20. Effect of blockage ratio on downstream bore-front velocities.

5.4.2 Force

5.4.3 Local Force

Upstream Obstacle: Constrictions

Local forces on all sides of the square structure were measured in Test Series 9 in order to investigate the effect of upstream obstacles on the local force. In this case, constrictions were installed between the gate and the test structure as described in Sec. 4.4.1. Time histories of forces measured on the upstream face of structure with and without constrictions are compared in Figs. 5.21 and 5.22, respectively. The measured forces are due to bores generated with impoundment depths of $h_0 = 0.50$, 0.75 and 0.85 m and are shown for various Blockage Ratios (BR). Comparison of exerted forces with and without upstream obstacles (Figs. 5.21 with Fig. 5.5) indicates that the general form of the time history has remained constant. However, it was observed that the presence of upstream obstacles, led to a sudden rise of the force due to impact of the bore front and result in a global peak force. This is consistent with the explanation provided in Sec. 5.3.2. Since the upstream obstacles would most likely affect the bore front impact, the difference in the exerted force would be only in the initial sudden rise of the force. This is observed in Fig. 5.21, where the initial impulsive force is increased up to 125, 140 and 125% for blockage ratios of BR = 0.125, 0.250 and 0.375, respectively.

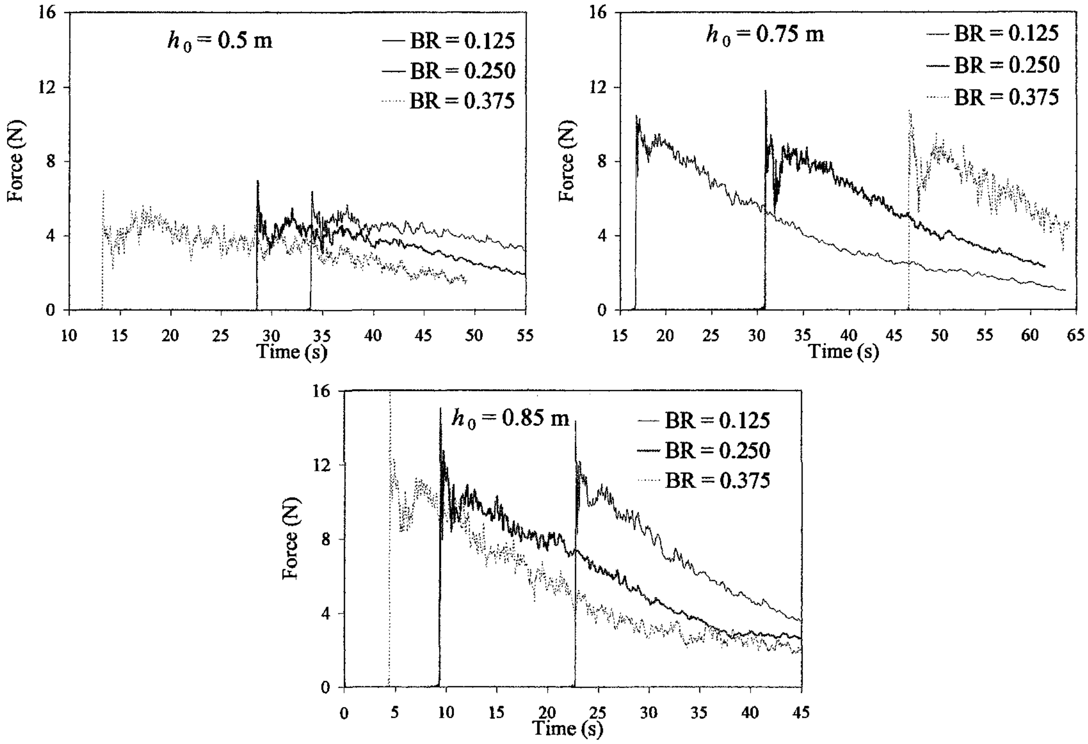

Fig. 5.21. Effect of upstream obstacles on the local force on the upstream face of the square structure (LC3): (a) h_0 = 0.50 m; (b) h_0 = 0.75 m; and (c) h_0 = 0.85 m.

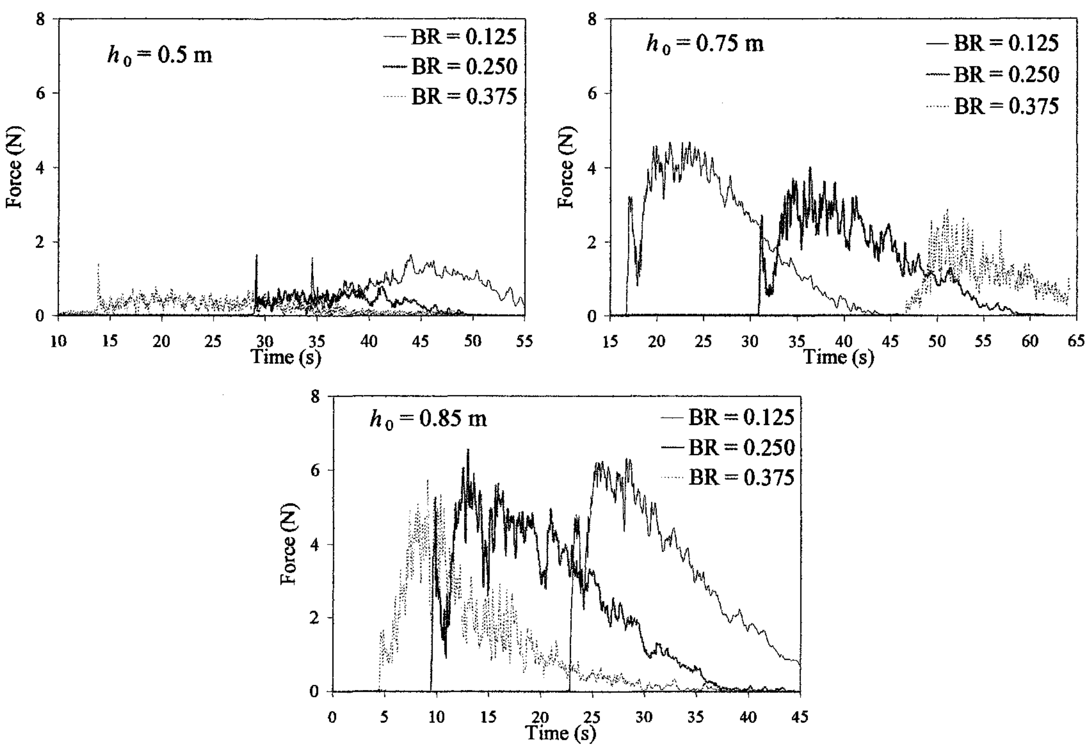

Fig. 5.22. Effect of upstream obstacles on exerted force on the square structure (LC5): (a) h_0 = 0.50 m; (b) h_0 = 0.75 m; and (c) h_0 = 0.85 m.

Local forces on the sides of the diamond structure were measured in Test Series 11 in order to investigate the effect of upstream obstacles on these forces. The upstream obstacle was in the form of constrictions with varying width, as explained in Sec. 4.4.1. Time histories of forces measured on one of the upstream faces of the structure measured by the bottom load cell (LC3) are shown in Fig. 5.23. The measured forces are due to bores generated with impoundment depths of h_0 = 0.50, 0.75 and 0.85 m and are shown for various Blockage Ratios (BR). Expectedly, it is observed that forcing increases with increasing impoundment depth. Also, the pattern of the time history is approximately the same for all cases and demonstrates the sudden rise of the force due to bore front impact. Comparison of the local forces measured on the square and diamond structures indicates that forces on the upstream sides of the latter are significantly less (up to 40%). This reduction in forcing was expected since for the case of the diamond structure, the sides are oriented at 45° with regards to the flow and bore impact is less compared to the case of the square structure.

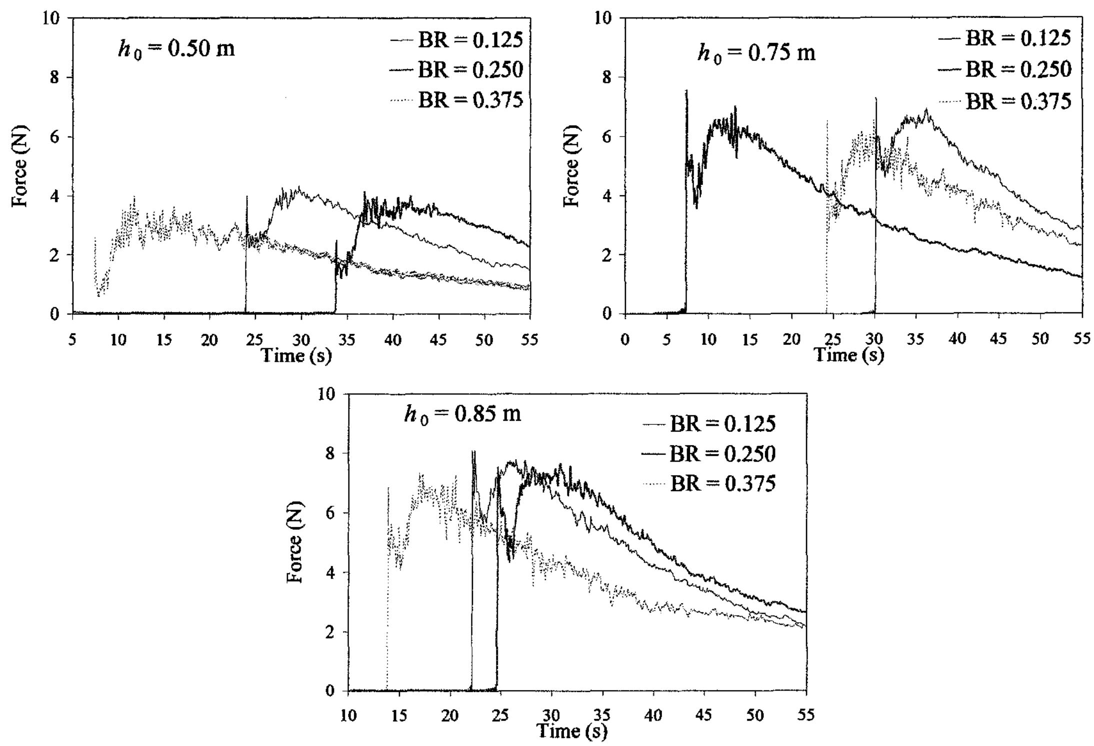

Fig. 5.23. Effect of upstream obstacles on exerted force on the diamond structure (LC3): (a) h_0 = 0.50 m; (b) h_0 = 0.75 m; and (c) h_0 = 0.85 m

5.5. Debris Impact Force

Test Series 5 was performed to study the impact of floating debris on structures in terms of exerted force, the period over which the force is exerted and parameters that affect the force such as impact orientation. As discussed in Sec. 4.6.3, tests were performed using *small* and *large* wooden logs with impoundment depths of 0.75 m and 1.0 m. Fig. 5.24 shows an example of the time history of global horizontal force measured on the circular structure in the direction of flow due to a bore with debris impact generated with impoundment depth of 0.75 m. There is a sudden rise in the recorded force at $t = 29.4$ s where the force reaches approximately 150 N due to the initial bore impact. This is followed by an abrupt increase up to approximately 650 N and a reduction in the time history due to debris impact at approximately $t = 29.6$ s. In some cases, after the first impact, the wooden log bounced back and impacted the structure a second time, leading to two force peaks as shown in Fig. 5.25. The second peak was always less (up to 28%) than the first peak and therefore the initial peak in the recorded force was selected as the maximum impact force.

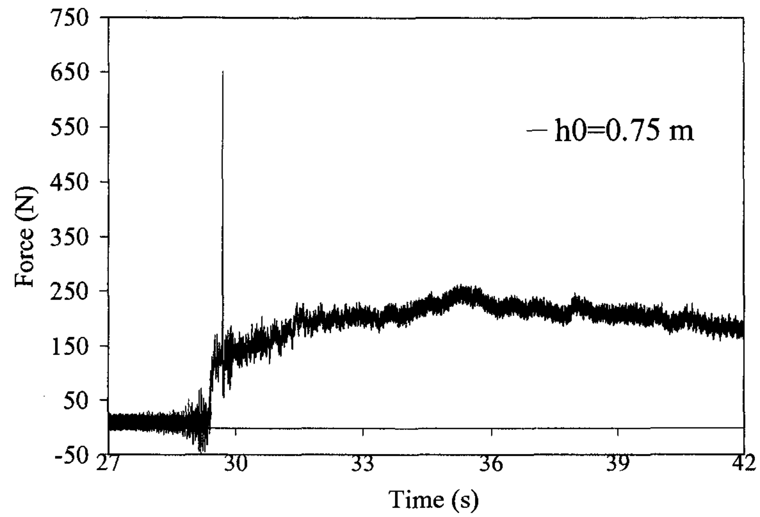

Fig. 5.24. Global horizontal force on the circular structure due to the impact of *large* log conveyed by a bore generated from an impoundment depth of $h_0 = 0.75$ m.

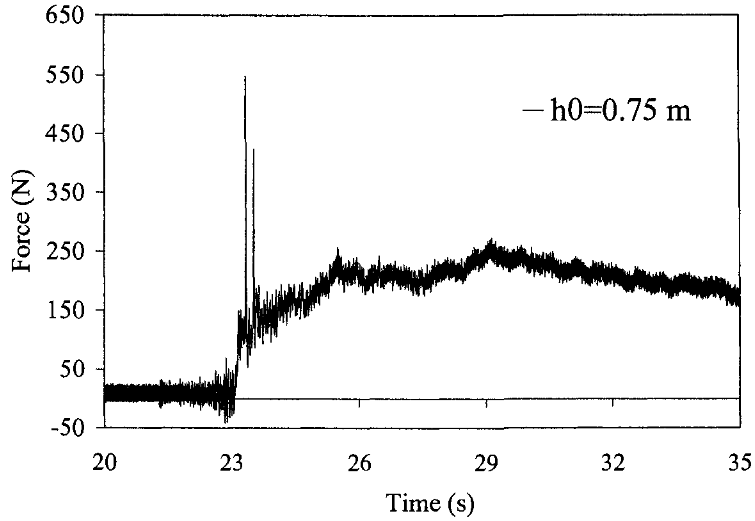

Fig. 5.25. Global horizontal force on the circular structure due to the impact of *large* log conveyed by a bore generated from an impoundment depth of h_0 = 0.75 m.

5.5.1 Impact Duration

The recorded time history in Fig. 5.24 is shown on an expanded time scale in Fig. 5.26 where the force increases from 150 N to 650 N (t = 29.682 s to 29.689 s) and reduces back to the previous level (t = 29.689 s and 29.696 s) in the form of a triangle force impulse. Impact durations, t_1, (the time between the initial contact of the debris with the structure and the maximum impact force) can be obtained from the time history of exerted force and equals t_1 = 0.007 s in this case. Similar calculations were performed in order to obtain the impact durations for all the performed tests. Average impact duration was found to be t_1 = 0.0075 s with a regression coefficient of r = 0.995 for the tests with varying flow velocities using both the *small* and *large* logs. Also, the obtained impact durations are approximately the same for the small and large log. The results suggest that impact duration is independent of log mass and velocity. However, this is not in agreement with Haehnel and Daly's (2002) statement that impact duration depends on the mass of the debris and the contact stiffness of the interaction.

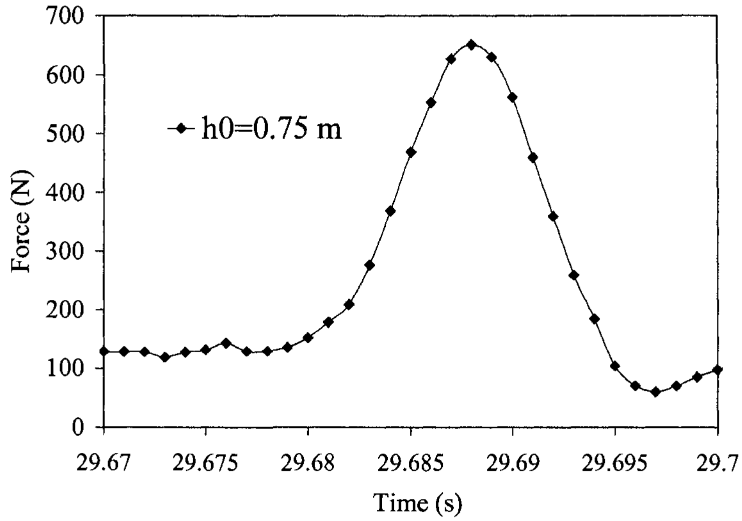

Fig. 5.26. Time history of force shown in Fig. 5.24 on expanded time scale.

Fig. 5.27 shows the recorded time history shown in Fig. 5.25 on expanded scale where the *large* log hit the structure twice. Videos taken during the test showed that the log rebounded from the first impact, and was again carried by the flow to the point of impact. The obtained impact duration equals $t_1 = 0.007$ s for both first and second peak. Since the log velocity was significantly reduced after the first impact, the measurements suggest that impact duration was not influenced by the log velocity in these tests.

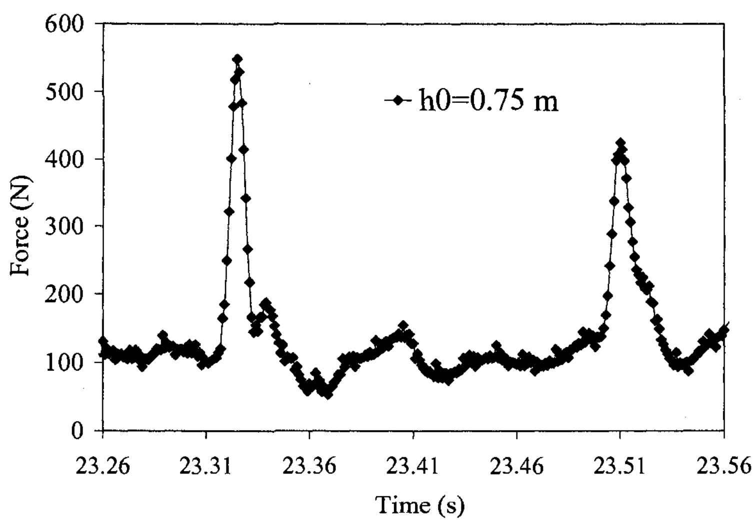

Fig. 5.27. Time history of force shown in Fig. 5.25 on expanded time scale where the log hit the structure twice.

Probability of Maximum Debris Impact Occurring

The common approaches for estimation of debris impact forces (see Sec. 2.4) can be used to estimate the maximum impact force that may be exerted on a structure due to debris. However, there is a lack of knowledge about probability of impact force and geometry. In order to investigate the probability of debris impact on the structure, tests with the *large* log were repeated 20 times. As explained in Section 4.6.5, the log was placed in the flume 2 m upstream and in line with the structure and released. The log was then allowed to flow freely until it impacted the structure while the two strings prevented the log from reaching the end of the flume. It was found that of the 20 logs released during this test, 7 missed the load frame entirely. Although the log was exactly placed at the same place upstream of the structure, relatively large scatter in obtained results in terms of maximum impact force was observed. Moreover, various impact geometries were observed in the videos taken during the tests. These observations confirmed that controlling specific impact geometry is almost impossible for an object moving with the flow. The frequency distribution of the maximum impact force for the 13 cases where the log struck the structure is shown in Fig. 5.28. A single peak is observed for the impact forces of 450-500 N. While the test was not repeated enough times to represent a statistics sample, it is clear that the highly irregular flows caused the orientation impact (mainly, the angle of impact) to vary, which affected the maximum impact forces.

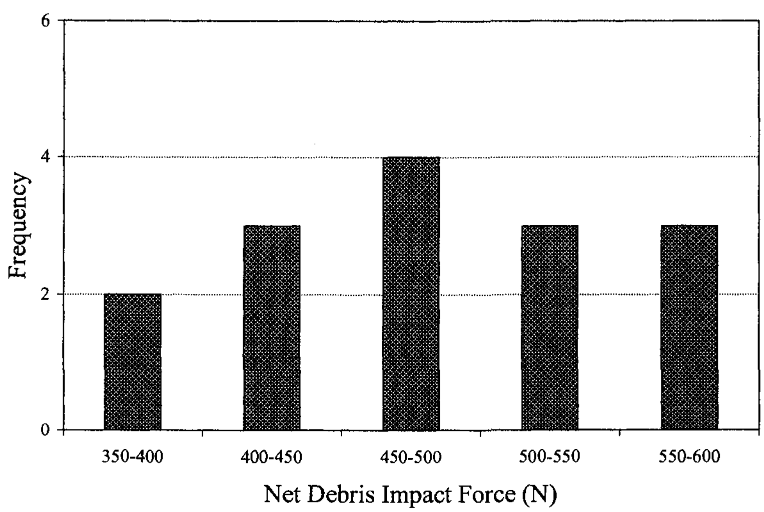

Fig. 5.28. Frequency of net debris impact force obtained from repeating a test 20 times where the log did not hit the structure seven times.

Chapter 6. Structural Analysis

In this section tsunami-induced forces are calculated for a prototype structure and comparison of existing codes and guidelines in terms of the forces are presented. Furthermore, effects of dynamic behaviour of a typical gate structure under tsunami-induced forces will be investigated.

6.1. Design Example

Building codes provide guidance for the design of lateral force resisting systems subjected to wind and seismic excitations. Tsunami-induced loading is normally not considered. The objective of this example is to demonstrate the levels of lateral loading associated with tsunamis for a prototype reinforced concrete building located in a tsunami-prone area. Specifically, the loads generated by a tsunami bore are addressed. Other researchers have provided comparisons between tsunami loading and other lateral loads (Okada *et al.* 2005, Pacheco and Robertson 2005, Nouri *et al.* 2007 and Palermo *et al.* 2007).

The following example consists of a moment-resisting frame with simple geometry, as shown in Fig. 6.1. The thickness of the slab is assumed to be 200 mm, and the beams are 450 mm deep (including the thickness of the slab) and 300 mm wide. The exterior and interior columns are 450 mm and 500 mm square sections, respectively. The centre-to-centre storey heights are 3.65 m and a 10-storey structure is considered.

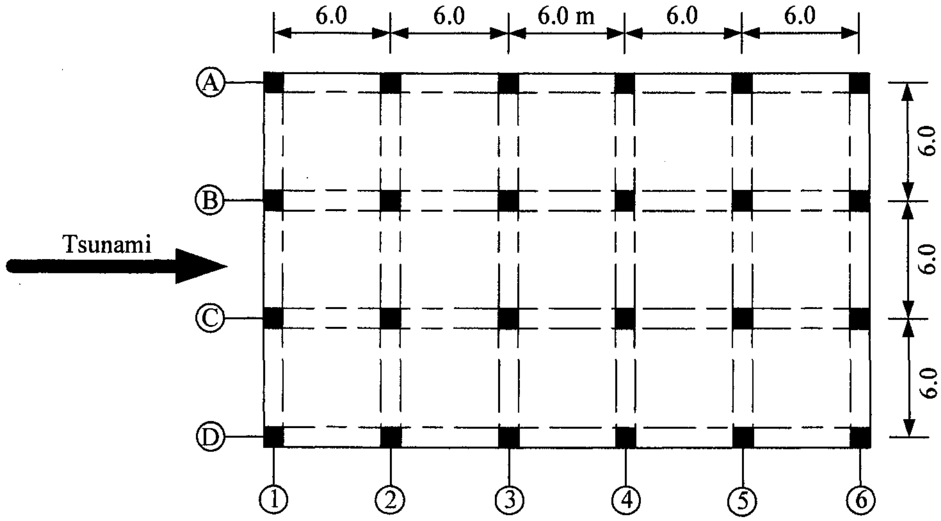

Fig. 6.1. Plan view of structural layout of reinforced concrete moment-resisting frame.

The components of the tsunami-induced forces are calculated based on CCH, FEMA 55 and SMBTR. The calculation of tsunami-induced loads require a number of assumptions, together with engineering judgment and lessons from reconnaissance missions in regions affected by tsunamis. The author assumes that the net hydrostatic force exerted on the lateral system is zero in calculating the base shear. The surge and drag forces require an effective area for load transfer to the lateral force resisting system. In this example, two scenarios are considered: (1) 100% breakaway walls, which expose the structural elements; and (2) non-breakaway walls. In the latter, the exterior non-structural elements remain intact. For breakaway walls the external elements will be damaged and all the columns of the structure will be subjected to drag force. The forces are calculated for inundation depths of 1 to 5 m, and the structure is oriented with its short side parallel to the shoreline. When designing structures located in tsunami prone areas, the inundation depth at a specific location should be obtained from tsunami inundation hazard maps, when available. Otherwise, numerical modeling based on site-specific characteristics should be conducted in order to estimate the tsunami inundation depth.

6.1.1 Hydrodynamic (Drag) Forces

For the case where 100% breakaway walls are assumed and the columns are exposed to the hydraulic bore, the drag forces are based on a drag coefficient of 2.0 for square columns, as recommended by CCH and FEMA 55. For the second case, non-breakaway walls are assumed to remain intact and the hydraulic bore impacts the entire surface of the building. In this situation, the drag coefficient is taken as 1.5 and 1.25 for CCH and FEMA 55, respectively.

6.1.2 Debris Impact Forces

To calculate debris impact, a mass of 455 kg is used to represent a floating object at the water surface. The mass used is consistent with the recommendations of CCH and FEMA 55. In this example, it is assumed that the debris will impact a single reinforced concrete column. CCH assumes duration of 0.1 s for concrete structures. FEMA 55 recommends an impact duration ranging from 0.3 to 0.6 s for reinforced concrete piles or columns. Hence, impact duration of 0.3 s is assumed in the design example.

6.1.3 Surge Forces

In this example, the surge force is applied over the full length of the building in the direction of the tsunami for non-breakaway walls. For the case of 100% breakaway walls, it is assumed that the surge force will develop on the four exterior columns which face the hydraulic bore. Note that the surge force is not applicable for FEMA 55 and that SMBTR assumes a different surge force per unit width for columns and walls.

6.1.4 Sample Calculations: Breakaway Walls

The following is a sample calculation for breakaway walls for the given structure subjected to a tsunami inundation depth of 5 m.

$g = 9.81 \, m/s^2 \qquad \rho = 1030 \, kg/m^3 \qquad d_s = 5m$

Surge Force:

$$F_S = 2.0\rho g h^2 = 2.0\left(1030 \, kg/m^3\right)\left(9.81 \, m/s^2\right)(5m)^2 = 0.505 \times 10^6 \, N/m \quad \text{SMBTR}$$

$$F_S \times width = \left(0.505 \times 10^6 \, N/m\right)(4(0.45m)) = 909 \times 10^3 N = 909kN$$

$$F_S = 4.5\rho g h^2 = 4.5\left(1030 \, kg/m^3\right)\left(9.81 \, m/s^2\right)(5m)^2 = 1.14 \times 10^6 \, N/m \quad \text{CCH}$$

$$F_S \times width = \left(1.14 \times 10^6 \, N/m\right)(4(0.45m)) = 2046 \times 10^3 N = 2046kN$$

Drag Force:

$$F_D = \frac{\rho C_D A u^2}{2}$$

$$u = C\sqrt{gd_s} = 2\sqrt{\left(9.81\,{}^{m}\!/\!_{s^2}\right)(5m)} = 14\,{}^{m}\!/\!_{s}$$ FEMA 55

$$u = d_s = 5\,{}^{m}\!/\!_{s}$$ CCH

$C_D = 2.0$ Rectangular columns

$$A = (5m)((16 \times 0.45m) + 8(0.50m)) = 56m^2$$

$$F_D = \frac{\left(1030\,{}^{kg}\!/\!_{m^3}\right)(2)\left(56m^2\right)\left(14\,{}^{m}\!/\!_{s}\right)^2}{2} = 11317 \times 10^3 N = 11317kN$$ FEMA 55

$$F_D = \frac{\left(1030\,{}^{kg}\!/\!_{m^3}\right)(2)\left(56m^2\right)\left(5\,{}^{m}\!/\!_{s}\right)^2}{2} = 1442 \times 10^3 N = 1442kN$$ CCH

Debris Impact Force:

$$F_i = m\frac{u_i}{\Delta t} = 455kg\left(\frac{14\,{}^{m}\!/\!_{s}}{0.3s}\right) = 21.2 \times 10^3 N = 21kN$$ FEMA 55

$$F_i = 455kg\left(\frac{5\,{}^{m}\!/\!_{s}}{0.1s}\right) = 22.8 \times 10^3 N = 23kN$$ CCH

6.1.5 Sample Calculations: Non-Breakaway Walls

The following is a sample calculation for non-breakaway walls for the given structure subjected to a tsunami inundation depth of 5 m.

Surge Force:

$$F_S = \left(1.14 \times 10^6\,{}^{N}\!/\!_{m}\right)(18m + 0.45m) = 20973 \times 10^3 N = 20973kN$$ SMBTR/CCH

Drag Force:

$$F_D = \frac{\rho C_D A u^2}{2}$$

$C_D = 1.25$ Walls FEMA 55

$C_D = 1.5$ Walls CCH

$$A = (5m)(18m + 0.45m) = 92m^2$$

$$F_D = \frac{\left(1030 \, {}^{kg}\!/_{m^3}\right)(1.25)(92m^2)\left(14 \, {}^{m}\!/_{s}\right)^2}{2} = 11652 \times 10^3 N = 11652kN \quad \text{FEMA 55}$$

$$F_D = \frac{\left(1030 \, {}^{kg}\!/_{m^3}\right)(1.5)(92m^2)\left(5 \, {}^{m}\!/_{s}\right)^2}{2} = 1782 \times 10^3 N = 1782kN \quad \text{CCH}$$

Debris Impact Force:

$$F_i = m\frac{u_i}{\Delta t} = 455kg\left(\frac{14 \, {}^{m}\!/_{s}}{0.3s}\right) = 21.2 \times 10^3 N = 21kN \quad \text{FEMA 55}$$

$$F_i = 455kg\left(\frac{5 \, {}^{m}\!/_{s}}{0.1s}\right) = 22.8 \times 10^3 N = 23kN \quad \text{CCH}$$

6.1.6 Results

Table 6.1 through Table 6.6 provide the results for calculation of the individual force components for the structure considered using CCH, FEMA 55, and SMBTR, respectively.

Table 6.1. Tsunami-induced force components based on CCH for breakaway walls.

Velocity (m/s)	Surge (kN)	Drag (kN)	Debris Impact (kN)
1	82	12	5
2	327	92	9
3	737	311	14
4	1310	738	18
5	2046	1442	23

Table 6.2. Tsunami-induced force components based on CCH for non-breakaway walls.

Velocity (m/s)	Surge (kN)	Drag (kN)	Debris Impact (kN)
1	839	14	5
2	3356	114	9
3	7550	385	14
4	13423	912	18
5	20973	1782	23

Table 6.3. Tsunami-induced force components based on FEMA 55 for breakaway walls.

Code	Inundation Depth (m)	Velocity (m/s)	Drag (kN)	Debris Impact (kN)
FEMA 55	1	6	453	10
	2	9	1811	13
	3	11	4074	16
	4	13	7243	19
	5	14	11317	21

Table 6.4. Tsunami-induced force components based on FEMA 55 for non-breakaway walls.

Code	Inundation Depth (m)	Velocity (m/s)	Drag (kN)	Debris Impact (kN)
FEMA 55	1	6	466	10
	2	9	1864	13
	3	11	4195	16
	4	13	7457	19
	5	14	11652	21

Table 6.5. Tsunami-induced force components based on SMBTR for breakaway walls.

Code	Inundation Depth (m)	Surge (kN)
SMBTR	1	36
	2	146
	3	327
	4	582
	5	909

Table 6.6. Tsunami-induced force components based on SMBTR for non-breakaway walls.

Code	Inundation Depth (m)	Surge (kN)
SMBTR	1	839
	2	3356
	3	7550
	4	13423
	5	20973

Given the force components, a loading combination must be specified in order to evaluate the maximum tsunami load that would be used for either design or analysis purposes. Yeh *et al.* (2005) suggested loading combinations that are applicable for tsunami loading. CCH does not specifically provide guidance to evaluate the maximum tsunami load. Nouri *et al.* (2007) proposed a two-part loading combination: Initial Impact and Post-

Impact Flow. For this example, the loading combinations are similar to those of Nouri *et al.* Table 6.7 provides the results of the tsunami load calculation for CCH, FEMA 55 and SMBTR for an inundation depth of 5 m based on loading combinations of Nouri *et al.* (2007).

Table 6.7. Tsunami-induced load based on CCH, FEMA 55 and SMBTR for 5 m inundation depth.

Standard	Case	Surge + Impact (kN)	Drag + Impact (kN)	Tsunami Load (kN)
CCH	Breakaway	2069	1465	2069
CCH	Non-breakaway	20995	1804	20995
FEMA 55	Breakaway	N.A.	11338	11338
FEMA 55	Non-breakaway	N.A.	11673	11673
SMBTR	Breakaway	909	N.A.	909
SMBTR	Non-breakaway	20973	N.A.	20973

For the prototype moment-resisting frame structure with the short side perpendicular to the advancing bore, it is apparent that non-breakaway walls or rigid exterior non-structural components can lead to large design base shears. CCH and SMBTR estimate significantly larger base shears relative to FEMA 55 due to the omission of a surge component in FEMA 55. It is evident that the width of exposed surfaces affects the magnitude of total forces exerted on a structure. Therefore, it would be prudent to orient buildings such that the short side is placed parallel to the shoreline. Furthermore, using breakaway or flexible walls at the lower level would reduce the lateral force that is transmitted to the lateral force resisting system. Note that although the debris impact force is a negligible component in the base shear, it could be critical in the design of individual structural components subjected to the debris impact.

6.2. Dynamic Response of Structures due to Tsunami-Induced Forces

Since the surge and debris-impact forces are exerted on structures in a very short period of time, it is important to check the dynamic properties of the structure together with the force rise time. It is known that if the ratio of t_r/T (where t_r is the force rise time and T is the natural period of the structure) is relatively small ($t_r/T << 1$) the structure would "see" the force like an impulsive (suddenly applied) load. On the other hand, the force will affect the structure as a static force if the ratio is large ($t_r/T >> 1$).

Yamamoto *et al.* (2006) surveyed the performance of structures in affected areas of Sri Lanka and Thailand, following the 2004 Indian Ocean tsunami. They performed a structural analysis in order to investigate the forces and moments exerted on structural elements due to the tsunami-induced force. The tsunami-induced force was calculated using the empirical formula proposed by Iizuka and Matsutomi (2000), Eq. 6.1:

$$F = 0.5C\rho u^2, u = 1.1\sqrt{gh} \qquad (6.1)$$

where F is the dynamic pressure due to a tsunami, C is a dimensionless coefficient (= 2.0, in the case of a rectangle section), ρ is the density of sea water, u is the velocity of the tsunami bore, g is the gravitational acceleration, and h is the inundation depth.

Further, they verified the results of the analysis, in terms of destruction or serviceability of structures, with the observed performance of structures. In order to demonstrate the change in structures' response, due to the dynamic effects, a comparison was made between the dynamic and static responses of one of the structures considered by Yamamoto *et al.* (2006). A typical reinforced concrete structure, located in an inland area with a height of D.L. (Datum Level) +5.0 m, in Phuket Island, Thailand was analyzed. An inundation depth of three meters was assumed based on the survey. A gate-type Rahmen building model with a height of three meters and a span of five meters was utilized in the analysis, as in Fig. 6.2. Square pillars with sides of 0.50 m and three reinforcing steel bars of 0.022 m diameter with 0.05 m cover thickness on each side were used. A distributed load per unit length of 20 kN/m, due to upper loads (roof, second floor, etc), was assumed. Further details can be found in Yamamoto *et al.* (2006).

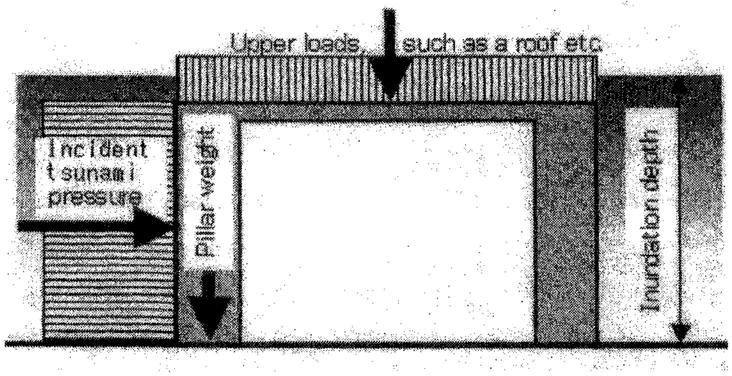

Fig. 6.2. The gate-type Rahmen structural model considered by Yamamoto *et al.* (2006).

The dynamic analysis of the model was performed using the software SAP 2000. The tsunami-induced force was calculated using the same formula as in Yamamoto *et al.* (2006) (Eq. 6.1) in order to make the comparison sensible. Based on the measured time history of the exerted bore-induced force on the structure, and for simplicity, the force was assumed as a step force with finite rise time (Fig. 6.4). While the formula of Iizuka and Matsutomi (2000) recommends the use of a uniform load distribution (Distribution 1), two more distributions were used, based on the results of this study (Distribution 2) and experiments of Yeh and Petroff (see Gomez-Gesteira and Dalrymple, 2004) (Distribution 3). The maximum pressure in these distributions was exerted at 40% and 75% of the bore height respectively, but the total force was equal to the calculated value from Eq. 6.1 as shown in Fig. 6.3.

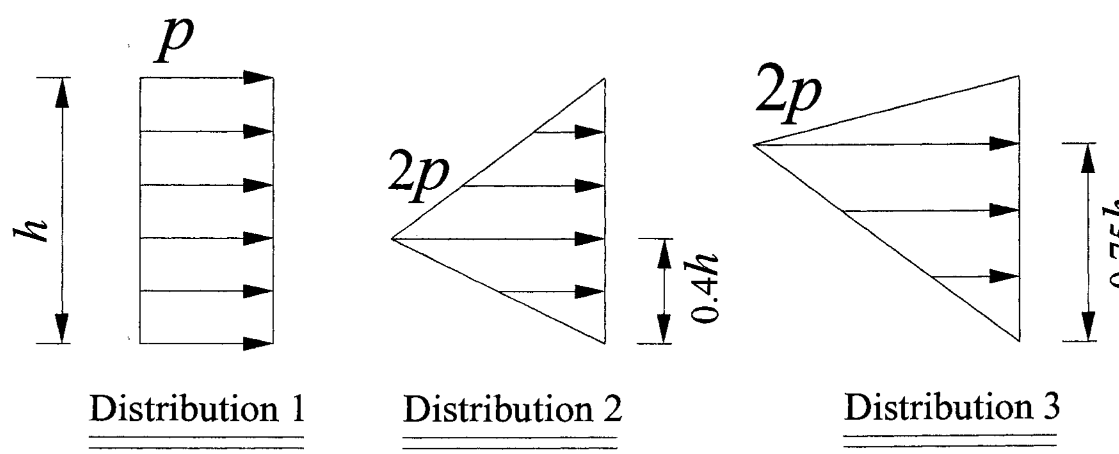

Fig. 6.3. Three distributions used in the analyses.

Fig. 6.5 shows the exerted moments at the base of the sea-side pillar obtained from the dynamic analysis for different ratios of t_r/T. The responses approach the static value of the moment when $t_r/T > 1.0$. However, for the case when $t_r/T < 1.0$, the response oscillates about the static response. It was observed that the moment increased by 25% for the case when $t_r/T = 0.2$ due to dynamic effects. The same trend was observed for the other considered distributions. It should be noted that the results do not include the effect of the upper load.

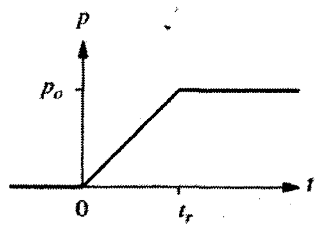

Fig. 6.4. Step force with finite rise time.

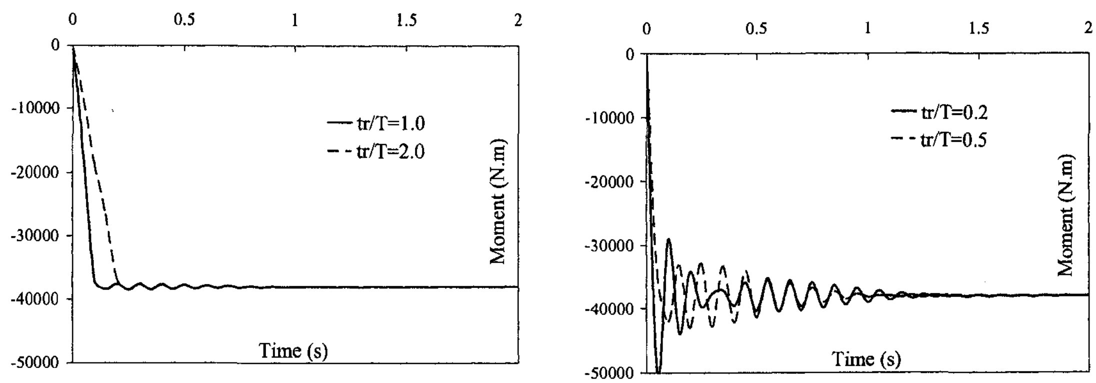

(a) (b)

Fig. 6.5. The change in the exerted moment at the base of the sea-side pillar, due to the ratio of rise time to natural period of the structure: (a) $t_r/T = 1.0$ and 2.0, (b) $t_r/T = 0.2$ and 0.5.

Table 6.8 shows the ratio of exerted moment at the base of the sea-side pillar based on the three different distributions to the same moment according to moments obtained from using Iizuka and Matsutomi (2000) formula (distribution 1) and static analysis. Analysis results are shown for various values of t_r/T. The moments obtained from a static and a dynamic analysis, using Distribution 3, are up to 16% and 46% larger than the moment obtained using Iizuka and Matsutomi's (2000) formula for the case when $t_r/T = 0.2$, respectively. The increase in the static moment is due to the fact that a higher centroid, induces larger moments at the base of the structure. Distribution 2 does not affect the results significantly.

Table 6.8. Ratio of exerted moment at the base of the sea-side pillar based on different distributions to the same moment due to Iizuka *et al.* (2000) formula and static analysis (Distribution 1).

	$t_r/T = 0.2$	$t_r/T = 0.5$	$t_r/T = 1.0$	$t_r/T = 1.5$	$t_r/T = 2.0$
Distribution 1 (dynamic)	1.25	1.08	0.96	1.00	0.96
Distribution 2 (static)	1.06	1.06	1.06	1.06	1.06
Distribution 2 (dynamic)	1.26	1.10	1.00	1.03	1.00
Distribution 3 (static)	1.16	1.16	1.16	1.16	1.16
Distribution 3 (dyamic)	1.46	1.24	1.10	1.15	1.10

Table 6.9 shows the ratio of structural displacement based on different distributions to the displacement obtained using Iizuka and Matsutomi's (2000) formula (with distribution 1) and static analysis for various values of t_r/T. It is observed that the dynamic response, in terms of displacement has increased up to 55% for the case when t_r/T = 0.2. The displacements obtained based on Distribution 3 are 20% and 86% larger than the displacement obtained using Iizuka and Matsutomi (2000) formula in static and dynamic analysis for the case when t_r/T = 0.2, respectively. However, the displacement using Distribution 2 reduces the static displacement of the structure for the same value of t_r/T, which is due to a lower centroid of the forces.

Table 6.9. Ratio of the horizontal displacement of the structure based on different distributions to the same distribution according to Iizuka and Matsutomi (2000) formula (Distribution 1) and static analysis.

	$t_r/T = 0.2$	$t_r/T = 0.5$	$t_r/T = 1.0$	$t_r/T = 1.5$	$t_r/T = 2.0$
Distribution 1 (dynamic)	1.55	1.23	1.02	1.09	1.02
Distribution 2 (static)	0.87	0.87	0.87	0.87	0.87
Distribution 2 (dynamic)	1.36	1.07	0.89	0.95	0.89
Distribution 3 (static)	1.20	1.20	1.20	1.20	1.20
Distribution 3 (dyamic)	1.86	1.47	1.22	1.31	1.22

Chapter 7. Conclusions

Based on an extensive analysis of the data obtained from the experiments discussed in Chapter 5, as well as the structural analysis presented in Chapter 6, the following conclusions can be drawn:

- The time history of global horizontal force exerted on the circular structure in the main flow direction was presented in Section 5.3.1. It was observed that the initial impact force does not overshoot the hydrodynamic force for the case of the circular structure.
- The temporal variation and vertical distribution of pressures exerted on structures due to the impact of a hydraulic bore were presented in Section 5.3.4. Maximum pressure was exerted at approximately 40% of the bore height on the structure.
- Detailed characteristics of the measured force and pressure depend on the instrumentation used and the size of the measurement area. Small pressure transducers with very rapid response times are able to capture highly impulsive forcing events having very short rise times and relatively large maximum pressure. Such impulse pressure events may be confined to a relatively small area, or may occur non-simultaneously over a large area. Thus, force or pressure measurements performed over a larger area generally appear less impulsive. The fact that instruments, such as dynamometers, designed to measure force or pressure over a large area generally feature slower response times may also contribute to this result.
- Debris impact tests were performed in order to improve estimation of maximum impact force based on debris mass and velocity, as explained in Section 5.5. It was observed that velocity of log does not significantly affect stopping time.

- Comparison of existing codes and guidelines that address tsunami-induced forces was presented in Section 6.1 through calculation of these forces for a prototype moment-resisting frame structure with the short side perpendicular to the advancing bore. It was observed that non-breakaway walls or rigid exterior non-structural components lead to larger design base shears.
- Based on the design example presented in Section 6.1, it is concluded that the magnitude of tsunami-induced design forces depends significantly on the design inundation depth. Therefore, attention must be paid to the determination of design inundation depth in the preparation of reliable tsunami hazard maps.
- Based on the comparison made in Section 6.1, it was observed that the use of the CCH and SMBTR formulas leads to significantly larger base shear forces comparing to the results provided by FEMA 55. The reason for this discrepancy is the omission of a surge component in the FEMA 55 loads.
- The dynamic analysis of a simple structural model in Section 6.2 revealed the significance of dynamic amplification in terms of the structures base reactions and global displacements. For example, results showed that, for the case when $t_r/T = 0.2$, resulting moments at the sea-side pillar and the horizontal displacement increase up to 25% and 55% respectively, compared to static analysis.

7.1. Recommendations for Future Work

The survey of literature demonstrated that limited research has been performed studying the following topics. Future work can be geared towards improving existing understanding of these phenomena.

- Vertical distribution of exerted forces and pressures due to bores on walls and other various free-standing structures (pier bridges, columns, reservoirs, etc).
- Studying effect of parameters that affect exerted forces due to bores, such as obstacles upstream of the structure (location, disposal, etc.)

- Development of new guidelines for the estimation of the hydrodynamic impact forces on specific structures.
- Development and verification of coupled hydraulic-structural numerical models capable of real-time analysis of structural response to hydrodynamic forces.
- Investigation of the applicability of the surge force component in the calculation of the tsunami load.

References

[1] AASHTO (1998). "LRFD Bridge Design Specifications." Second edition. American Association of State Highways and Transportation Officials, 26–27.

[2] Arnason, H. (2005). "Interactions between and incident bore and a free-standing coastal structure." Ph.D. Thesis, University of Washington, Seattle, 172 pp.

[3] Asakura, R., Iwase, K., and Iketani, T. *et al.* (2000). "Experimental research about wave force by the tsunami which overflow the revetment." *Proc. of the Coastal Engineering of JSCE*, **47**, 911-915.

[4] ASCE Standard. (2005). "Minimum design loads for buildings and other structures." SEI/ASCE 7-05, 376 pp.

[5] Barr, D. I. H., and Das, M. M. (1980). "Numerical simulation of dam-burst and reflections, with verification against laboratory data." *Proc. Institution Civil Engineers*, **69**(2), 359-373.

[6] Bell, S.W., Elliot, R.C., and Chaudhry, M.H. (1992). "Experimental results of two dimensional dam-break flows." *J. of Hydraulic Research*, **30**(2), 225-252.

[7] Briechle, S., and Kötenger, J. (2002). "Experimental data for dike-break waves." *Proc., River Flow 2002*, D. Bousmar and Y. Zech, eds., Balkema, Rotterdam, Netherlands, **1**, 467–473.

[8] Bryant, E. (2001). "Tsunami: the underrated hazard." Cambridge University Press, London, UK.

[9] Camfield, F. (1980). "Tsunami Engineering." Coastal Engineering Research Center, US Army Corps of Engineers, Special Report (SR-6), 222 pp.

[10] Chanson, H. (2005a). "Applications of the Saint-Venant equations and method of characteristics to the dam-break wave problem." Report No. CH55/05, Dept. of Civil Engineering, The University of Queensland, Brisbane, Australia, May, 135 pp.

[11] Chanson, H. (2005b). "Analytical solution of dam-break wave with flow resistance: Application to tsunami surges." *Proc. 31st Biennial IAHR Congress*, Seoul, Korea, 0137, 3341-3353.

[12] Chanson, H. (2006). "Tsunami surges on dry coastal plains: Application of dam break wave equations." *Coastal Engineering Journal*, **48**(4), 355-370.

[13] Chervet, A., and Dalleves, P. (1970). "Calcul de l'onde de submersion consecutive a la rupture d'un barrage (Computation of wave due to a sudden release of a dam)." Schweizerische Bauzeitung, **88**(19), 420-432 (in French).

[14] CNN. (2007). http://www.cnn.com/interactive/world/0502/gallery.tsunami.photos/frameset.exclude.html, referred to on 2007-8-8.

[15] Cox, D. C., and Mink, J.F. (1963). "The tsunami of 23 May 1960 in the Hawaiian Islands." *Bull. Seism. Soc. Am.* 53, 1191-1209.

[16] Cross, R. H. (1967). "Tsunami Surge Forces." *Journal of the Waterways and Harbor Division*, ASCE, **93**(4), 201-231.

[17] Cumberbatch, E. (1960). "The impact of a water wedge on a wall" *J. of Fluid Mechanics*, **7**, 353-374.

[18] Dames and Moore. (1980). "Design and construction standards for residential construction in tsunami prone areas in Hawaii." (Prepared for the Federal Emergency Management Agency).

[19] Department of Planning and Permitting of Honolulu Hawaii. (2000). "City and County of Honolulu Building Code." Chapter 16, Article 11.

[20] Dias, P., Fernando, L., Wathurapatha, S., and De Silva, Y. (2005). "Structural resistance against sliding, overturning and scouring caused by tsunamis." *International Conference of Disaster Reduction on Coasts*, Melbourne.

[21] Dressler, R. (1954). "Comparison of theories and experiments for the hydraulic dam-break wave." *Proc. Intl Assoc. of Scientific Hydrology Assemblée Générale*, Rome, Italy, **3**(38), 319-328.

[22] Drobir, H. (1971). "Der Ausfluss aus einem Speicher beim Bruch einer Talsperre (The discharge from a reservoir caused by dam breaching)." Mitteilung 17, Institute fur Wasserwirtschaft und konstruktiven Wasserbau, Technische Hochschule: Graz (in German).

[23] Estrade, J. (1967). "Contribution à l'Etude de la Suppression d'un Barrage. Phase Initiale de l'Ecoulement. (Contribution to the Study of Dam Break. Initial Stages of the Wave)." Bulletin de la Direction des Etudes et Recherches, Series A, Nucléaire, Hydraulique et Thermique, EDF Chatou, France, **1**, 3-128.

[24] FEMA. (1995). "Engineering principles and practices for retrofitting flood-prone residential buildings." FEMA Report No. 259, Federal Emergency Management Agency.

[25] FEMA. (2003). "Coastal Construction Manual." (3 vols.), 3rd Ed. (FEMA 55), Federal Emergency Management Agency, Jessup, MD.

[26] Fraccarollo, L., and Capart, H. (2002). "Riemann wave description of erosional dam-break flows." *J. Fluid Mech.*, **461**, 183–228.

[27] Franco, A. B. (1996). "Modelação computacional e experimental de escoamentos provocados pela rotura de barragens." PhD thesis, Instituto Superior Técnico, Lisbon, Portugal (in Portuguese).

[28] Fukui, Y., Nakamura, M., Shiraishi, H., and Sasaki, Y. (1963). "Hydraulic study on tsunami." *Coastal Engineering in Japan*, Tokyo, **6**, 67-82.

[29] Ghobarah, A., Saatcioglu, M., and Nistor, I. (2006). "The impact of 26 December 2004 earthquake and tsunami on structures and infrastructure." *J. Engineering Structures*, Elsevier, **28**, 312-326.

[30] Gomez-Gesteira, M., and Dalrymple, R.A. (2004). "Using a 3D SPH Method for Wave Impact on a Tall Structure." *J. Waterways, Port, Coastal, Ocean Engineering*, **130**(2), 63-69.

[31] Grundy, P., Thurairajah, A., and Walker, G. (2005). "Some reflections on the structural engineering aspects of tsunami damage." *Proc. Australian Earthquake Engineering Society*, Albury, New South Wales.

[32] Haehnel, R.B., and Daly, S.F. (2002). "Maximum impact force of woody debris on floodplain structures." Technical Report: ERDC/CRREL TR-02-2, US Army Corps of Engineers, 40 pp.

[33] Haehnel, R. B., and Daly, S. F. (2004). "Maximum impact force of woody debris on floodplain structures." *J. Hydraul. Eng.*, **130**(2), 112–120.

[34] Haritos, N., Ngo, T., and Mendis, P. (2005). "Modelling tsunami wave force effects on structures." *Proc. Australian Earthquake Engineering Society*, Albury, New South Wales.

[35] Hibberd, S., and Peregrine, D. H. (1979). "Surf and run-up on a beach: A uniform bore." *J. Fluid Mech.*, **95**, 323 -345.

[36] Iizuka, H., and Matsutomi, H. (2000). "Damage due to the flooding flow of tsunami." *Proc. Conf. Coastal Engineering.*, JSCE, **47**, 381-385 (in Japanese).

[37] Ikeno, M., Mori, N., and Tanaka, H. (2001). "Experimental research about wave force of a bore and a breaking wave, and the action and impulsive force of drifting timber." *Proc. of the Coastal Engineering of JSCE*, **48**, 846-850.

[38] International Code Council, INC. (2006). "2006 International Building Code." Country Club Hills, IL.

[39] Kirkgoz, M.S. (1990). "An experimental investigation of a vertical wall response to breaking wave impact." *Ocean Engineering*, **17**, 379–391.

[40] Kirkoz, M.S. (1983). "Breaking and run-up of long waves, tsunamis: their science and engineering." *10th IUGG International Tsunami Symposium*, Sendai-shi/Miyagi-ken, Japan, Terra Scientific Publishing, Tokyo, Japan.

[41] Kleefsman, K.M.T., Fekken, G., Veldman, A.E.P., Iwanowski, B., and Buchner, B. (2005). "A volume-of-fluid based simulation methods for wave impact problems." *J. Comput. Phys.*, **206**, 363-393.

[42] Lauber, G., and Hager, W.H. (1998). "Experiments to dam-break wave: horizontal channel." *J. of Hydraulic Research, IAHR*, **36**(4), 291-307.

[43] Leal, J. G. A. B. (1999). "Modelação matemática da propagação de ondas de cheia provocadas pela ruptura de barragens em canais de leito móvel." MS thesis, Instituto Superior Técnico, Lisbon, Portugal (in Portugues).

[44] Leal, J. G. A. B., Ferreira, R. M. L., and Cardoso, A. H. (2002). "Dam-break waves on movable bed." *Proc. River Flow 2002*, D. Bousmar and Y. Zech, eds., Balkema, Rotterdam, the Netherlands, **2**, 981–990.

[45] Leal, J. G. A. B., Ferreira, R. M. L., and Cardoso, A. H. (2006). "Dam-break wave-front celerity." *J. of Hydraulic Engineering*, **132**, 69-76.

[46] Levin, L. (1952). "Mouvement non permanent sur les cours d'eau la suite de rupture de barrage (Unsteady river flow caused by a dam-break)." *Revue Generale de l'Hydraulique*, **18**, 297-315 (in French).

[47] Maheshwari, B. K., Sharma, M. L., and Narayan, J. P. (2006). "Geotechnical and Structural Damage in Tamil Nadu, India, from the December 2004 Indian Ocean Tsunami." *Earthquake Spectra*, Earthquake Engineering Research Institute, **22**, 475-493.

[48] Martin, H. (1981). "Dammbruchkurven in horizontalen Rechteckkanalen (Dam-break curves in horizontal rectangular channels)." Acta Hydrophysica Berlin **26**(1), 45-65 (in German).

[49] Matskevitch, D.G. (1997). "Eccentric impact of an ice feature: Linearized model." Cold Regions Science and Technology, **25**, 159–171.

[50] Matsutomi, H. (1999). "A practical formula for estimating impulsive force due to driftwoods and variation features of the impulsive force." *J. Hyd., Coastal and Environmental Engineering, JSCE*, Japan, **621**/II-47, 111-127 (in Japanese).

[51] Matsutomi, H., Sakakiyama, T., Sindhu, N., and Matsuyama, M. (2006). "Aspects of inundated flow due to the 2004 Indian Ocean tsunami." *Coastal Engineering Journal, JSCE*, 48(2), 167-195.

[52] Miles, M.D. (2001). "GEDAP User's Guide for Windows NT." National Research Council of Canada, Technical Report HYD-TR-021, Ottawa, Canada, 96 pp.

[53] Miller, S., and Chaudhry, M.H. (1989). "Dam-break flows in curved channel." *J. of Hydraulic Engineering*, ASCE, **115**(11), 1465-1478.

[54] Mizutani, S., and Imamura, F. (2001). "Dynamic wave force of tsunamis acting on a structure." *Proc. Int. Tsunami Symp.*, Washington, **7**(28), 941-948.

[55] Munich Re Group. (2005). "Annual Review: Natural Catastrophes 2004 in the Munich Re Group Knowledge Series." *Topics Geo*, 60 pp.

[56] Murty, C. V. R., Rai, D. C., Jain, S. K., Kaushik, H. B., Mondal, G., and Dash, S. R. (2006). "Performance of Structures in the Andaman and Nicobar Islands (India) during the December 2004 Great Sumatra Earthquake and Indian Ocean Tsunami." *Earthquake Spectra*, Earthquake Engineering Research Institute, **22**, 321-354.

[57] Murty, T.S. (1977). "Seismic sea waves: tsunamis." Bulletin of the Fisheries Research Board of Canada- no. 198, Department of Fisheries and the Environment, Fisheries and Marine Service, Scientific Information and Publishing Branch, Ottawa, Canada.

[58] NAASRA (1990). "Highway Bridge Design Specification." National Association of Australian State Road Authorities.

[59] Nakano, Y., and Paku, C. (2005). "Studies on lateral resistance of structures and tsunami load caused by the 2004 Sumatra Earthquake, part 2: Comparison of tsunami load and lateral resistance." Summaries of technical papers of Annual meeting Architectural Institute of Japan (Kinki).

[60] Nistor, I., Saatcioglu M., and Ghobarah, A. (2006). "Tsunami Hydrodynamic Impact Forces on Physical Infrastructures in Thailand and Indonesia." *Proc. Annual Conf. of the Canadian Society for Civil Eng.*, CSCE, Calgary, Canada.

[61] Nortek (2004). "Nortek User Guide." Rev. C. Nortek AS, Norway.

[62] Nouri Y., Nistor I., Palermo D., and Saatcioglu, M. (2007a). "Tsunami-induced hydrodynamic and debris flow forces on structural elements." *9th Canadian Conference of Earthquake Engineering*, Ottawa, Canada, June.

[63] Nouri, Y., Nistor, I., Palermo, D., and Cornett, A. (2007b). "Structural Analysis for Tsunami-Induced Force and Debris Impact." *Coastal Structures 2007*, Venice, Italy.

[64] Ohmori, M., Fujii, N., and Kyotani, O. *et al.* (2000). "The numerical computation of the water level, the flow velocity and the wave force of the tsunami which overflow the perpendicular revetments." *Proc. of the Coastal Engineering of JSCE*, **47**, 3766-380.

[65] Okada, T., Sugano, T., Ishikawa, T., Ohgi, T., Takai, S., and Hamabe, C. (2005). "Structural design methods of buildings for tsunami resistance." (SMBTR), the Building Centre of Japan.

[66] Okada, T., Sugano, T., Ishikawa, T., Takai, S., and Tateno, T. (2006). "Tsunami loads and structural design of tsunami refuge buildings." the Building Centre of Japan.

[67] Pacheco, K. H., and Robertson, I. N. (2005). "Evaluation of tsunami loads and their effect on reinforced concrete buildings." University of Hawaii Research Report.

[68] Packwood, A. R., and Peregrine, D. H. (1981). "Surf and run-up on beaches: models of viscous effects." Rep. AM-81-07, Univ. of Bristol, UK.

[69] Palermo, D., Nistor, I., Cornett, A., and Nouri, Y. (2007). "Tsunami-Induced Impact and Hydrodynamic Loading of Near-Shoreline Structures." PROTECT 2007 (First International Workshop on Performance, Protection & Strengthening of Structures Under Extreme Loading), Whistler, Canada.

[70] Pbase (2007). http://www.pbase.com/issels/image/37890946, referred to on 2007-8-8.

[71] Ramsden, J.D. (1993). "Tsunamis: Forces on a vertical wall caused by long waves, bores, and surges on a dry bed." Report No. KH-R-54, W.M. Keck Laboratory, California Institute of Technology, Pasadena, Calif., 251 pp.

[72] Ramsden, J.D. (1996). "Forces on a vertical wall due to long waves, bores, and dry-bed surges." *J. Waterways, Port Coasts and Ocean Eng.*, **122**(3), 134-141.

[73] Ramsden, J.D., and Raichlen, F. (1990). "Forces on vertical wall caused by incident bores." *J. of Waterway, Port, Coastal, and Ocean Engineering*, **116**, 592-613.

[74] Ritter, A. (1892). "Die Fortpflanzung der Wasserwellen." *Vereine Deutscher Ingenieure Zeitswchrift*, **36**(2), 947-954 (in German).

[75] Ruangrassamee, A., Yanagisawa, H., Foytong P., Lukkunaprasit, P., Koshimura, S., and Imamura, F. (2006). "Investigation of Tsunami-Induced Damage and Fragility of Buildings in Thailand after the December 2004 Indian Ocean Tsunami." *Earthquake Spectra*, Earthquake Engineering Research Institute, **22**, 377-401.

[76] Saatcioglu, M., Ghobarah, A., and Nistor, I. (2005). "Reconnaissance report on the December 26, 2004 Sumatra earthquake and tsunami." final report prepared for the Canadian Association of Earthquake Engineering, Ottawa, Canada, 27 pp.

[77] Saatcioglu, M., Ghobarah, A., and Nistor, I. (2006a). "Performance of structures in Thailand during the 2004 Sumatra earthquake and tsunami." *Earthquake Spectra*, **22**, 355-375.

[78] Saatcioglu, M., Ghobarah, A., and Nistor, I. (2006b). "Performance of structures in Indonesia during the 2004 Sumatra earthquake and tsunami." *Earthquake Spectra*, **22**, 295-319.

[79] Schmidt, R., Oumeraci, H., and Partenscky, H.W. (1992). "Impact loads induced by plunging breakers on vertical structures." *Proc. 23rd Intl. Conf: Coastal Engineering,* ASCE, Venice, 1545-1558.

[80] Shuto, N. (1994). "Building damage evaluation for the 1993 Okushiri tsunamis, Tsunami Engineering." Technical Report No.11, DCRC, Tohoku University, (in Japanese).

[81] Snodgrass, F.E., Rice, E.K., and Hall, M. (1951) "Wave forces on piling." (Monterey Field Test), Univ. California, Berkeley, CA, Inst. Of Engineering Research, Tech. Rept. Series 35, Issue 4, June, 9 pp.

[82] Stansby, P.K., Chegini, A., and Barnes, T.C.D. (1998). "Initial stages of dam-break flow." *J. Fluid Mech.*, **370**, 203–220.

[83] Stoker, J. J. (1957). "Water waves: The mathematical theory with applications." Wiley-Interscience, New York.

[84] Synolakis, C. E. (1991). "Tsunami run-up on steep slopes: How good linear theory really is." *Natural Hazards*, **4**, 221-234.

[85] Thurairajah, A. (2005). "Structural design loads for tsunami and floods." *International Symposium Disaster Reduction on Coasts*, Monash University, Melbourne, Australia.

[86] Tomita, T., Imamura, F., Arikawa, T., Yasuda, T., and Kawata, Y. (2006). "Damage caused by the 2004 Indian Ocean Tsunami on the southwestern coast of Sri Lanka." *Coastal Engineering Journal*, **48**(2), 99-116.

[87] Tsuji, Y. (2005). "Distribution of the tsunami heights of the 2004 Sumatra tsunami in Banda Aceh measured by the tsunami survey team." Internet Resource, referred to on 2007-8-8 {http://www.eri.u-tokyo.ac.jp/namegaya/sumatera/surveylog/eindex.htm}.

[88] UBC (1997). "1997 Uniform Building Code." *International Conference of Building Officials*, California.

[89] US Army Corps of Engineers. (1960). "Floods resulting from suddenly breached dams." Miscellaneous Paper 2(374), Report 1. US Army Engineer Waterways Experiment Station, Corps of Engineers: Vicksburg, Mississippi.

[90] U.S. Army Corps of Engineers. (1961). "Floods resulting from suddenly breached dams-Conditions of high resistance." Miscellaneous Paper 2(374), Report 2. US Army Engineer Waterways Experiment Station, Corps of Engineers: Vicksburg, Mississippi.

[91] USGS. (2007). Earthquake Hazards Program, referred to on 2007-8-8, http://earthquake.usgs.gov/regional/world/most_destructive.php

[92] Whitham, G. B. (1955). "The effects of hydraulic resistance in the dam-break problem." *Proc. Roy. Soc. London*, Ser. **A227**, 399-407.

[93] Yamamoto, Y., Takanashi, H, Hettiarachchi, S., and Samarawickrama, S. (2006). "Verification of the destruction mechanism of structures in Sri Lanka and Thailand due to the Indian Ocean tsunami." *Coastal Engineering Journal*, **48**(2), 117-146.

[94] Yeh, H. (1991). "Tsunami bore runup." *Natural Hazards*, **4**, 209-220.

[95] Yeh, H. (2006). "Tsunami loading." International workshop on fundamentals of coastal effects of tsunamis, Hilo, Hawaii. tsunami.orst.edu/workshop/2006/doc/Yeh_TsunamiLoading.pdf

[96] Yeh, H., and Mok, K. M. (1990). "On turbulence in bores." *Phys. Fluids*, **A2**, 821-828.

[97] Yeh, H., Ghazali, A., and Marton, I. (1989). "Experimental study of bore runup." *J. of Fluid Mechanics*, **206**, 563-578.

[98] Yeh, H., Robertson, I., and Preuss, J. (2005). "Development of design guidelines for structures that serve as tsunami vertical evacuation sites." Report No 2005-4, Washington Dept. of Natural Resources.